CUMENTATION PAGE

Form Approved
OMB No. 0704-0188

ation is estimated to average 1 hour per response, including the time for reviewing instructions, searching existing data sources,
mplet ng and reviewing the collection of information. Send comments regarding this burden estimate or any other aspect of this
educing this burden to Washington Headquarters Services, Directorate for Information Operations and Reports, 1215 Jefferson
2 and to the Office of Management and Budget, Paperwork Reduction Project (0704-0188) Washington, DC 20503

2. REPORT DATE	3. REPORT TYPE AND DATES COVERED
May 1993	THESIS/DISSERTATION

4. TITLE AND SUBTITLE	5. FUNDING NUMBERS
Design of A Fluid Elastic Actuator With Application to Structural Control	

6. AUTHOR(S)

Lt Mark K Ciero

7. PERFORMING ORGANIZATION NAME(S) AND ADDRESS(ES)	8. PERFORMING ORGANIZATION REPORT NUMBER
AFIT Student Attending: Massachusetts Institute of Technology	AFIT/CI/CIA-

9. SPONSORING/MONITORING AGENCY NAME(S) AND ADDRESS(ES)	10. SPONSORING/MONITORING AGENCY REPORT NUMBER
DEPARTMENT OF THE AIR FORCE AFIT/CI 2950 P STREET WRIGHT-PATTERSON AFB OH 45433-7765	

DTIC
ELECTE
AUG 1 1 1993
S
C D

11. SUPPLEMENTARY NOTES

12a. DISTRIBUTION/AVAILABILITY STATEMENT	12b. DISTRIBUTION CODE
Approved for Public Release IAW 19 Distribution Unlimited MICHAEL M. BRICKER, SMSgt, USAF Chief Administration	

13. ABSTRACT *(Maximum 200 words)*

93 8 05 131

14. SUBJECT TERMS			15. NUMBER OF PAGES
			152
			16. PRICE CODE

17. SECURITY CLASSIFICATION OF REPORT	18. SECURITY CLASSIFICATION OF THIS PAGE	19. SECURITY CLASSIFICATION OF ABSTRACT	20. LIMITATION OF ABSTRACT

DESIGN OF A FLUID ELASTIC ACTUATOR WITH APPLICATION TO STRUCTURAL CONTROL

Mark K. Ciero

Lt. U.S.A.F.

B.S., Aeronautical Engineering

B.S., Engineering Mechanics

United States Air Force Academy, 1991

Submitted to the Department of Aeronautics and Astronautics in Partial
Fulfillment of the Requirements for the Degree of

MASTER OF SCIENCE in AERONAUTICS AND ASTRONAUTICS

at the

MASSACHUSETTS INSTITUTE OF TECHNOLOGY

May 1993

Signature of Author _____
Department of Aeronautics and Astronautics
May 28, 1993

DESIGN OF A FLUID ELASTIC ACTUATOR WITH APPLICATION TO STRUCTURAL CONTROL

by

MARK K. CIERO, Lt. U.S.A.F.

ABSTRACT

An elastically deformable pressure vessel is used as an actuator. The internal pressure is controlled hydraulically via force applied to an external bellows. The resulting elongation of the vessel is a linear function of the input force, and depends on the physical properties of the vessel, fluid, and bellows. The design includes an orifice through which fluid flows, adding damping to the actuator.

Mathematical models of the actuator are developed which relate performance of the actuator to its geometry and material properties. A static analysis yields the linear relationship between the commanded input force and the resulting elongation of the vessel. A model of the passive (no input force) response of the actuator indicates it will act as a passive damper. The active response (application of a dynamic input force yielding a dynamic elongation) is limited in frequency by the orifice damping. Strategies for optimizing the actuator size and material properties are developed from the models.

Actuators manufactured with differing materials and fluids were tested. The static results are linear and matched the analysis. The passive results and the model predictions confirm that the configuration of the actuators, as built, is poor for passive damping. The correlation between the model and active experiments is excellent. Actuation bandwidth is shown to be selectable by selecting orifice size. Tailoring the material properties of the vessel by the use of optimally designed composite laminates results in a factor of two improvement in the performance.

The actuator is useful for structural control. It's performance is comparable to other available actuators, it is constructed of off-the-shelf hardware, and it has the advantages of a built-in frequency limit and easily customizable performance characteristics.

Acknowledgement

In the short two years that I have been here (which recently have seemed like two decades), I have had the privelege of meeting and working with so many brillant good-natured people.

The top of the list begins with my advisor, Professor Hugh McManus. Without his guidance, his time, and a couple of cups of coffee (that he bought), this thesis would not be possible. His insight and ability to solve problems were a charachteristic that I admired (and hoped a little has rubbed off on me). I am very grateful. Thank you.

To everyone at the Space Engineering Center whom I have gotten to know and joked with thanks for keeping me sane. The help of so many of you was much appreciated. I certanly will miss the lab. (I think, thanks to the Air Force, I will reach orbital velocity the first time out.)

To Professor Jack Kerrebrock, thank you for the concept and for recruiting me. I hope this thesis represents just the first tidbit of what is possible with your idea.

To my wife, who married me knowing the thesis was on the horizon but, probably, did not anticipate the role of late-night editor, thank you. If it had not been for you my organization may have drowned me. I consider myself extremely fortunate to have found a person as understanding and willing to help as you. You have demonstrated so clearly that our friendship and companionship, no matter what the future entails, is a constant that we can trust in. Thank you.

Table of Contents

List of Figures

8

List of Tables

Nomenclature

$\mathbf{A}, \mathbf{X}, \mathbf{Bd}$	State Space System Matrices
$\mathbf{A}$	Composite Thickness Weighted Stiffness Matrix
A_{act}	Admittance of P-Strut in Active Model
A_{DCact}	Admittance at DC Frequency
A_{zc}	Area of Cylinder Wall (i.e. Annulus Area)
A_c	Cross-Sectional Area of Cylinder
A_b	Effective Cross-Sectional Area of Bellows
A_o	Cross-Sectional Area of Orifice
B_f	Bulk Modulus of the Fluid
B_w	Bandwidth (Frequency)
c	Damping Coefficient Multiplied by Area Ratic
$\mathbf{C}_y, \mathbf{C}_z, \mathbf{K}_{AS}, \mathbf{N}, \mathbf{Y}, \mathbf{e}, \mathbf{r}$	Control State Space Matrices
	Damping Coefficient
C	Damping of Structure or Orifice Modeled
	Damping Coefficient
C_1	Damping Coefficient Used in Passive Model
C_{lam}	Laminar Flow Damping or Dashpot Coefficient
C_{turb}	Turbulent Flow Damping or Dashpot Coefficient
$\mathbf{C}^L$	Laminate Compliance Matrix
D_o	Diameter of Orifice
$\mathbf{E}$	Material Property Matrix
E, ν, G	Isotropic Material Properties (Young's Modulus, Poisson's Ratio, Shear Modulus)
$E_{11}^L, E_{22}^L, \nu_{12}^L, \nu_{21}^L, G_{12}^L$	Laminate Effective Direction Material Properties
F_b	Input Force into Bellows
F_d	Disturbance Force from Structure into Actuator
F_L	Force from Actuator into Structure
h_{lam}, h_{turb}	Laminar and Turbulent Head Loss Coefficients
h_{end}	Head Loss Coefficient Due to Roughness or Blunt Orifice Ends
K	Structural Stiffness

K_1, K_2	Stiffnesses Associated with the Passive Damping Model
K_b	Static Stiffness of Bellows
k_b	Static Stiffness of Bellows Multiplied by Area Ratio
K_f	Volumetric Stiffness of Fluid
K_L	Longitudinal Stiffness
K_{pass}	Complex Stiffness of P-Strut in Passive Model
K_{pass}'	Revised Complex Stiffness of Passive Model
K_R	Hoop or Radial Dilation Stiffness
K_S	Structural Stiffness of Bellows
K_{DCp}	Passive Stiffness at DC Frequency
K_{DCep}, K_{ep}, C_{ep}	Epoxy Stiffness and Dashpot Parameters
$K_{\infty p}$	Passive Stiffness at Infinite Frequency
L, L_{eff}	Physical and Effective Length of Cylinder
L_{dev}	Entrance or Development Length in Orifice
L_o	Length of Orifice
M	Mass of Structure
P	Internal Cylinder Pressure
P_b	Internal Bellows Pressure
R_i, R_c, R_o	Interior Radius of Cylinder, Mean Radius of Cylinder, and Outer Radius of Cylinder
Re	Reynold's Number
s	Complex or Bode Frequency ($i\omega$)
t	Thickness of Cylinder Wall
t_{al}, t_{comp}	Thickness of Aluminum and Composite Cylinders
t_{dev}	Time Required to Develop Laminar Flow in Orifice
t_{dev}^{*}	Non-Dimensional t_{dev}
t_r	Time to Rise (Step Input)
V_o	Velocity of Fluid in the Orifice
Z	State Space Performance Variable
β	Ratio or Frequency of Pole Divided By Zero.
δ_b	Input Bellows Stroke
δ_L	Elongation or Actuation Authority
δ_R	Radial Dilation (Expansion)

$\varepsilon_{11}, \varepsilon_{22}$	Longitudinal and Hoop Strain
ε	Strain Vector
ϕ	Bode Phase
η, η^*	Loss Factor and Peak Loss Factor
φ	Fiber Orientation Angle for Composites
μ	Fluid Absolute Viscosity
ρ	Fluid Density
σ_{11}, σ_{22}	Longitudinal and Hoop Stress
σ	Stress Vector
υ	Fluid Kinematic Viscosity
ϖ	End Effect
ω	Frequency
ω^*_{dev}	Non-Dimensional Oscillating Fluid Frequency For Quasi-Laminar Fluid Flow
ω^*	Peak Damping Frequency
ω_n	Natural Frequency
ω_c	Corner Frequency
ω_z, ω_p	Zero and Pole Frequencies
ζ	System Damping Coefficient
ΔP	Pressure Loss Through Orifice Shearing
ΔV_f	Volume Change Due to Fluid Compression
ΔV_L	Volume Change Due to Longitudinal Expansion
ΔV_R	Volume Change in Radial Direction (Dilation)
ΔV_{total}	Total Volume Change
Γ	Strain Ratio: Hoop Strain to Longitudinal Strain
Γ_i, Γ_c	Isotropic and Composite Strain Ratios
Ψ_b	Area of Ratio: Cylinder Area to Bellows Area
Ψ_o	Area of Ratio: Cylinder Area to Orifice Area
Ψ_{ob}	Area of Ratio: Bellows Area to Orifice Area

CHAPTER 1:

A Fluid Elastic Actuator

1.1 INTRODUCTION

The established trend in structural design is towards light weight high performance structures. Often stringent performance criterion conflict with the flexibility inherent in light weight structures. Flexible space structures under current development, such as large deployable reflectors, optical interferometers, and orbital observation platforms, exhibit degraded performance in the presence of disturbance vibrations. On Earth, the engineering fields of robotics, high performance vehicles, and precision instruments include flexible structures which require dynamic stability and accurate positioning while subjected to disturbance vibrations.

An adaptive structure employs sensors to measure performance and actuators to correct deviations. Thus, an adaptive structure is capable of recognizing and manipulating its characteristics or states [52]. In order to alter the states, the structure must possess actuators capable of

14

commanding inputs, usually displacement or force, which can produce the desired and corrective action.

Passive devices intrinsically and independently react to their local state. A damper, for example, dissipates energy whenever it under goes a displacement. Passive devices act regardless of the cause of the local state, and without knowledge of the global, structural conditions. The performance of a passive component is not sensitive to desired changes in the structure and cannot be optimized or controlled once installed.

On the other hand, sensors and actuators managed by an automated control system can accomplish dramatic improvements in performance. Errors measured by sensors and feedback to the control system may be canceled by actuators. In addition, the physical attributes of the structure can be altered (i.e. a part could be stiffened or deployed/retracted) via an actuator under the direction of a control system [34].

Typically, an adaptive structure would compliment an actuator/sensor control system with passive devices in order to achieve the overall performance objective. The passive component reduces the disturbance and the level of control effort (i.e. amount of actuated displacement or force) needed and therefore required of an actuator.

A new concept of commanding displacements or force, by controlling the deformation of a fluid containing vessel, results in an actuator with advantageous characteristics. This idea combines an active component with passive fluid damping.

1.2   ACTUATOR CONCEPT

A closed vessel containing a pressurized fluid will deform. If the vessel is elastic and the fluid pressure is controlled, the deformation is elastic and predictable. If the vessel is constrained not to deform, the pressure response is a force. This elastic deformation or force can be used as an actuator to command displacement or force into a structure. The physical and mathematical principles which explain the elastic deformation of a pressurized vessel are well known. Utilizing a fluid as the pressurized medium causes the dynamic actuation to be a function of the viscous fluid motion, as well as the vessel properties. This viscous fluid motion produces innate passive damping.

Figure 1.1 depicts the geometry of a pressurized vessel. The internal pressure causes an elastic deformation, δ_L, or actuation force, F_L, which depend on the properties and dimensions of the vessel. An input force, F_b, controls the pressure via a piston-like mechanism. The fluid subjected to F_b is connected to the fluid in the vessel through a restricted passageway or orifice.

The actuation displacement, δ_L, is a linear function of F_b. If constrained, an actuation force, F_L, is a linear function of F_b multiplied by a ratio of the areas and dependent on the vessel properties. This amplification effect is analogous to a hydraulic jack or a mechanical lever where a large pressure force is gained at the expense of a large input displacement. As the viscous fluid squeezes through the orifice, the fluid undergoes a shearing action and releases energy. This loss of energy is the source of damping.
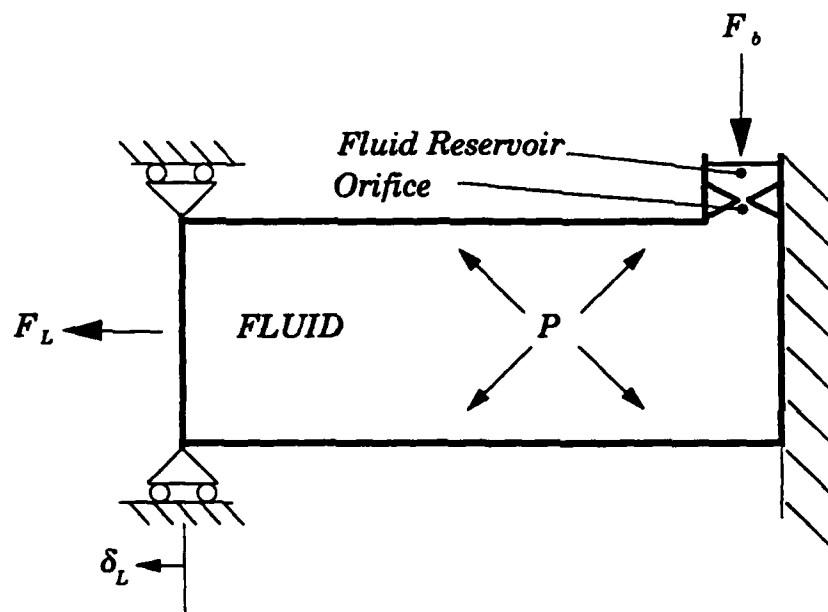
FIGURE 1.1: P-Strut Concept: An Elastic, Axially Deformable
Body Under Internal Fluid Pressure
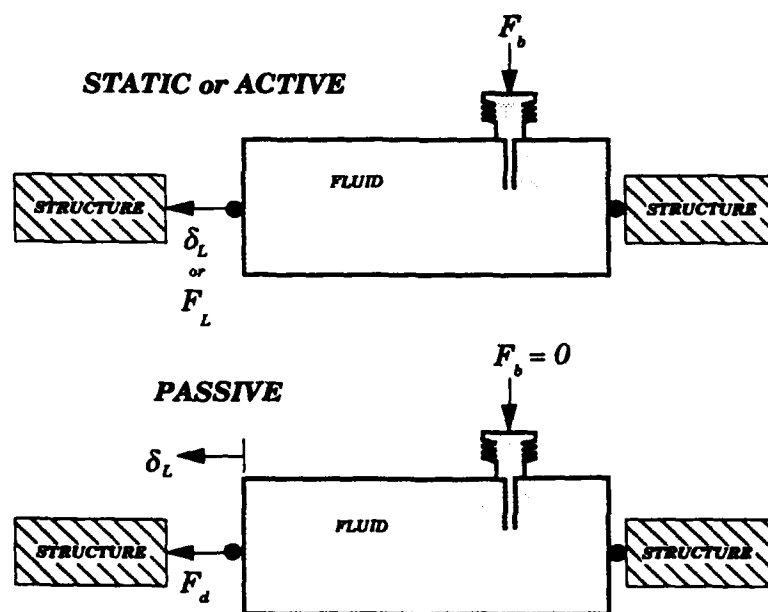
FIGURE 1.2: Static, Active, and Passive Modes
Of Operation

17

By tailoring the material properties of the vessel, the deformation or the actuation force can be optimized. Furthermore, the type of actuation—elongation, bending, or torsion—are functions of the geometry and material properties of the actuator.

1.3   STATIC, PASSIVE, AND ACTIVE MODES OF OPERATIONS.

The pressure actuator operates in three distinct modes which are illustrated in Figure 1.2. During static operation, where the velocity of the viscous fluid is negligible, the elongation, δ_L, is linear with the input force, F_b. Thus, the actuator could command and hold precise structural inputs by maintaining a constant fluid pressure.

In the presence of dynamic structural disturbances, F_d, the actuator would be expanded or compressed generating δ_L independent of F_b. In order to accommodate the volume changes resulting from the disturbance, the fluid in the vessel would be pumped or sucked through the orifice. The fluid shearing in the orifice would cause a damping of the disturbance. This mode of operation is passive.

The third mode of operation is active. If the input force, F_b, is dynamic, the fluid in the reservoir would be forced into the orifice at a rate directly dependent on F_b. However, the viscous fluid is inhibited by the restricted passageway. Therefore, F_b applied slowly would allow the fluid to pass through the orifice and into the vessel (i.e. near static conditions); but with a rapidly applied F_b the fluid would not squeeze through. Thus, the actuator cannot command displacement or force at high rates or frequencies. This physical limitation prevents the actuator from exciting

the higher dynamics of a structure or amplifying back into a structure control system noise.

The technology needed to create and implement the pressurized fluid elastic actuator is available from "off-the-shelf" hardware. The concept is straightforward and an inexpensive, simple alternative to other actuator approaches.

1.4   APPROACH

The proposed pressurized fluid elastic actuator (dubbed the P-Strut) was designed with the objective of achieving actuation comparable to other available actuators. The dimensions of the P-Strut were optimized by solving the pressure-displacement relationships for pressure vessels. The investigation examined the advantages of tailoring the material properties to maximize the axial elongation. Analytical models were developed to represent the three modes of operation.

Three P-Struts were manufactured to prove the concept and demonstrate the benefits of customizing the material properties. The actuators were tested in each of the three modes operation for a variety of fluids and orifice diameters. The results correlated well with the models.

1.5   THESIS OUTLINE

This thesis describes the development and verification of a fluid elastic actuator.

Chapter 2 provides the background to controlled structures and discusses pneumatic piston devices which have been previously applied to the control of flexible structures.

The analytical groundwork for the design is presented in Chapter 3. The investigation begins by developing the pressure-displacement relationships. The static performance equations, defined as input force, F_b, and input stroke, δ_b, versus actuator displacement, δ_L, are derived in terms of the P-Strut's material properties and physical dimensions. The viscous fluid and the orifice interaction is considered from solutions to channel flow problems. The three modes of operation are described via models which mimic the physics of the P-Strut. The parameters of these models include elastic material and volumetric fluid stiffnesses, as well as a rate dependent parameter (i.e. a dashpot) for the fluid-orifice effect. The models are used to define the appropriate mathematical equations. A parameteric study of the models emphasize the important parameters. The passive model was updated to account for an additional damping source discovered during testing.

The equations developed in Chapter 3 are combined to determine the optimal actuator dimensions in Chapter 4. An isotropic, a composite-aluminum hybrid, and an all-composite P-Strut are described and optimally designed to demonstrate the advantages of tailoring the actuator's material properties. The "off-the-shelf" components of the P-Strut are discussed as well as the properties of the viscous fluids utilized.

Chapter 5 details the manufacturing procedures and the test methods. The construction included the chemical milling of aluminum tubes, and the layup of aluminum-composite (hybrid) and all-composite tubes. The method of filling the actuator with fluid is presented. The test

objectives and setup are described. The techniques and equipment utilized
to determine the static, passive, and active performance of the P-Strut are
discussed.

The experimental results are reported and correlated in Chapter 6.
The performance of the three P-Struts with a variety of orifice and fluid
combinations is presented. The static performance was linear. The active
results compared favorably with the static results and the model developed
in Chapter 3. The advantage of tailoring the material properties is
supported by the data. Passive damping, probably caused by the epoxy used
in manufacturing, was discovered during testing. This damping
overshadowed the orifice damping.

A summary of the scientific and engineering benefits of this study
conclude the thesis in Chapter 7.

CHAPTER 2:

Structures and Actuators in Structures

2.1   CHAPTER OUTLINE

This chapter presents a short review of flexible structures and the relevant aspects of structural control. A one degree-of-freedom (1-DOF) model is used to explain issues involved in passive damping and active control. The use of an actuator in a feedback control system is examined. Three general categories of feedback control are considered.

Previous actuators which have used pressure as an actuation source are discussed and compared with the P-Strut concept. The differences between a piston pneumatic actuator and the fluid elastic actuator are clarified. Structural control issues surrounding the proposed fluid elastic actuator are presented.

2.2   THE CONTROLLED STRUCTURES FIELD

Figure 2.1 depicts an overview of the controlled structures field. Generally, a structure is first modeled with a set of assumptions and
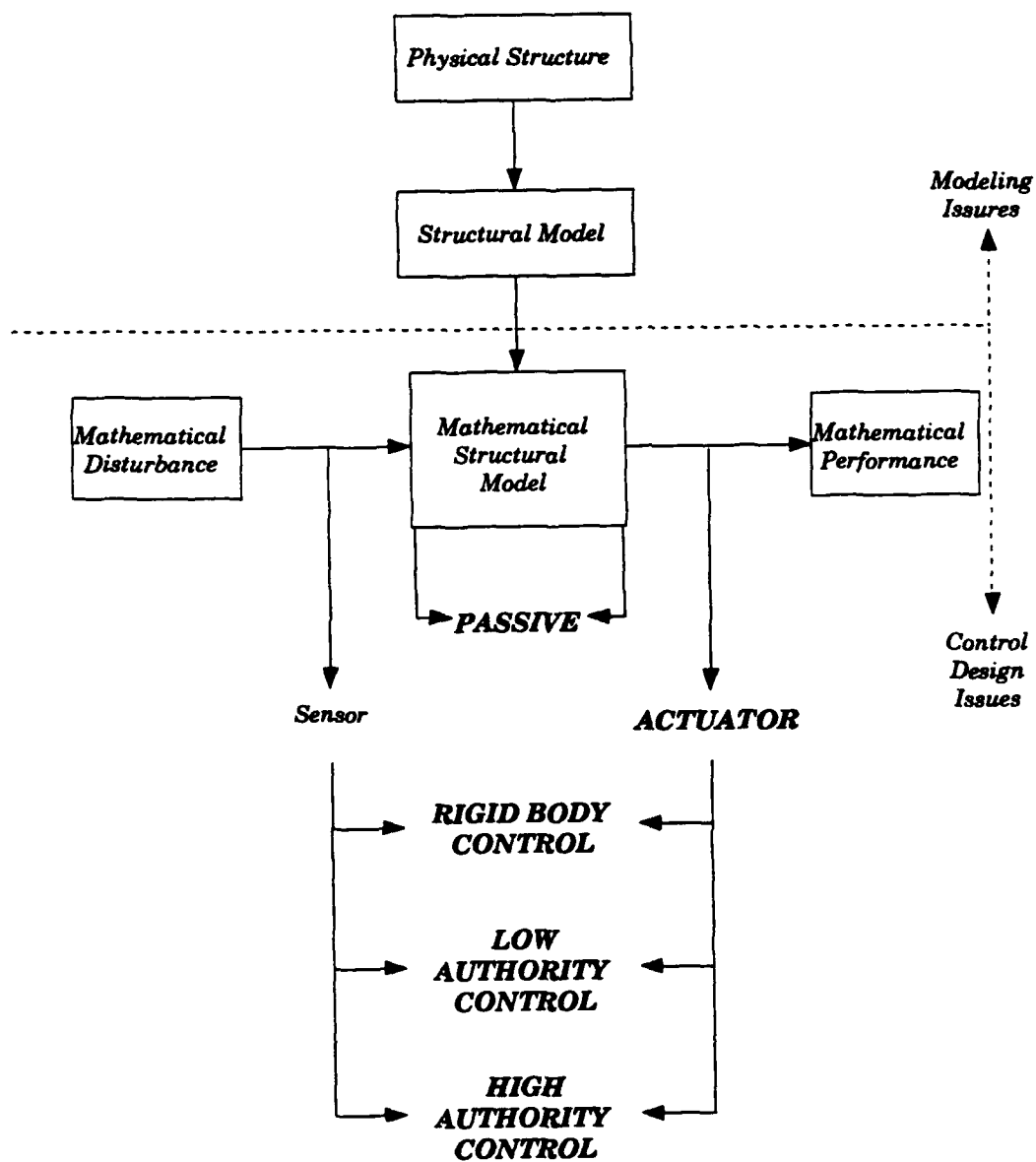
FIGURE 2.1: An Overview of the Controlled Structures Field

estimated physical parameters. In reference 10, Craig published a broad survey of recent modeling topics and techniques. Modeling provides means to predict the performance of the structure and design a control approach.

2.2.1 A 1-DOF MODEL

A 1-DOF system consisting of a single mass, spring, and dashpot is pictured in Figure 2.2. The model represents a structure with mass, M, elastic stiffness, K, and material damping, C, subjected to a disturbance force, F_d. This system is useful for illustrating several significant structural control concepts. The mathematical representation of the system is the equation of motion:

$$M\ddot{x} + C\dot{x} + Kx = F_d \qquad (2.1)$$

or:

$$\ddot{x} + 2\zeta\omega_n\dot{x} + \omega_n^2 = \frac{F_d}{M} \qquad (2.2)$$

where: $\omega_n = \sqrt{\dfrac{K}{M}}$ and $\zeta = \dfrac{C}{2\omega_n M}$ — the structure's natural frequency and damping coefficient, respectively. ζ is a function of the material damping parameter, C, which in turn is dependent on the material type, and in some instances, on the loading [11,41,48]. For a typical structure, ζ is very small (0.1–1.0%).

An analysis of the model is usually accomplished in the frequency domain or the time domain [37,51]. In the time domain, assuming the damping is negligible ($\zeta = 0$), the equation of motion can be written as two first order differential equations which together are called the state space equation:

$$\begin{Bmatrix} \dot{x} \\ \ddot{x} \end{Bmatrix} = \begin{bmatrix} 0 & 1 \\ -\omega_n^2 & 0 \end{bmatrix} \begin{Bmatrix} x \\ \dot{x} \end{Bmatrix} + \begin{Bmatrix} 0 \\ \omega_n^2 \end{Bmatrix} \frac{F_d}{K} \quad = \quad \{\dot{X}\} = [A]\{X\} + [B_d]F_d \qquad (2.3)$$

X is the state vector (i.e. displacement and velocity), **A** is the system matrix, and **B**$_d$ is the disturbance force mapping matrix which indicates how the force is directed into the states.

A frequency domain representation can be derived by taking the Laplace Transform of 2.2 with zero initial conditions:

$$\frac{X(s)}{\left[\dfrac{F_d(s)}{K} \right]} = \frac{\omega_n^2}{s^2 + \omega_n^2} = G(s) \qquad (2.4)$$

where $G(s)$ relates the dynamic displacement $X(s)$ to dynamic input $F_d(s)$ and the system parameters [37,51].

$G(s)$ is the state transfer function [37,51]. The roots of the denominator are called poles and the roots of the numerator are called zeroes. Two repeated poles are at ω_n. The physical interpretation of a pole and zero can be observed from Figure 2.3, the Bode Diagram of $G(s)$ [37,51]. The Bode magnitude and phase (i.e. the magnitude and phase angle of the sinusoidal response, X, to a sinusoidal input force, F_d) are depicted versus the complex frequency s. The peak in the magnitude and the shift in the phase occurs at ω_n. This frequency location is labeled the natural frequency, resonant frequency, or frequency of the structural mode. This frequency corresponds to a particular motion or mode shape of the structure. For the system in Figure 2.2 the mode shape is the mass moving left to right. At an undamped pole the response to a disturbance would be infinite. If material damping is included ($\zeta \neq 0$), the height of the peak and the sharpness of the phase shift are dependent on the inverse of ζ [12,37,51].
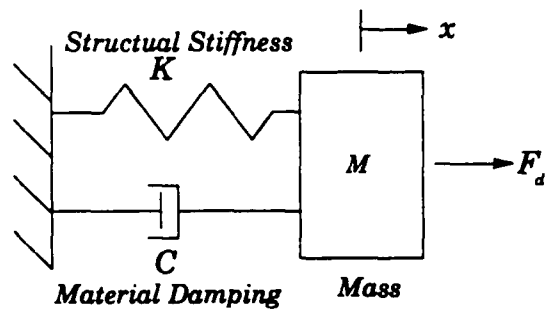
FIGURE 2.2: 1-DOF Model
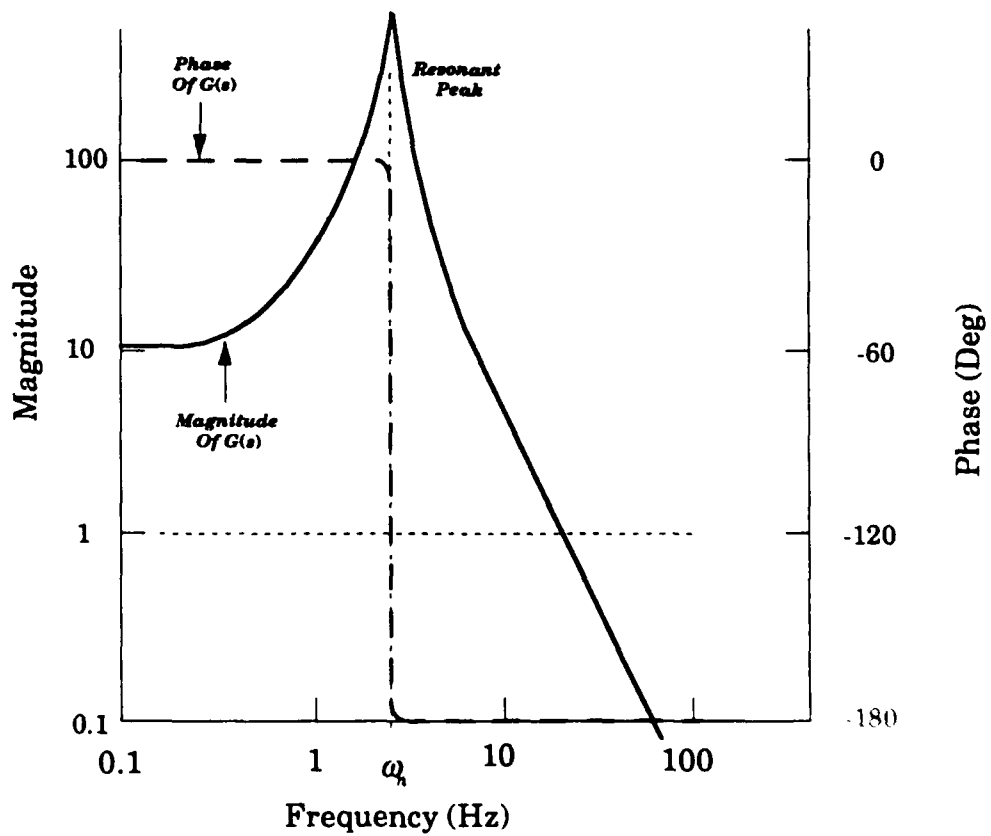
FIGURE 2.3: Bode Diagram of 1-DOF Model

At frequencies approaching infinity the response rolls off to zero at an average slope on a log-log scale of approximately the number of poles minus the number of zeroes [12].

2.2.2 A CONTROL APPROACH

The purpose of a control system is usually to minimize the performance deviations and therefore minimize the associated deviations in the structural states. This amounts to controlling the modes of the system or reducing the resonant peaks of the transfer function. Usually, the approach to control design is to damp or move the resonant peaks which are critical to the performance.

To accomplish this objective the plant or modeled system must be paired with a control approach. The scheme could be as simple as adding passive components or designing a feedback control system using actuators and sensors. The type and level of control depends on the needed performance.

Figure 2.4 depicts a typical feedback control diagram. The states are labeled X and are observed as the output of $G(s)$ caused by the input of the combined disturbance force, F_d, and an actuator, F_a. Y are the sensor outputs which are related to the states of the structure by a gain matrix C_y and are corrupted by a sensor noise N. The performance of the system, Z, is given by $C_z X$ and consists of those states which should be controlled. The compensator loop gain and the dynamics of the actuator and sensors are combined in the compensator/actuator block, $K_{AS}(s)$. The error, e, equals the difference between Y and the reference, r. If the gain and state matrices are linear and constant, the system is linear and time invariant (abbreviated LTI) [37,51].
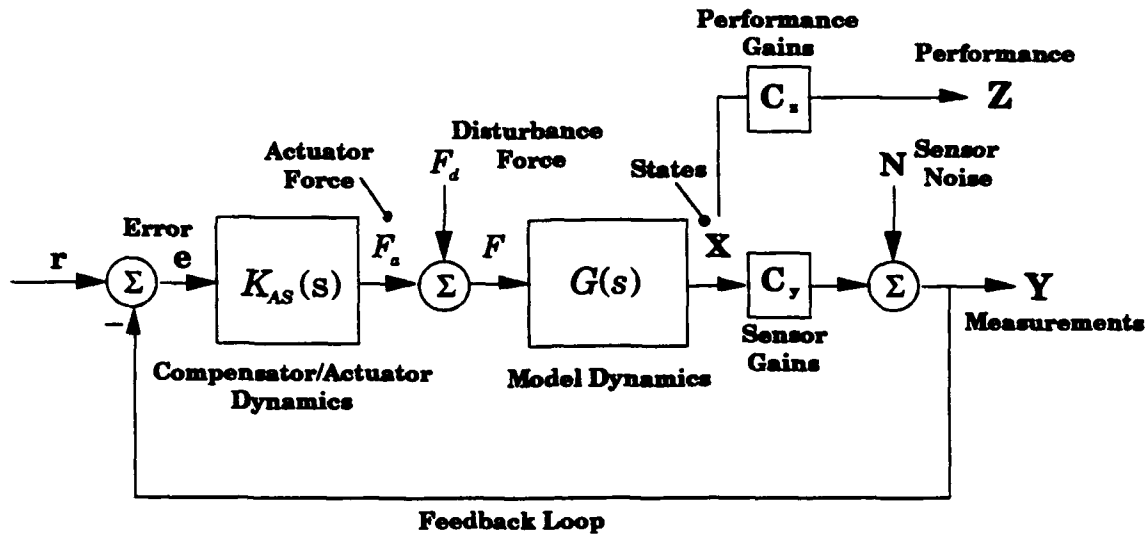
FIGURE 2.4: A Control System Diagram

To reduce the performance deviations as observed by **Z**, several types of control strategies are available, and research continues into new control strategies. However, for purposes of this discussion four generally well known approaches are examined: passive damping, rigid body control, low authority control, and high authority control.

2.2.3   PASSIVE DAMPING APPROACH

Passive damping reduces the peak of the performance transfer function by increasing the system damping, ζ. In most instances, passive damping is added before feedback control and is thus independent of the control system. Passive damping changes the system transfer function $G(s)$.

Figure 2.5 depicts a new structural model where a generic passive damping device has replaced the structural stiffness or spring element K in Figure 2.2. The damper is modeled as a pair of springs and a dashpot.

This model of a damper is representative of the passive mode of operation for the P-Strut. The device is in the load path of the structure and therefore must support the mass.
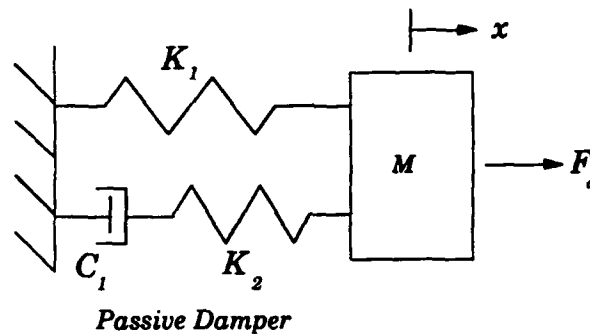
Figure 2.5: Passively Damped System Model

The purpose of the damper is to add damping to the structure over a particular bandwidth. The dashpot and springs have a characteristic damping curve which offers significant damping within a limited bandwidth. Inserting the device into the structure increases the damping coefficient of the system within the bandwidth of the device. In order to achieve the optimal reduction in the resonant peak, the frequency of maximum damping within the bandwidth should be designed to match the resonant frequency. However, if the resonant frequency moves from the peak damping frequency, the damper is mistuned. The result is less, possibly insufficient, damping.

Damping is achieved by dissipating the energy in a system. Energy can be removed from the system through a strain mechanism. For example a constrained viscoelastic layer attached to a structural member dissipates energy by shear strain. This mechanism offers reasonable damping with little mass penalty [3,39,49]. The Honeywell D-Strut—a

dashpot damper currently in operation aboard the Hubble Space Telescope—provides significant damping over a reasonable band of frequencies by displacing a fluid through a restricted passageway [2,9,14,35]. This damping concept is analogous to the P-Strut. A Piezo-resistive-shunted device, which when strained generates a voltage that is dissipated in a resistor, also offers damping over a moderate frequency range [20]. These types of passive devices have a fixed frequency at which the damping is maximum and a relatively broad band about this peak in which the damping is effective. In contrast, resonant dampers such as proof mass dampers or piezo-inductive-resistive-shunted devices are capable extracting a significant amount of energy and can be tuned to a particular frequency. However, these devices add additional modes to the system, and are only effective in a narrow band about the tuned frequency [20,29].

Although passive components are benign (i.e. they cannot add energy), they are only capable of reacting to locally perceived displacements or forces and are independent of and unaware of the global performance.

2.2.4 ACTIVE CONTROL APPROACH

An adaptive structure requires control systems which can sense and command a structural change and compensate for unwanted changes. Figure 2.6 depicts the 1-DOF Model with an actuator in parallel with the structural stiffness. The active controller or compensator, $K_{AS}(s)$, in Figure 2.4 which controls the feedback gains and thereby the actuator response, F_a, depends on the type or level of control needed.

2.2.4.1 Rigid Body Control

Rigid body control involves deploying, retracting, or positioning an object. In order to accomplish a rigid body movement, an input displacement is needed. If the mass is independent from the wall in the 1-DOF model (i.e. $K=0$ in Figure 2.6), a commanded actuator displacement would cause the mass to move to a new position and hold. If the mass were truly rigid and no disturbance force was present the movement would be precise. However, if $K \neq 0$, or the mass has additional flexibilites not shown in the figure, the movement would involve a decaying vibration or ring down around the displaced position. Preferably, an actuator would not add energy to the flexibility of the system. This can be accomplished either by input shaping, which diminishes the energy transmitted to the flexible modes of the structure by negatively reinforcing the resonant frequencies [45], or by an actuator which rolls off at frequencies lower than those of the flexibility of the mass. In a feedback control system, the measured states can be used to adjust the inputs and reposition or realign the structure via the actuator especially in the presence of disturbance force, F_d.

Ideal actuators are linear such that a feedback measurement yields a linear correction through the compensator. However, piezoceramics exhibit mild hystersis effects and electrostrictives are quadratic (or higher) with respect to the driving voltage [4,13,32,50].
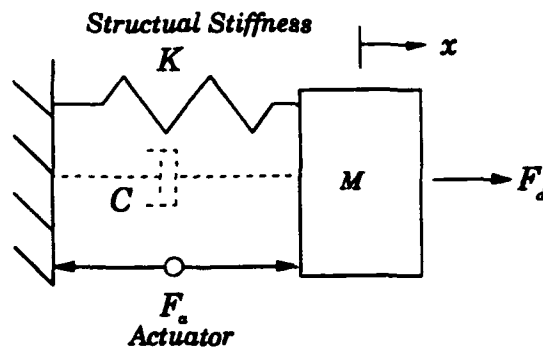
FIGURE 2.6: System Model Actuator

2.2.4.2 Low Authority Control

Low authority control (LAC) decreases the resonant peaks in Figure
2.2 by actively adding damping to the structure. The objective is similar to
that of passive damping; however, the achievable peak damping is higher
and the frequency can be tuned. A proportional derivative (PD)
compensator feeds back a measurement of the displacement and the
velocity to influence both the natural frequency and system damping [37,51].
By properly designing the compensator, the structure can be significantly
damped. A linear quadratic regulator (LQR), which is a full state feedback
controller, accomplishes the peak damping for a single mode system in the
same manner as the PD controller [12]. LQR is one type of modern control
design technique. An advantage of modern controllers is the use of the
state space representation (equation 2.3) which is optimal for computer
implementation. The deviations in performance can be written as a cost
which can be minimized by mathematical operations resulting in a stable
compensator design. [12,37,51].

Regardless of the compensator, the actuator must be capable of
commanding an input at the frequency of the mode which is to be damped.
The frequency bandwidth over which the component can actuate dictates to

what frequency and to what extent active damping is possible. If the actuator cannot command force or displacement at a particular frequency no damping or control is possible. Therefore, care must be exercised in selecting the appropriate actuator. Piezoceramic materials and electrostrictives are capable of excitation over a broad range of frequencies [46]. At frequencies out to 1K Hz, Scribner, et.al. employed a piezoelectric component to isolate transmitted disturbances in a model of a rotor blade [44]. At lower frequencies (< 25 Hz), Hallauer, et.al. used an air jet thruster alone and paired with a reaction mass actuator to damp a planar truss [22,23].

2.2.4.3 HIGH AUTHORITY CONTROL

High authority control (HAC) involves shifting the structural frequencies and altering the mode shapes of the structure [12]. HAC means moving the peak and lowering the entire curve in Figure 2.3 therefore, greatly diminishing the performance deviations. The magnitude of the commanded input must be comparable to the disturbance. In essence, HAC attempts to cancel the disturbance such that from Figure 2.6, $F_a=-F_d$. HAC can involve a multi-input-multi-output problem with many actuators and sensors. HAC compensators can be determined from frequency weighted cost functions including techniques to handle parametric uncertainties and unmodeled dynamics [12].

33

2.3 PREVIOUS APPLICATIONS OF PRESSURE ACTUATORS IN STRUCTURES

Due to the inherent bandwidth limitations on pneumatic or pressure-type actuators, structural applications have been limited. Sievers and VonFlotow appropriately dismissed pneumatic actuators in developing an isolator for damping acoustic vibrations [46]. Nevertheless, pneumatic actuators have been successfully used at low frequencies.

Rafati designed and tested a pneuma piston actuator with application to passenger trains [40]. His component was utilized in a LAC system to damp modeled disturbances transmitted f om the rail to the train. These disturbances included the accelerations due to train rocking and bouncing and occurred at frequencies below 5 Hz. The opening and closing delays in a solenoid valve limited the performance of his system.

The pneumatic air-jet developed by Hallauer and Smith—used to damp a planar truss—expelled pressurized air to generate a force (i.e. thrust). The air-jet had a limited bandwidth due to delays in opening and closing the air valve [22].

Lim, et.al. used unspecified pneumatic actuators in comparing three multi-input-multi-output control systems. The structure consisted of a fifty-one foot truss connected to a sixteen foot diameter reflector with the highest controlled frequency of 1.87 Hz [30]. His results suggested that a PD type controller with feedback to the pneumatic actuators compared favorably to other controllers.

Karnopp proposed an active and passive-active isolation system for a high-speed ground vehicle using a modern control theory approach [26].

Butsuen proposed a semi-active isolation system to isolate roadway disturbances without severely limiting an automobile's handling characteristics [7]. Since a substantial force is required over a modest bandwidth, these control systems could involve a fluid elastic actuator.

2.4 THE P-STRUT VS. PREVIOUS PRESSURE ACTUATORS

The proposed P-Strut commands a force or displacement by controlling the internal pressure in an elastic deformable cylinder. On the other hand, the piston actuator developed by Rafati used a solenoid to open and close a pressurized chamber. Hallauer's air-jet released a directed stream of high pressure air to generate on/off thrust.

The proposed fluid elastic actuator has an inherent frequency roll-off similar to other pneumatic actuators. However, in the P-Strut the bandwidth is limited by the fluid-orifice interaction, whereas in piston actuators and the air-jet, the frequency bandwidth is limited by the opening and closing of the solenoid valves [40,22]. Moreover, the viscous fluid adds passive damping qualities. When not actuating, the P-Strut is capable of absorbing energy, thus further improving the performance of the structure. In contrast, the air-jet and piston actuators are not designed to add passive damping.

CHAPTER 3:

Developing the Performance Equations

3.1 CHAPTER OUTLINE

This chapter examines the physical principles of the P-Strut and develops the mathematical equations which describe the actuator's three modes of operation: static, passive, and active.

Section 3.2 describes the dimensions of the P-Strut that are relevant to the analyses.

In Section 3.3, the pressure-strain relationships are developed via the stress-strain constitutive equations for isotropic and anisotropic materials. The axial elongation of the structure is determined as a function of the input force and input stroke. These equations define the static performance of the actuator. Anisotropic material properties are shown to enhance the performance.

Section 3.4 investigates the damping interaction between the viscous fluid and the orifice. An effective loss coefficient is estimated by

considering laminar and turbulent channel flows. In addition, accelerating and sinusoidally varying pressure flows are examined.

A mechanical analysis details the passive mode of operation and leads to a three parameter model in Section 3.5. The parameters include discrete elastic and volumetric stiffnesses, as well as a dashpot representation of the fluid-orifice interaction. The physical and mathematical development indicates that these stiffnesses compete against one another reducing the passive damping. The P-Strut performance is compared to the Honeywell D-Strut and piezoelectric resistive-shunted struts. The passive model is updated to include the additional damping encountered during testing. The revised model based on the measured performance has damping which overwhelms the predicted orifice damping.

Section 3.6 examines the active performance of the P-Strut. A second discrete stiffness model is developed with similar physical parameters. Mathematically and physically, the model defines the non-collocated transfer function between the input force and the actuation displacement. The static performance, as well as the frequency roll-off due to the fluid and orifice, are properly incorporated into the model. A parameteric study demonstrates the important parameters.

3.2. DEFINITION OF THE P-STRUT GEOMETRY

Figure 3.1 depicts a schematic of the P-Strut. The fluid-elastic actuator is a circular cylindrical pressure vessel which is sealed with rigid flat-plate endcaps. The fluid inside the cylinder is connected via an orifice to the fluid inside the reservoir or flexible bellows.

The cylindrical actuator has a length L, with inner radius R_i, outer radius R_o, and thickness t. R_c represents the average radius or $(1/2)(R_i + R_o)$. Since $t << R_c$, the three radii are approximately equal (i.e. $R_o \approx R_c \approx R_i$). Thus, the cross-sectional area, A_c, and the annulus or vessel wall area, A_{ac}, can be expressed as:

$$A_c = \pi R_i^2 \approx \pi R_c^2$$

$$A_{ac} = \pi(R_o^2 - R_i^2) \approx 2\pi R_c t$$

(3.1)

The bellows is depicted in Figure 3.2. The reservoir or bellows has an effective cross-sectional area A_b. This dimension is difficult to compute from the geometry of the bellows. (In this study, A_b is determined directly from the experimental results.)

The orifice has cross-sectional area A_o and length L_o.

The ratio of the P-Strut cross-sectional area, A_c, to the effective bellows area, A_b, equals the fluid lever introduced in Chapter 1. This fluid lever is represented by Ψ_b. The ratio of A_c to the area of the orifice, A_o, is defined as Ψ_o. A_b divided by A_o equals Ψ_{ob}. As equations:

$$\Psi_b = \frac{A_c}{A_b} \qquad \Psi_o = \frac{A_c}{A_o} \qquad \Psi_{ob} = \frac{\Psi_o}{\Psi_b} = \frac{A_b}{A_o}$$

(3.2)
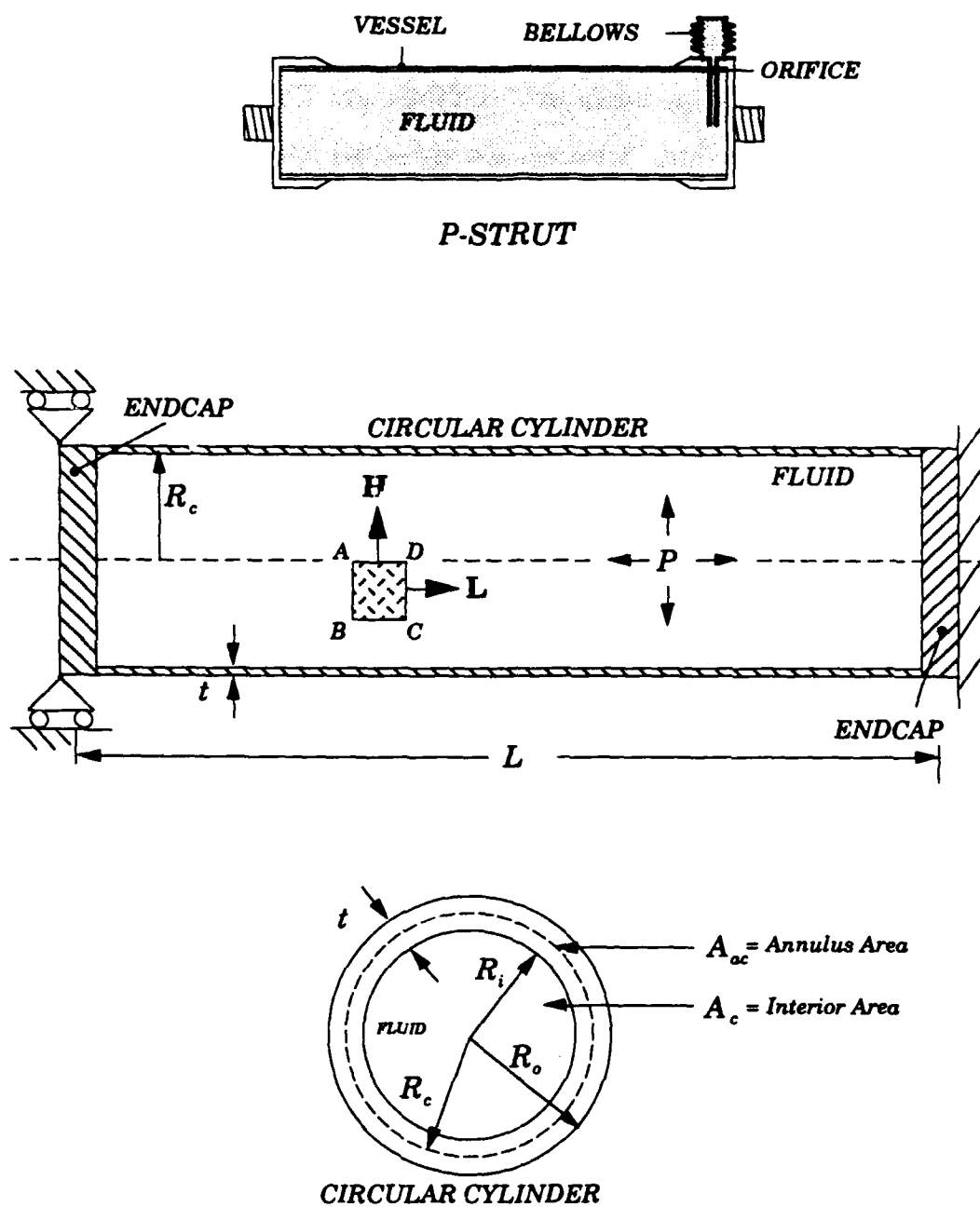
FIGURE 3.1: Description of the P-Strut Geometry

Figure 3.3 depicts the element *ABCD* extracted from the surface of the P-Strut cylinder illustrated in Figure 3.1. The longitudinal direction is labeled **L** or **1** and the hoop direction is labeled **H** or **2**. The curvature of the element in the hoop direction is R_c. The element is not curved with respect to the longitudinal direction.

3.3   DERIVATION OF THE STATIC EQUATIONS

As established in Chapter 1, the P-Strut is an elastically deformable pressure vessel. The static analysis derives the elongation of the P-Strut (i.e. actuation authority) as functions of the input force and stroke.

3.3.1 CONSTITUTIVE EQUATIONS

In general, the application of an arbitrary load induces normal and shear stresses in the cylinder wall which can be described in the **1**, **2**, and **3** coordinate directions. However, since the thickness of the cylinder, t, is much smaller than the radius, R_c, the stresses through the thickness are negligible (i.e. σ_{12}, σ_{23}, and $\sigma_{33}=0$). With this plane-stress state assumption, the constitutive equations are:

$$\begin{Bmatrix} \sigma_{11} \\ \sigma_{22} \\ \sigma_{12} \end{Bmatrix} = \begin{bmatrix} E_{1111} & E_{1122} & 2E_{1112} \\ E_{1122} & E_{2222} & 2E_{2212} \\ E_{1112} & E_{2212} & 2E_{1212} \end{bmatrix} \begin{Bmatrix} \varepsilon_{11} \\ \varepsilon_{22} \\ \varepsilon_{12} \end{Bmatrix} \tag{3.3}$$

or abbreviated:

$$\{\sigma\} = [E]\{\varepsilon\} \tag{3.4}$$
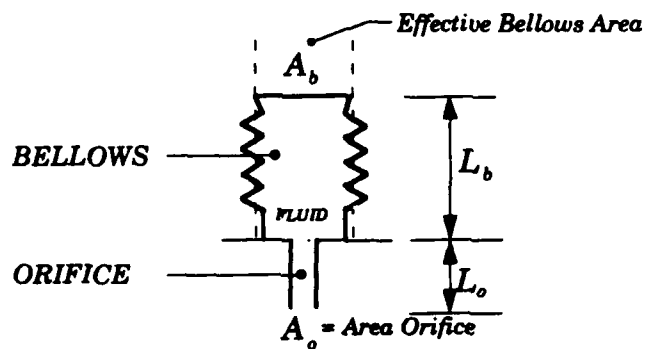
FIGURE 3.2: P-Strut Bellows and Orifice Geometry
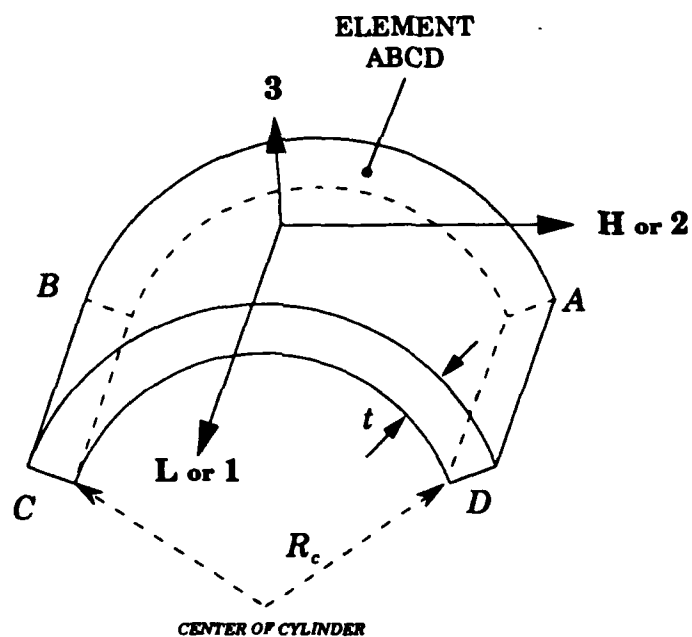
FIGURE 3.3: Definition of Longitudinal (1) and
Hoop (2) Coordinate Directions

The components of the **E** matrix represent the cylinder's material properties. The 2 appears in the last column of **E** since the tensor strain, ε_{12}, instead of the engineering strain, γ_{12}, is used.

If a pair of orthogonal planes of material property symmetry exists, the material is categorized as orthotropic. Defining the material properties in these orthogonal or principle directions, $E_{1112} = E_{2212} = 0$. This eliminates the coupling between the normal stresses and the shear strain. Rewriting matrix equation 3.3 with orthotropic material constants, yields:

$$
\begin{Bmatrix} \sigma_{11} \\ \sigma_{22} \\ \sigma_{12} \end{Bmatrix} = \begin{bmatrix} E_{1111} & E_{1122} & 0 \\ & E_{2222} & 0 \\ sym & & 2E_{1212} \end{bmatrix} \begin{Bmatrix} \varepsilon_{11} \\ \varepsilon_{22} \\ \varepsilon_{12} \end{Bmatrix} \tag{3.5}
$$

Equation 3.5 can be expressed in terms of the vessel wall's engineering properties as:

$$
\begin{Bmatrix} \sigma_{11} \\ \sigma_{22} \\ \sigma_{12} \end{Bmatrix} = \left(\frac{1}{1 - v_{12} v_{21}} \right) \begin{bmatrix} E_{11} & v_{21} E_{11} & 0 \\ & E_{22} & 0 \\ sym & & 2G_{12}(1 - v_{12} v_{21}) \end{bmatrix} \begin{Bmatrix} \varepsilon_{11} \\ \varepsilon_{22} \\ \varepsilon_{12} \end{Bmatrix} \tag{3.6}
$$

where E_{11} and E_{22} are the Young's Modulii and v_{12} and v_{21} are the Poisson's Ratios in the 1 and 2 coordinate directions. These four engineering constants are related by the expression $v_{12} E_{22} = v_{21} E_{11}$.

Inverting and expanding matrix equation 3.6 to solve for the strains:

$$
\begin{Bmatrix} \varepsilon_{11} \\ \varepsilon_{22} \\ \varepsilon_{12} \end{Bmatrix} = \begin{bmatrix} C_{1111} & C_{1122} & 0 \\ & C_{2222} & 0 \\ sym & & 2C_{1212} \end{bmatrix} \begin{Bmatrix} \sigma_{11} \\ \sigma_{22} \\ \sigma_{12} \end{Bmatrix} \tag{3.7}
$$

where the compliances are defined as:

$$C_{1111} = \frac{1}{E_{11}} \qquad\qquad C_{2222} = \frac{1}{E_{22}}$$

$$C_{1122} = -\frac{v_{12}}{E_{11}} = -\frac{v_{21}}{E_{22}} \qquad\qquad C_{1212} = \frac{1}{4G_{12}} \qquad (3.8)$$

For an isotropic material, $E_{11}=E_{22}=E$, $v_{12}=v_{21}=v$, and $G_{12}=E/[2(1+v)]$. Thus, only two constants are required to characterize the constitutive relationships for a material such as aluminum. Combining 3.8 and 3.7, the isotropic longitudinal strain can be written as:

$$\varepsilon_{11} = \frac{1}{E}(\sigma_{11} - v\sigma_{22}) \qquad (3.9)$$

and the hoop strain as:

$$\varepsilon_{22} = \frac{1}{E}(\sigma_{22} - v\sigma_{11}) \qquad (3.10)$$

An actuator constructed from composites would, in general, have anisotropic material characteristics. Composite laminates are manufactured from individual plies which posses material properties aligned in their fiber and transverse fiber directions. In order to determine the material properties in the laminate reference frame (1-2), the contribution from each ply must be considered.

From Figure 3.4, a ply coordinate system (1'-2') is defined at an angle, φ, from the laminate coordinate frame. In the 1'-2' directions, the ply orthotropic material constants, $E'_{\alpha\beta\gamma\nu}$, are defined as:

$$E'_{1111} = \frac{E'_{11}}{1 - v'_{12}v'_{21}} \qquad\qquad E'_{2222} = \frac{E'_{22}}{1 - v'_{12}v'_{21}}$$

$$E'_{1122} = \frac{v'_{21}E'_{11}}{1 - v'_{12}v'_{21}} \qquad\qquad E'_{1212} = G'_{12} \qquad (3.11)$$
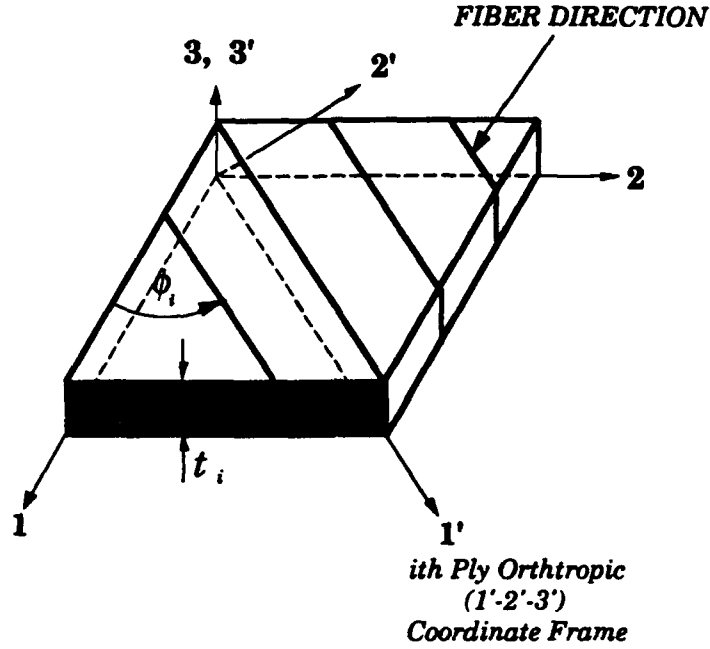
FIGURE 3.4: Typical Composite Laminate Layup

To transform the ith ply's $E'_{\alpha\beta\gamma\nu}{}^i$ into the **1-2 laminate frame, four** invariant constants are needed [17,25].

$$I_1 = (1/4)[E'_{1111}{}^i + E'_{2222}{}^i + 2E'_{1122}{}^i]$$
$$I_2 = (1/8)[E'_{1111}{}^i + E'_{2222}{}^i - 2E'_{1122}{}^i + 4E'_{1212}{}^i]$$
$$I_3 = (1/2)[E'_{1111}{}^i - E'_{2222}{}^i]$$
$$I_4 = (1/4)[E'_{1111}{}^i + E'_{2222}{}^i - 2E'_{1122}{}^i - 4E'_{1212}{}^i]$$

$$(3.12)$$

With these invariants, the ith ply's material constants are transformed into the **1-2 coordinate system:**

$$E_{1111}{}^i = I_1 + I_2 + I_3 \cos(2\,\varphi_i) + I_4 \cos(4\,\varphi_i)$$
$$E_{2222}{}^i = I_1 + I_2 - I_3 \cos(2\,\varphi_i) + I_4 \cos(4\,\varphi_i)$$
$$E_{1122}{}^i = I_1 - I_2 - I_3 \cos(4\,\varphi_i)$$
$$E_{1212}{}^i = I_2 - I_3 \cos(4\,\varphi_i)$$
$$E_{1112}{}^i = (I_3/2) \sin(2\,\varphi_i) + I_4 \sin(4\,\varphi_i)$$
$$E_{2212}{}^i = (I_3/2) \sin(2\,\varphi_i) - I_4 \sin(4\,\varphi_i)$$

$$(3.13)$$

With the rotated $E_{\alpha\beta\gamma\upsilon}{}^{i}$ in the laminate coordinate frame, a thickness weighted stiffness matrix, **A**, can be determined by adding individually the stiffnesses of equation 3.13 multiplied by the ith ply's thickness:

$$A_{\alpha\beta\gamma\upsilon} = \int_{t_{i-1}}^{t_i} E_{\alpha\beta\gamma\upsilon}{}^{i}\,dt = \sum_{i=1}^{\# \, plies}(E_{\alpha\beta\gamma\upsilon}{}^{i})t_i \qquad (3.14)$$

The average laminate stresses, σ^L, are defined as:

$$\begin{Bmatrix} \sigma_{11}^L \\ \sigma_{22}^L \\ \sigma_{12}^L \end{Bmatrix} = \left(\frac{1}{t}\right)\begin{bmatrix} A_{1111} & A_{1122} & 2A_{1112} \\ & A_{2222} & 2A_{2212} \\ sym & & 2A_{1212} \end{bmatrix}\begin{Bmatrix} \varepsilon_{11} \\ \varepsilon_{22} \\ \varepsilon_{12} \end{Bmatrix} \qquad (3.15)$$

or, abbreviated:

$$\{\sigma^L\} = \frac{1}{t}\,[A]\{\varepsilon\} \qquad (3.16)$$

For a balanced laminate, where the number of $-\varphi$ plies equals the number of $+\varphi$ plies, $A_{1112}=A_{2212}=0$ (i.e. the material is quasi-orthotropic).

Inverting 3.16 for the strain vector:

$$\{\varepsilon\} = t\,[A]^{-1}\{\sigma^L\} \qquad (3.17)$$

Assuming a balanced laminate, equation 3.17 can be expanded as:

$$\begin{Bmatrix} \varepsilon_{11} \\ \varepsilon_{22} \\ \varepsilon_{12} \end{Bmatrix} = \frac{t}{\Delta}\begin{bmatrix} A_{2222}A_{1212} & -A_{1122}A_{1212} & 0 \\ & A_{1111}A_{1212} & 0 \\ sym & & (A_{1111}A_{2222} - A_{1122}^2)/4 \end{bmatrix}\begin{Bmatrix} \sigma_{11}^L \\ \sigma_{22}^L \\ \sigma_{12}^L \end{Bmatrix} \qquad (3.18)$$

where $\Delta = A_{1212}(A_{1111}A_{2222} - A_{1122}^2)$

Equation 3.18 is analogous to equation 3.7. Defining the effective laminate compliance matrix C^L as:

$$[C^L] = t\,[A]^{-1} \qquad (3.19)$$

45

the effective or "smeared" laminate engineering properties can be determined from equation 3.8 as:

$$E_{11}^L = \frac{1}{C_{1111}^L} \qquad\qquad E_{22}^L = \frac{1}{C_{2222}^L}$$

$$v_{12}^L = -E_{11}^L C_{1122}^L \qquad\qquad v_{21}^L = -E_{22}^L C_{1122}^L \qquad (3.20)$$

$$G_{12}^L = \frac{1}{4C_{1212}^L}$$

where the elements of $\mathbf{C}^L$ are defined in equation 3.7.

With 3.17 and 3.20, the longitudinal and hoop strains are defined as:

$$\varepsilon_{11} = \frac{1}{E_{11}^L}(\sigma_{11}^L - v_{12}^L \sigma_{22}^L) \qquad (3.21)$$

$$\varepsilon_{22} = \frac{1}{E_{22}^L}(\sigma_{22}^L - v_{21}^L \sigma_{11}^L) \qquad (3.22)$$

3.3.2   PRESSURE -STRAIN RELATIONSHIPS

As illustrated in Figure 3.5, the longitudinal and hoop stresses acting in the walls of a thin pressurized cylinder are:

$$\sigma_{11}^L = \frac{PR_c}{2t} \qquad (3.23)$$

$$\sigma_{22}^L = \frac{PR_c}{t} \qquad (3.24)$$

These equations are derived by equilibrating the forces acting in the **1** and **2** directions (i.e. the pressure force versus the stresses in the cylinder wall).

Substituting 3.23 and 3.24 into the isotropic strain equations 3.9 and 3.10 yields the longitudinal strain as a function of the internal pressure:

$$\varepsilon_{11} = \frac{PR_c}{2tE}(1 - 2v) \qquad (3.25)$$
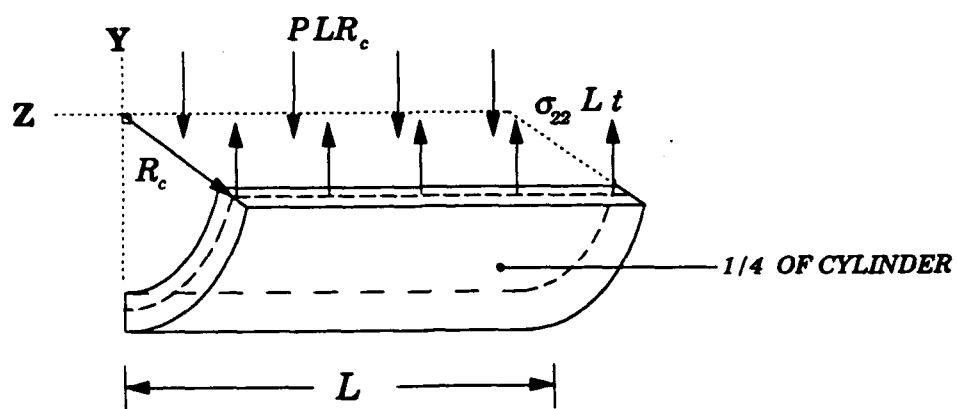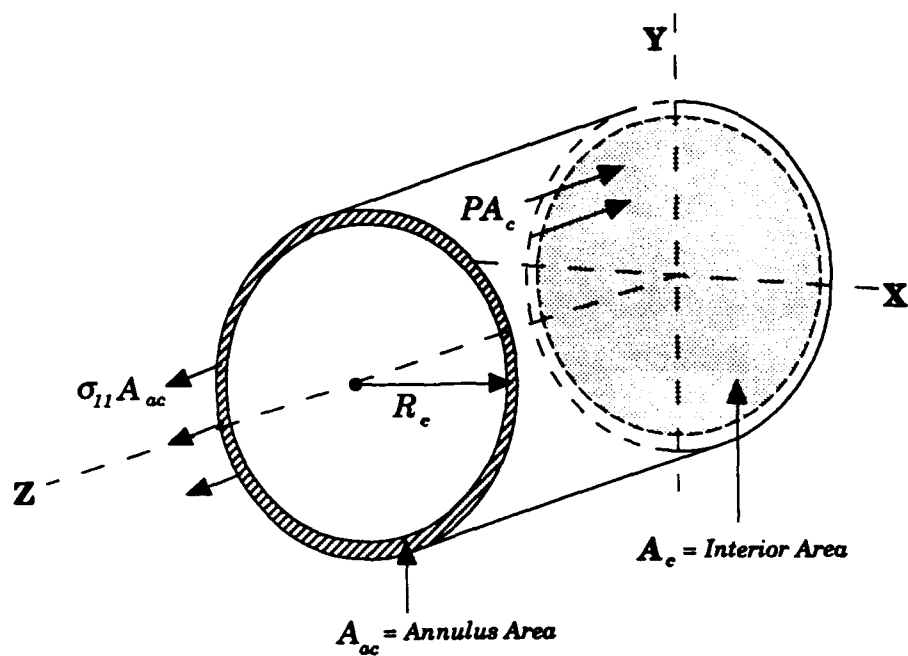
FIGURE 3.5: Pressurized Circular Cylinder

and the hoop strain:

$$\varepsilon_{22} = \frac{PR_c}{2tE}(2-v) \tag{3.26}$$

Similarly, substituting 3.23 and 3.24 into the quasi-orthotropic strain equations 3.21 and 3.22 results in the composite longitudinal and hoop strains:

$$\varepsilon_{11} = \frac{PR_c}{2tE_{11}^L}(1-2v_{12}^L) \tag{3.27}$$

$$\varepsilon_{22} = \frac{PR_c}{2tE_{22}^L}(2-v_{21}^L) \tag{3.28}$$

The ratio of longitudinal to hoop strain is defined as Γ. The isotropic strain ratio, Γ_i, equals 3.25 divided by 3.26, or:

$$\Gamma_i = \frac{\varepsilon_{11}}{\varepsilon_{22}} = \frac{(1-2v)}{(2-v)} \tag{3.29}$$

The ratio of the composite strains, equation 3.27 versus 3.28, is defined as:

$$\Gamma_c = \frac{\varepsilon_{11}}{\varepsilon_{22}} = \frac{E_{22}^{\ L}(1-2v_{12}^{\ L})}{E_{11}^{\ L}(2-v_{21}^{\ L})} \tag{3.30}$$

3.3.3 DERIVATION OF THE ACTUATION AUTHORITY, INPUT FORCE, AND STROKE REQUIREMENTS

From the elementary definition of strain, the actuation displacement of the P-Strut, δ_L, is given by:

$$\delta_L = L_{eff}\varepsilon_{11} \tag{3.31}$$

where L_{eff} is the effective length of the actuator. The effective length is the length over which the longitudinal strain acts plus a contribution due to the end conditions. Near the boundaries the pressure-stress equations 3.23 and

3.24 are not valid. In order to satisfy compatibility at the boundaries, additional moment and shear stress-resultants, acting out of the 1-2 coordinate plane, must exist. These resultants can be solved using linear Shell Bending Theory which predicts a dramatic increase in ε_{11} near the end conditions [16,27]. In essence, the clamped-rigid endcaps physically restrict the radial swelling or the hoop strain of the vessel (see Figure 3.6). As the hoop strain is diminished near the boundary, the local longitudinal strain is increased due to Poisson's effect.

Figure 3.7 depicts the strains as a function of the position calculated using a complete Shell Bending Theory solution. The peaks in ε_{11} near the ends of the cylinder correspond to the end effects and the reduction in hoop strain while the dominating plateau in ε_{11} is the strain predicted by the elementary pressure-strain equations 3.25 or 3.27. Therefore, over the majority of the cylinder the simplified pressure-strain equations 3.25 and 3.26 or 3.27 and 3.28 are valid; only near the ends does the solution require the more complicated bending theory approach. The Shell Bending Theory solution is reported in Appendix A and analyzed extensively (for isotropic and anisotropic cylinders) by Graves in reference 18.

The elongation, δ_L, equals the longitudinal strain integrated over the length of the P-Strut. The peaks in ε_{11} at the boundaries are accounted for by adding an amount ϖ to the physical length of the P-Strut, L, i.e.:

$$L_{eff} = L(1 + \varpi) \tag{3.32}$$

49
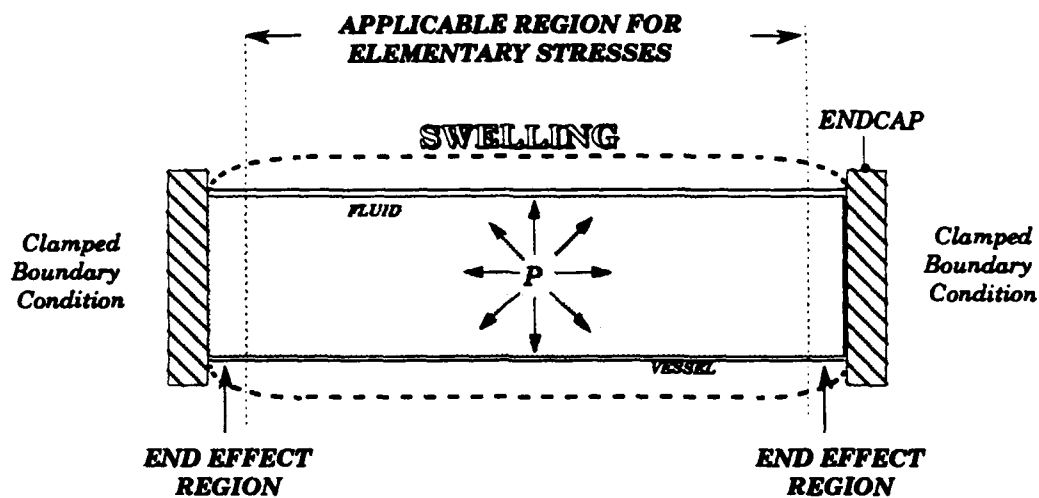
FIGURE 3.6: P-Strut Radial Swelling and End Effects
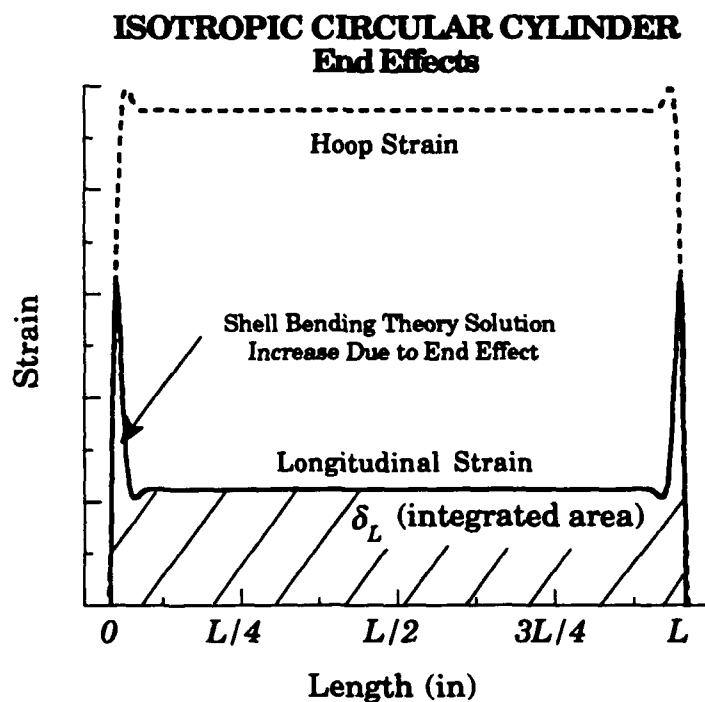
FIGURE 3.7: Pressurized Isotropic Circular Cylinder End Effects

3.3.4 VOLUMETRIC CHANGES AND INPUT FORCE/STROKE REQUIREMENTS

Since ε_{11} and ε_{22} are both positive for a positive pressure increase, the vessel grows with pressure. Figure 3.8 depicts, for a circular cylindrical actuator, the longitudinal elongation or the actuation displacement, δ_L. In addition, the radial expansion or dilation is labeled δ_R.

Th volume change in the longitudinal direction is simply the interior cross-sectional area of the actuator multiplied by the actuation authority:

$$\Delta V_L = A_c \delta_L \tag{3.33}$$

The hoop dilation, as drawn in Figure 3.7, equals the P-Strut's circumferential expansion:

$$\delta_R = R_c \varepsilon_{22} \tag{3.34}$$

The associated radial volume increase is given by:

$$\Delta V_R = [(R_c + \delta_R)^2 - R_c^2]\, \pi L \approx 2\pi R_c \delta_R L \tag{3.35}$$

From Figure 3.7, the bending theory end effect has little influence on the hoop strain. Therefore, the hoop strain is assumed effective over a length L and not magnified nor reduced by the end effect.

The final volume to consider is the volume change of the fluid due to the internal pressure. The compression of the fluid volume, V_f, as a function of the pressure equals:

$$\Delta V_f = \frac{V_f P}{B_f} = \frac{A_c L P}{B_f} \tag{3.36}$$

where B_f equals the bulk modulus of the fluid.

Summing the volume changes together yields:

$$\Delta V_{total} = \Delta V_L + \Delta V_R + \Delta V_f \qquad (3.37)$$

As illustrated in Figure 3.9, to maintain a fluid balance within the P-Strut, the total sum of the volume changes in the cylinder must equal the volume change in the fluid reservoir. The fluid in the bellows is assumed incompressible and the cross-sectional area of the bellows, A_b, is assumed constant. (The relatively small volume of fluid in the bellows experiences an insignificant amount of compression.) Thus, the input force stroke is defined as:

$$\delta_b = \frac{\Delta V_{total}}{A_b} \qquad (3.38)$$

The input force, F_b, is related to the stiffness of the flexible bellows and the internal bellows pressure. Defining the spring stiffness of the bellows as K_b and noting that the displacement equals δ_b, the input force required, without the fluid, is $K_b \delta_b$. With the fluid present, the opposing pressure force equals PA_b. Summing these together yields the required input force:

$$F_b = K_b \delta_b + PA_b \qquad (3.39)$$

3.3.5   STATIC EQUATIONS FOR AN ISOTROPIC CIRCULAR CYLINDER

Substituting equation 3.25 into 3.31 and 3.26 into 3.34 yields for an isotropic P-Strut the axial displacement (i.e. actuation authority):

$$\delta_L = L_{eff} \frac{PR_c}{2tE}(1 - 2v) \qquad (3.40)$$

and the radial dilation:

$$\delta_R = R_c \frac{PR_c}{2tE}(2 - v) \qquad (3.41)$$

Δ VOLUME
LONGITUDINAL
(ΔV_L)

P

L δ_L

R_c

δ_R
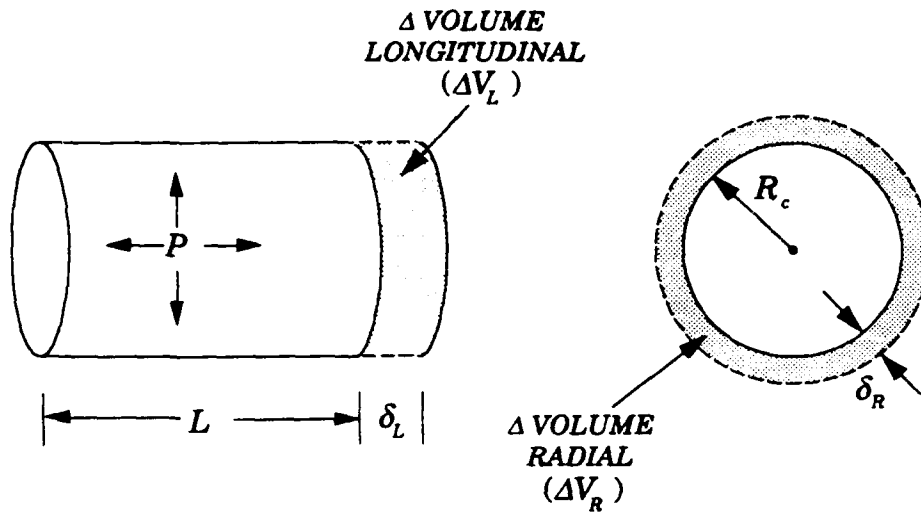
Δ VOLUME
RADIAL
(ΔV_R)

FIGURE 3.8: Longitudinal and Radial Volume Changes

CYLINDER
VOLUME
CHANGE
(ΔV_{total})

FLEXIBLE FLUID
RESERVOIR

INPUT FORCE

RESERVOIR
VOLUME
CHANGE
(ΔV_{total})

ORIFICE

ORIGINAL
VOLUME
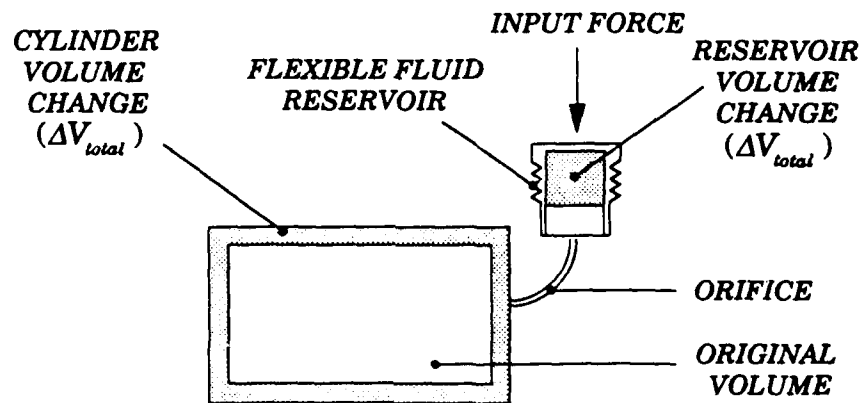
FIGURE 3.9: Total Volume Change and Input Stroke

Inserting equations 3.33, 3.35, and 3.36 into 3.37 yields:

$$\Delta V_{total} = \delta_L A_c + \delta_R 2\pi R_c L + \frac{P}{B_f} A_c L \qquad (3.42)$$

By substituting 3.40 and 3.41 into 3.42 and simplifying using 3.1, the total volume change as a function of the pressure is determined as:

$$\Delta V_{total} = PA_c \left\{ \frac{R_c}{2tE} \left[L_{eff}(1-2v) + 2L(2-v) \right] + \frac{L}{B_f} \right\} \qquad (3.43)$$

From equation 3.38 and 3.43, the input stroke, δ_b, equals:

$$\delta_b = P\Psi_b \left\{ \frac{R_c}{2tE} \left[L_{eff}(1-2v) + 2L(2-v) \right] + \frac{L}{B_f} \right\} \qquad (3.44)$$

where Ψ_b equals the ratio of the interior cross-sectional area of the cylinder to the effective area of the bellows as defined in equation 3.2. Substituting equation 3.44 into equation 3.39 yields the input force as a function of the pressure:

$$F_b = P \left\{ K_b \Psi_b \left[\frac{R_c}{2Et} [L_{eff}(1-2v) + 2L(2-v)] + \frac{L}{B_f} \right] + A_b \right\} \qquad (3.45)$$

Solving equation 3.40 for the pressure, P, yields:

$$P = \delta_L \frac{2tE}{L_{eff} R_c (1-2v)} \qquad (3.46)$$

Noting the definition of the isotropic strain ratio, Γ_i in equation 3.29 and using equation 3.46, equation 3.44 can be rewritten as:

$$\delta_b = \delta_L \Psi_b \left\{ 1 + \frac{2L}{L_{eff} \Gamma_i} + \frac{2tE\, L}{(1-2v)L_{eff} R_c B_f} \right\} \qquad (3.47)$$

54

To determine the input force as a function of the actuation authority, equations 3.46 and 3.47 are substituted into 3.39 to yield:

$$F_b = \delta_L \left\{ K_b \Psi_b \left[1 + \frac{2L}{L_{eff} \Gamma_i} + \frac{2tE\,L}{(1-2v)L_{eff}R_cB_f} \right] + \frac{2tE\,A_b}{(1-2v)L_{eff}R_c} \right\} \quad (3\,48)$$

Therefore, the actuation authority can be determined as a function of the input stroke and input force by inverting 3.47 and 3.48 respectively, i.e.:

$$\delta_L = \frac{\delta_b}{\Psi_b \left[1 + \frac{2L}{L_{eff} \Gamma_i} + \frac{2tE\,L}{(1-2v)L_{eff}R_cB_f} \right]} \quad (3.49)$$

and

$$\delta_L = \frac{F_b}{K_b \Psi_b \left[1 + \frac{2L}{L_{eff} \Gamma_i} + \frac{2tE\,L}{(1-2v)L_{eff}R_cB_f} \right] + \frac{2tE\,A_b}{(1-2v)L_{eff}R_c}} \quad (3.50)$$

From studying the preceding equations, several important observations can be made. First, the static performance equations 3.47 through 3.48 linearly relate the inputs force, F_b, and stroke, δ_b, to the actuation displacement, δ_L. Second, the area ratio, Ψ_b, amplifies a small input force into a larger pressure force in the cylinder (equation 3.45) at the cost of increasing the input stroke, δ_b, per elongation, δ_L (equation 3.47 or 3.49). This effect is analogous to a mechanical lever.

In equation 3.47, the first term represents the axial response, the second the hoop swelling, and the third the fluid compression. If, as is typical, L/L_{eff} is approximately one and the fluid is nearly incompressible, the necessary bellows stroke scales as $1+2/\Gamma_i$. Since the isotropic strain ratio, Γ_i, is less than one for common isotropic materials, the hoop strain significantly diminishes the static performance. For aluminum, $\Gamma_i \approx 0.25$;

therefore, ε_{11} is only 25% of ε_{22}. Even worse, the radial volume dilation is approximately an order of magnitude greater than the longitudinal volume elongation $(1+2/\Gamma_i = 9)$. This isotropic volume effect translates directly into a much higher input stroke, δ_b, per unit δ_L. The required input force, F_b, is determined primarily by the last term in equation 3.48 because the bellows stiffness, K_b, is generally small. The cylinder material properties, geometry, and effective bellows area, A_b, affect F_b. A larger A_b, and a larger effective stiffness $E/(1-2\nu)$, or smaller cylinder dimensions act to increase the required F_b per unit δ_L. A large F_b over a long δ_b requires an input force generator which is capable of a high force over a long stroke—a limiting combination.

The detrimental radial volume dilation and the higher effective stiffness (i.e. $E/(1-2\nu)$) are results of the isotropic material properties. If the effective material's Young's Modulii were greater in the hoop direction than the longitudinal direction and the Poisson's Ratio was reduced, the isotropic disadvantages could be alleviated. This revelation suggests the use of tailored composite materials to achieve a cylinder stiffer in the hoop than in the longitudinal direction.

3.3.6 THE STATIC EQUATIONS FOR AN ANISOTROPIC CYLINDER

The same process which was followed to derive the static equations for an isotropic P-Strut can be generalized to the anisotropic cylinder.

The actuation authority, δ_L, and the radial dilation, δ_R, are defined from substituting equations 3.27 into 3.31 and 3.28 into 3.34.

$$\delta_L = L_{eff} \frac{PR_c}{2tE_{11}^L}(1-2\nu_{12}^L) \tag{3.51}$$

and

$$\delta_R = R_c \frac{PR_c}{2tE_{22}^L}(2 - v_{21}^L) \qquad (3.52)$$

The total volume change, ΔV_{total}, was given in 3.42. Substituting 3.51 and 3.52 into 3.42 and using 3.38 yields the input stroke, δ_b, as a function of the pressure, P:

$$\delta_b = P\Psi_b \left\{ \frac{R_c}{2t} \left[\frac{L_{eff}}{E_{11}^L}(1-2v_{12}^L) + \frac{2L}{E_{22}^L}(2-v_{21}^L) \right] + \frac{L}{B_f} \right\} \qquad (3.53)$$

Solving equation 3.51 for P, inserting the result into 3.53, and substituting Γ_c from 3.30, the input stroke, δ_b, as a function of the elongation, δ_L, equals:

$$\delta_b = \delta_L \Psi_b \left\{ 1 + \frac{2L}{L_{eff}\Gamma_c} + \frac{2tE_{11}^L L}{(1-2v_{12}^L)L_{eff}R_c B_f} \right\} \qquad (3.54)$$

Substituting 3.54 into 3.39, and again using 3.51 solved for P, yields the anisotropic input force to actuation authority relationship.

$$F_b = \delta_L \left\{ K_b \Psi_b \left[1 + \frac{2L}{L_{eff}\Gamma_c} + \frac{2tE_{11}^L L}{(1-2v_{12}^L)L_{eff}R_c B_f} \right] + \frac{2tE_{11}^L A_b}{(1-2v_{12}^L)L_{eff}R_c} \right\} \qquad (3.55)$$

Equations 3.54 and 3.55 could be inverted to solve for the elongation in terms of the input stroke and force. These relationships would be analogous to equations 3.49 and 3.50 in the isotropic case.

The advantage of tailoring the laminate properties is obvious from equations 3.30, 3.54, and 3.55. For a given axial stiffness, increasing the hoop stiffness, and/or adjusting the Poisson's Ratios, increases Γ_c. In addition, tailoring the Poisson's Ratios minimizes the required input force. This implies, in comparison to the isotropic case, less force and stroke will

57

be wasted on radial dilation and consequently, less force and stroke will be required for longitudinal actuation.

Intuitively, the hoop stiffness can be increased by manufacturing composite P-Struts with the fibers running in the hoop direction. However, blindly increasing $E_{22}{}^L$ versus $E_{11}{}^L$ without considering other performance issues can lead to less optimal actuator designs. Chapter 4 investigates the optimal composite properties.

3.4   ANALYSIS OF VISCOUS FLUID-ORIFICE DAMPING

In the passive and active modes of operation, the viscous fluid is forced in and out of an orifice. As the fluid flows through the orifice or channel, it undergoes a shearing action which dissipates energy. This loss of energy is the source of damping in the P-Strut.

The frictional shear losses can be estimated with analytical and experimental channel flow solutions. If the flow is assumed incompressible (i.e. constant density), steady (i.e. the fluid properties are constant in time), and fully developed (i.e. the velocity profile is uniform along the length of the channel), the energy dissipated by shearing can be related to a mechanical dashpot as depicted in Figure 3.10. The dashpot coefficient, C, associates the damping with the physical properties of the fluid and the dimensions of the orifice. The retarding force in the dashpot—C multiplied by the average fluid velocity, V_o—equals the pressure force lost, ΔP, due to the fluid shearing:

$$CV_o = \Delta PA_o \tag{3.56}$$

where A_o equals the cross-sectional area of the orifice ($A_o = \pi D_o^2 / 4$). The dashpot representation is used in both the passive and active modeling of the following sections.

3.4.1 LAMINAR HAGEN-POISEUILLE CHANNEL FLOW

If the fluid flows in smooth layers and no macroscopic mixing occurs, the flow is laminar. Figure 3.10 depicts the fluid in a two-dimensional circular orifice or channel. Due to the forces acting on the fluid including a constant pressure gradient and the shear stress, a parabolic velocity profile develops. Summing these forces, the pressure difference between locations **1** and **2** can be defined as a function of the orifice length, L_o, diameter, D_o, fluid absolute viscosity, μ, and average channel velocity, V_o, as:

$$\Delta P = P_1 - P_2 = 32 \frac{L_o}{D_o} \frac{\mu V_o}{D_o} \tag{3.57}$$

where reference 33 or 53 details the derivation.

From an energy balance the differential pressure can be expressed as a function of the head loss, h_{lam}, and the fluid density, ρ, as:

$$\Delta P = h_{lam}\rho \tag{3.58}$$

From equations 3.57 and 3.58:

$$h_{lam} = 32 \frac{L_o}{D_o} \frac{\mu V_o^2}{\rho V_o D_o} = 32 \frac{L_o}{D_o} \frac{V_o^2}{Re} \tag{3.59}$$

The Reynold's Number, $Re = \rho V_o / \mu$, is a non-dimensional parameter which characterizes the flow. If $Re \leq 2300$, the flow is considered laminar.

C_{lam} can be defined by combining equations 3.56 and 3.57 as:
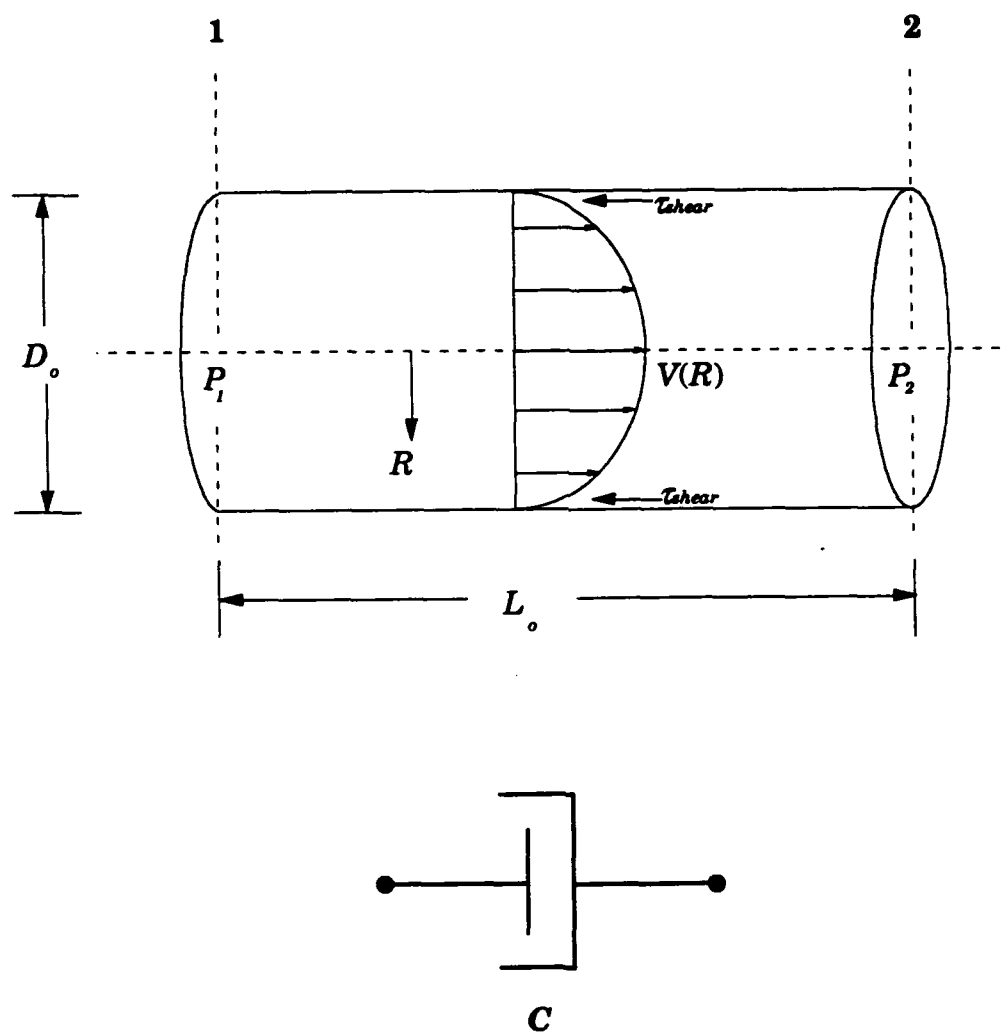
FIGURE 3.10: A Circular Orifice with Viscous Fluid Flow
And the Mechanical Dashpot Representation

$$C_{lam} = 8\pi\mu L \qquad (3.60)$$

Therefore, C_{lam} is a function of the length and fluid absolute viscosity with units of force-seconds per length. Interestingly, the orifice diameter does not influence C_{lam}.

3.4.2   TURBULENT FULLY-DEVELOPED CHANNEL FLOW

The fluid is considered turbulent, such that macroscopic mixing of the fluid layers occurs, if the Reynold's Number is greater than 2300. By virtue of the nature of turbulence, the analytical solutions available are for very specific mixing problems. Blasius proposed the following equation for the turbulent head loss in a smooth pipe [33]:

$$h_{turb} = \frac{0.1582}{Re^{0.25}} \frac{L_o}{D_o} V_o^2 \qquad (3.61)$$

where $Re \leq 10^5$. From the definition of C:

$$C_{turb} = \frac{0.1582}{Re^{0.25}} \frac{L_o}{D_o} \rho V_o A_o = \frac{0.0396}{Re^{0.25}} \pi L_o D_o \rho V_o \qquad (3.62)$$

The turbulent dashpot coefficient, C_{turb}, is a function of the orifice diameter and the average velocity within the turbulent channel flow. C_{turb}'s dependence on V_o makes applying C_{turb} difficult, since the mechanical dashpot force would be a non-linear function of V_o. A non-linear dashpot coefficient is difficult (and not practical) to incorporate into the linear dynamic models developed for the passive and active modes of operation in the following sections.

3.4.3   ACCELERATING AND OSCILLATING CHANNEL FLOWS

The laminar and turbulent dashpot coefficients (equations 3.60 and 3.62) were derived assuming a fully developed flow. However, time and

distance along the channel are required to achieve a developed velocity profile. The entrance or development length, L_{dev}, for laminar flows equals approximately $D_o Re/150$ [33]. For turbulent flows, L_{dev} ranges from 25 to 50 diameters [33]. Thus in a short orifice, the flow never reaches a fully developed state. The time to achieve a developed velocity profile, t_{dev}, depends on the pressure flow condition. For the preceding constant-pressure-gradient laminar and turbulent flows, t_{dev} can be approximated by dividing the estimated L_{dev} by the average channel flow velocity, V_o.

The actual pressure gradient in the P-Strut orifice is dynamic. The external forces (i.e. the input force, F_b, or the disturbance force, F_d,—see Figure 1.2) generate dynamic fluid flow. If the force instantaneously accelerates the fluid flow, the time to attain fully developed flow, t_{dev}, can be estimated from the non-dimensional parameter, $t_{dev}^{\bullet}$, proposed by Szymanski and published in reference 53:

$$t_{dev}^{\bullet} = \frac{4\upsilon}{D_o^2} t_{dev} \qquad (3.63)$$

where υ is defined as the kinematic viscosity, μ/ρ. When the development time, t_{dev}, has progressed (measured from zero at the instant the force was applied) such that $t_{dev}^{\bullet} \approx 0.75$, the fluid is essentially laminar [53].

If the pressure gradient (i.e. the input or disturbance force) is sinusoidally applied at a frequency ω, the fluid responds sinusoidally. Sexl and Unchida [53] derived a solution utilizing a non-dimensional frequency, $\omega_{dev}^{\bullet}$, where:

$$\omega_{dev}^{\bullet} = \frac{\omega D_o^2}{4\upsilon} \qquad (3.64)$$

If ω_{dev}^{*} is small ($\omega_{dev}^{*} < 1$), the fluid velocity is essentially quasi-static and the laminar, Hagen-Poiseuille equations are applicable [53].

For example, a DOW Corning 200 series silicon fluid—a fluid used in the P-Strut—has an kinematic viscosity rated at 15.5 in²/s (10K centistokes) [15]. If the orifice diameter is assumed to be 70 mil (1.8 mm):

$$Re = (4.6 \times 10^{-3})V_o$$

$$t_{dev}^{*} = (12.6 \times 10^{3})t_{dev} \qquad (3.65)$$

$$\omega_{dev}^{*} = (7.9 \times 10^{-5})\omega_{dev}$$

The channel velocity, V_o, would need be 0.5×10^6 in/s to classify as turbulent flow. Only 59 microseconds are required to develop laminar flow from the initiation of an input or disturbance force. Moreover, the dynamic forcing frequency, ω, would need be on the order of 1K Hz to negate the use of a quasi-laminar solution. Therefore, the laminar flow equations and C_{lam} seem appropriate to the P-Strut's passive and active analyses.

3.4.4   OTHER FLUID/ORIFICE CONSIDERATIONS

Certainly, the P-Strut's hand-drilled orifice is not smooth. However, due to the high viscosity of the P-Strut fluid and consequently the low Re, the roughness effects are assumed to be negligible [33].

In addition, the orifice is not tapered and thus the inlet and exit areas do not uniformly transition into the reservoir or vessel. As a result, the fluid flow expands or contracts dramatically at the ends of the orifice. These events increase the fluid head loss. For a square-edged orifice (i.e. flat exit with no taper) an additional head loss, h_{end}, as great as $0.25V_o^2$ can be present [33].

The dashpot equations developed in the passive and active models of the following sections do not consider the head loss due to the square-edged orifice exits.

3.5   PASSIVE PERFORMANCE

The passive performance of the P-Strut relates a collocated structural disturbance, F_d, to an elongation (or compression), δ_L. The proposed fluid elastic actuator, operating in its passive mode, exhibits the properties of a viscous damper. These properties can be ascertained by examining the mechanical behavior and developing a model of the P-Strut.

3.5.1   AN ANALYSIS OF THE MECHANICAL BEHAVIOR

Figure 3.11 depicts a schematic of the P-Strut subjected to a disturbance force, F_d. F_d is in equilibrium with the longitudinal stress in the cylinder wall and the pressure force inside the cylinder:

$$F_d = \sigma_{11}^L A_{\alpha c} - PA_c \tag{3.66}$$

The average hoop stress $\sigma_{22}{}^L$, associated with the pressure increase, was reported in equation 3.24. Solving 3.66 for $\sigma_{11}{}^L$ and substituting $\sigma_{11}{}^L$ and $\sigma_{22}{}^L$ into equations 3.27 and 3.28 yields for the longitudinal and hoop strains:

$$\varepsilon_{11} = \frac{PR_c}{2tE_{11}^L}(1 - 2\,v_{12}^L) + \frac{F_d}{E_{11}^L A_{\alpha c}} \tag{3.67}$$

and, noting $v_{12}{}^L E_{22}{}^L = v_{21}{}^L E_{11}{}^L$:

$$\varepsilon_{22} = \frac{PR_c}{2tE_{22}^L}(2 - v_{21}^L) - \frac{v_{12}^L F_d}{E_{11}^L A_{\alpha c}} \tag{3.68}$$

64
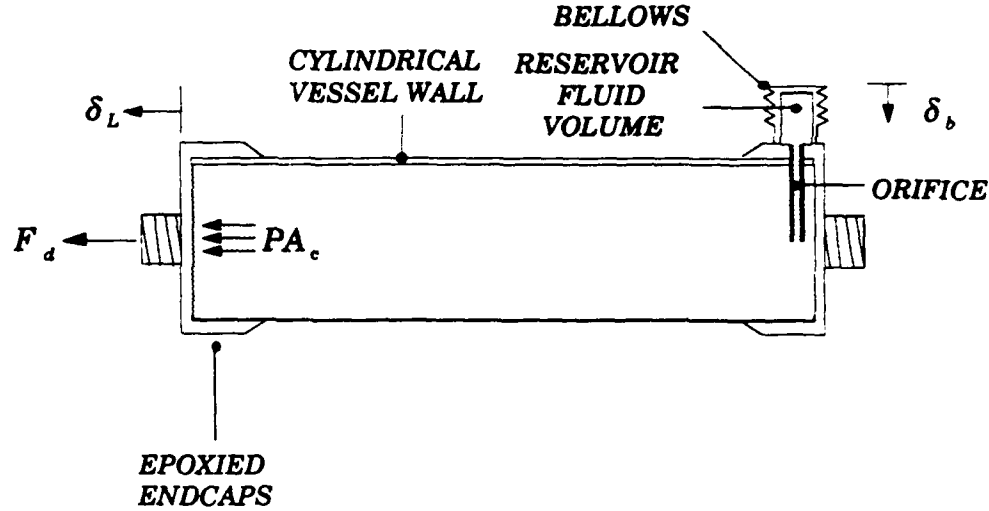
FIGURE 3.11: P-Strut Schematic in Passive Mode of Operation

The elongation of the cylinder is defined in equation 3.31 as the longitudinal strain multiplied by the length; Thus, substituting 3.67 into 3.31 defines the elongation of the P-Strut as a function of the pressure and disturbance force:

$$\delta_L = \varepsilon_{11} L = \frac{PR_cL}{2tE_{11}^L}(1 - 2v_{12}^L) + \frac{F_dL}{E_{11}^LA_{oc}} \tag{3.69}$$

where L is used instead of the effective length, L_{eff}, to simplify the development. Typically, the effective length correction factor, ϖ (equation 3.32), is very small (i.e. $L_{eff}{\approx}L$). Moreover, if rigorous, separate effective length corrections would have to be included for radial swelling and axial loading.

The total volume change for the cylinder due to the combined pressure and force loading can be represented by inserting 3.67 into 3.33, 3.68 into 3.35, and substituting the results along with 3.36 into 3.37:

$$\Delta V_{total} = A_c \left[\frac{PR_cL}{2tE_{11}^L}(1-2v_{12}^L) + 2\frac{PR_cL}{2tE_{22}^L}(2-v_{21}^L) + \frac{PL}{B_f} + \frac{(1-2v_{12}^L)F_dL}{E_{11}^LA_{oc}} \right] \quad (3.70)$$

The first three terms are similar to the static analysis—the cylinder grows with increasing pressure. The last term indicates that a disturbance force also acts to expand the cylinder, increasing the volume.

Since within the actuator the fluid volume is conserved, the total volume change in the cylinder must be balanced by an equal volume change in the fluid reservoir (see Figure 3.8). From 3.38 the reservoir stroke, δ_b, is determined by dividing 3.70 by the effective area of the bellows, A_b:

$$\delta_b = \Psi_b \left[\frac{PR_cL}{2tE_{11}^L}(1-2v_{12}^L) + \frac{PR_cL}{tE_{22}^L}(2-v_{21}^L) + \frac{PL}{B_f} + \frac{(1-2v_{12}^L)F_dL}{E_{11}^LA_{oc}} \right] \quad (3.71)$$

where Ψ_b equals the area ratio of the cylinder to the bellows (equation 3.2).

Assuming no input force (F_b=0), the pressure in the bellows, P_b, must be in equilibrium with the bellows static stiffness, K_b, and stroke, δ_b. From equation 3.39, $K_b\delta_b = -P_bA_b$. In addition, the pressure in the cylinder, P, must be in equilibrium with the pressure in the bellows and the pressure loss due to the fluid-orifice interaction. As an equation,

$$P = P_b + \Delta P = -\frac{K_b\delta_b}{A_b} + \Delta P \quad (3.72)$$

With equation 3.56, equation 3.72 can be rewritten as:

$$P = -\frac{K_b\delta_b}{A_b} + \frac{CV_o}{A_o} \quad (3.73)$$

where C (assuming laminar flow) is defined in equation 3.60 and V_o is the velocity of the fluid flowing from the cylinder through the orifice and into the bellows. The velocity equals the rate of bellows displacement multiplied by the area ratio of the bellows to the orifice, Ψ_{ob} (equation 3.2). The area

66

ratio represents the velocity increase as the flow leaves a larger reservoir area and enters a small orifice. In Laplace notation, $V_o = -\Psi_{ob} s \delta_b$. Substituting into 3.73 and multiplying by the area of the cylinder, the pressure force, PA_c, can be expressed as:

$$PA_c = -\delta_b A_c \left(\frac{K_b}{A_b} + \frac{\Psi_{ob} Cs}{A_o} \right) \tag{3.74}$$

Rearranging 3.74 and simplifying with the area ratios defined in equation 3.2, the bellows stroke as a function of the pressure can be defined as:

$$\delta_b = \frac{-PA_c}{(\Psi_b K_b + \Psi_o \Psi_{ob} Cs)} \tag{3.75}$$

Substituting equation 3.75 into 3.71 and solving for the pressure as a function of the disturbance force yields:

$$P = -F_d \left[\frac{\dfrac{(1 - 2 v_{12}^L) L}{E_{11}^L A_{ac}}}{\dfrac{R_c L}{2t E_{11}^L}(1 - 2 v_{12}^L) + \dfrac{R_c L}{t E_{22}^L}(2 - v_{21}^L) + \dfrac{L}{B_f} + \dfrac{A_c}{\Psi_b(\Psi_b K_b + \Psi_o \Psi_{ob} Cs)}} \right] \tag{3.76}$$

Inserting equation 3.76 into 3.69 and dividing the numerator and denominator by A_c defines the elongation of the P-Strut as a function of the disturbance force.

$$\delta_L = F_d \left[\frac{L}{E_{11}^L A_{ac}} - \frac{\dfrac{(1 - 2 v_{12}^L) R_c L}{2t E_{11}^L A_c} \dfrac{(1 - 2 v_{12}^L) L}{E_{11}^L A_{ac}}}{\dfrac{(1 - 2 v_{12}^L) R_c L}{2t E_{11}^L A_c} + \dfrac{(2 - v_{21}^L) R_c L}{t E_{22}^L A_c} + \dfrac{L}{B_f A_c} + \dfrac{1}{\Psi_b(\Psi_b K_b + \Psi_o \Psi_{ob} Cs)}} \right] \tag{3.77}$$

Equation 3.77 represents the dynamic compliance of the system (δ_L versus F_d). Simplifying, the expression into a function of stiffnesses with physical definitions, yields:

$$\delta_L = F_d \left[\frac{1}{K_S} - \frac{\dfrac{1}{K_L^2}}{\dfrac{1}{K_L} + \dfrac{1}{K_R} + \dfrac{1}{K_f} + \dfrac{1}{\Psi_b^2 K_b + \Psi_o^2 Cs}} \right] \qquad (3.78)$$

where K_L equals the longitudinal stitfness associated with the pressure-induced axial elongation:

$$K_L = \frac{A_{oc} E_{11}^L}{L(1 - 2v_{12}^L)} \qquad (3.79)$$

K_R corresponds to the hoop or radial dilation due to the pressure:

$$K_R = \frac{A_{oc} E_{22}^L}{2L(2 - v_{21}^L)} \qquad (3.80)$$

K_f is the fluid volumetric stiffness which comes directly from the compressibility of the fluid:

$$K_f = \frac{B_f A_c}{L} \qquad (3.81)$$

K_S represents the P-Strut's axial or structural stiffness:

$$K_S = \frac{E_{11}^L A_{oc}}{L} \qquad (3.82)$$

Having defined these stiffnesses based on physical effects, the performance equations developed with just the mechanical properties could be redeveloped with these stiffnesses. For example, the input stroke, δ_b, could be redefined from equation 3.71 as:

$$\delta_b = \Psi_b \left\{ PA_c \left[\frac{1}{K_L} + \frac{1}{K_R} + \frac{1}{K_f} \right] + \frac{F_d}{K_L} \right\} \qquad (3.83)$$

68

3.5.2 DISCRETE PASSIVE STIFFNESS MODEL

Inverting the compliance transfer function, equation 3.78, and simplifying yields the passive stiffness transfer function, K_{pass}, which is a function of the complex frequency s:

$$K_{pass}(s) = \frac{F_d}{\delta_L} = \frac{K_L^2 K_S (cs + k_b + K_P)}{(K_L^2 - K_S K_P)(cs + k_b) + K_L^2 K_P} \qquad (3.84)$$

where:
$$K_P = \frac{1}{\dfrac{1}{K_L} + \dfrac{1}{K_R} + \dfrac{1}{K_f}} = \frac{K_L K_R K_f}{K_L K_R + K_R K_f + K_f K_L} \qquad (3.85)$$

$c = \Psi_o^2 C$ and $k_b = \Psi_b^2 K_b$.

Figure 3.12 depicts a three parameter stiffness model representative of the fluid elastic actuator's passive performance. A dynamic disturbance force, F_d, is transmitted directly through the stiffness labeled K_1 and in parallel through the series spring and dashpot, K_2 and C_1 respectively.

The transfer function relating the structural disturbance force, F_d, to the axial expansion, δ_L, of the modeled system equals:

$$\frac{F_d}{\delta_L} = K_{pass}(s) = K_1 \frac{(1 + \dfrac{K_2}{K_1}) C_1 s + K_2}{C_1 s + K_2} \qquad (3.86)$$

The springs K_1 and K_2 and the dashpot C_1 do not correspond one-to-one with the physical stiffnesses and the dasphot given in equation 3.84. Nevertheless, the modeled springs and the dashpot can be expressed as functions of the physical stiffnesses, K_L, K_S, K_P, k_b, and c as follows:

$$K_1 = K_S \frac{K_L^2(k_b + K_P)}{(K_L^2 - K_P K_S)k_b + K_L^2 K_P}$$

$$K_2 = \frac{K_L^2 K_P^2 K_S^2}{(K_L^2 - K_P K_S)[k_b(K_L^2 - K_P K_S) + K_L^2 K_P]} \qquad (3.87)$$

$$C_1 = c \frac{(K_L^2 K_P^2 K_S^2)}{[k_b(K_L^2 - K_P K_S) + K_L^2 K_P]^2}$$

From equation 3.87 and Figure 3.12, the static load path, K_1, is primarily determined by the structural stiffness of the cylinder, K_S. If the fluid is not present (i.e. K_P=0), K_1 reduces to K_S. In practice, the presence of the fluid contributes a small amount of additional stiffness. The second modeled spring, K_2 is a complex combination of all of the physical stiffnesses present in the system. The dashpot coefficient, C_1, represents the orifice damping, c, scaled by a complicated stiffness factor.
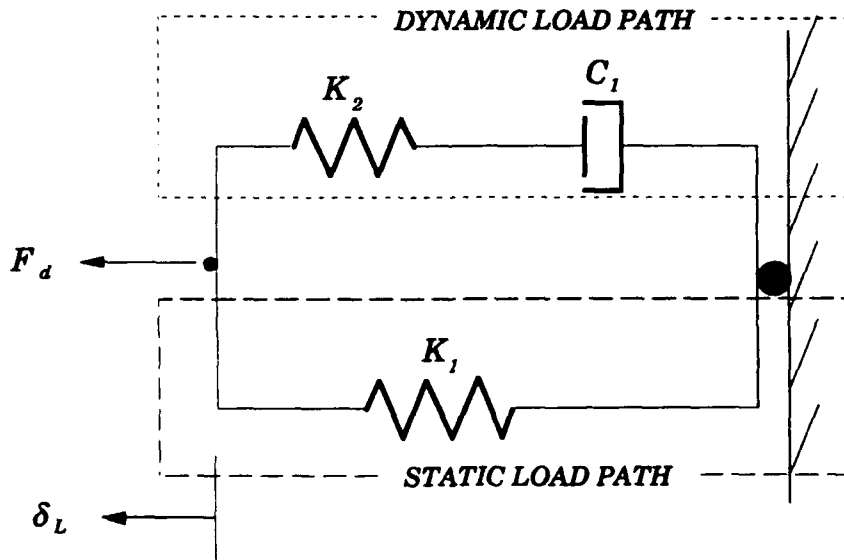
FIGRUE 3.12: Passive Discrete Stiffness Model

3.5.3 PASSIVE FREQUENCY CHARACTERISTICS

Equation 3.86 expressed in pole-zero form equals:

$$K_{pass}(s) = K_{DCp} \frac{\omega_p}{\omega_z} \left(\frac{s + \omega_z}{s + \omega_p} \right) \tag{3.88}$$

The magnitude of K_{pass} at $s=0$ (the DC gain), is labeled K_{DCp}. K_{DCp} equals K_1. From equations 3.86 and 3.88, the pole, ω_p, and zero, ω_z, are determined as:

$$\omega_z = \frac{K_2}{C_1}$$

$$\omega_z = \frac{K_1 K_2}{C_1 (K_1 + K_2)} \tag{3.89}$$

The passive frequency characteristics of the P-Strut in terms of the physical stiffnesses, K_L, K_P, K_S, k_b, and c are calculated from equations 3.87, 3.88, and 3.89. These properties are reported in Table 3.1.

The frequency performance can be illustrated with a Bode Diagram. Assuming a sinusoidal displacement $\delta_L = \delta_{Lo} e^{i\omega t}$, K_{pass} can be written as:

$$K_{pass}(\omega) = \delta_{Lo} M(\omega) e^{i \phi(\omega)} \tag{3.90}$$

where $M(\omega)$ equals the magnitude and $\phi(\omega)$ equals the phase of K_{pass}. $M(\omega)$ and $\phi(\omega)$ are defined in Table 3.1. Figure 3.13 depicts the Bode magnitude and phase of K_{pass} (equation 3.90). This figure was calculated using the representative physical properties found in Table 3.2.

TABLE 3.1: Passive Frequency Characteristics

CHARACTERISTIC	PARAMETERS
DC Stiffness, K_{DC_p}	$K_S \dfrac{K_L^2(k_b + K_P)}{k_b(K_L^2 - K_P K_S) + K_L^2 K_P}$
Stiffness at Infinity, K_{∞_p}	$\dfrac{K_L^2 K_S}{K_L^2 - K_P K_S} = K_{DC_p}\beta$
Frequency of Zero, ω_z	$\dfrac{k_b + K_P}{c}$
Frequency of Pole, ω_p	$\dfrac{(K_L^2 - K_P K_S)k_b + K_L^2 K_P}{c(K_L^2 - K_P K_S)}$
Bandwidth, B_W	$\omega_p - \omega_z$
Maximum Loss Factor, η^*	$\dfrac{\beta - 1}{2\sqrt{\beta}}$
Frequency, ω^*	$\omega_z \sqrt{\beta} = \sqrt{\omega_z \omega_p}$
Bode Magnitude, $M(\omega)$	$K_{DC_p}\beta \sqrt{\dfrac{1 + \dfrac{\omega^2}{\omega_z^2}}{\dfrac{\omega^2}{\omega_z^2} + \beta^2}}$
Bode Phase, $\phi(\omega)$	$\tan^{-1}\left[\dfrac{(\beta - 1)\dfrac{\omega}{\omega_z}}{\beta + \dfrac{\omega^2}{\omega_z^2}}\right]$

where $\quad \beta = \dfrac{\omega_p}{\omega_z} = \dfrac{(K_L^2 - K_P K_S)k_b + K_L^2 K_P}{(k_b + K_P)(K_L^2 - K_P K_S)}$

PASSIVE PERFORMANCE
Magnitude (Stiffness) vs Frequency

Stiffness At Infinity

DC Stiffness

Stiffening Due To Orifice

PASSIVE PERFORMANCE
Phase vs Frequency

Peak Due to Orifice
(Peak Frequency and
Peak Damping)
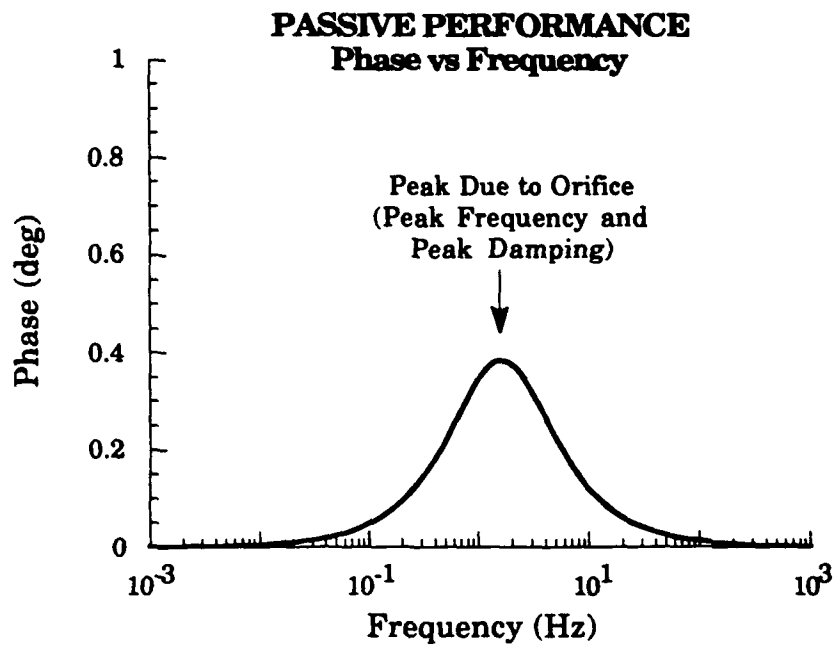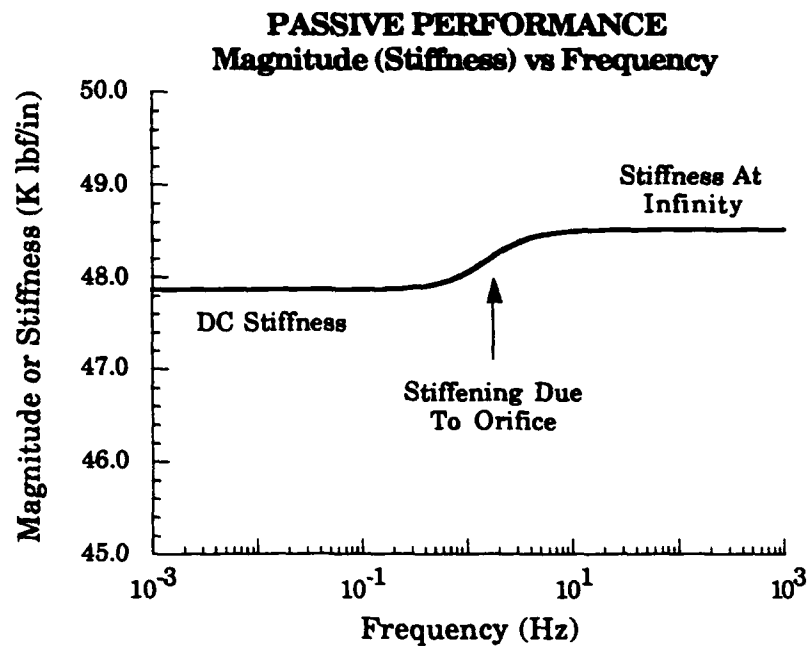
FIGURE 3.13: Passive Performance (K_{pass}) Bode Diagrams: Magnitude and Phase Versus Frequency

The passive performance follows a classic pattern. K_{pass} begins with a value of K_{DCp} at $s=0$ and exhibits a region of increasing stiffness until leveling off at $K_{\infty p}$. This rise in magnitude is accompanied by an associated bell-shape change in phase.

Physically, the fluid flowing through the orifice or dashpot begins at DC with no motion. The dashpot has an effective zero stiffness, $cs=0$. At low frequencies, the fluid is pushed through the orifice by the displacement. Due to fluid drag in the orifice, the phase of the displacement lags the force. As the frequency increases, the fluid begins to "lock-up" the dashpot. The phase lag of the displacement begins to diminish as less fluid flows through the orifice. At high frequencies, the fluid is unable to displace through the orifice and the dashpot approaches an effective infinite stiffness. At each extreme, the frequency dependence of K_{pass} is removed since cs becomes "constant". The rise in the magnitude of K_{pass} corresponds to the "locking-up" of the dashpot.

Two important parameters are the peak loss factor, η^*, which represents a measure of the maximum damping achievable, and the peak frequency, ω^*, which equals the frequency at which η^* occurs. The loss factor is commonly defined for viscous damping as:

$$\eta(\omega) = \frac{Energy\ Dissipated\ /\ Cycle}{2\pi\ Maximum\ Energy\ Stored\ /\ Cycle} = \tan\phi(\omega) \qquad (3.91)$$

η is proportional to the structural damping coefficient, ζ (see Chapter 2). For LTI systems with a sinusoidal disturbance, $\eta=2\zeta$ [12]. By differentiating 3.91 to locate the maximum of $\eta(\omega)$, η^* and ω^* can be defined as reported in Table 3.1.

To optimally damp a particular structural mode at a frequency ω_i, ω^* should be made equal to ω_i. Furthermore, the larger the damping bandwidth, the more tolerable the damping is to uncertainty in ω_i and potentially the more structural modes which can be damped. The bandwidth, B_w, is defined as the difference between the pole and zero frequencies (i.e. approximately the frequency region under the bell-shaped phase plot).

3.5.4 PARAMETERIC STUDY OF THE PASSIVE PERFORMANCE

Table 3.2 details the results of a parameteric study of the passive model. The reference values are based on realistic physical dimensions and properties of an isotropic P-Strut. These reference constants are used in the active analysis of Section 3.6 and again in the optimization study of Chapter 4. The percent variations in the DC stiffness, the stiffness at infinity, the peak loss factor and frequency, and the bandwidth were calculated. The reference parameters were varied independently by ±25%. The percent difference is defined by:

$$Percent\ Difference = 100\% \left[\frac{(Value - Reference\ Value)}{Reference\ Value} \right] \quad (3.92)$$

Since an increase in η^* and bandwidth is beneficial to the damping performance, the parameteric study suggests increasing the pressure stiffness, K_P. This equates to increasing the amount of force (or strain energy) which is transmitted into the fluid and thus into the dashpot. K_P can be increased by increasing K_R which suggests—as did the static analysis—increasing the effective hoop stiffness, $E_{22}{}^L$ (equation 3.80).

TABLE 3.2: A Parameteric Study of the Passive Performance Model

REFERENCE VALUES*

K_S (K lbf/in)	K_P (K lbf/in)	K_b (lbf/in)	K_L (K lbf/in)	K_R (K lbf/in)	K_f (K lbf/in)
47.1	8.4	10.0	117.8	13.9	26.2

C (lbf s / in)	Ψ_b (K in²/in²)	Ψ_o (K in²/in²)
0.044	31.42	204.08

K_{DCp} (K lbf/in)	$K_{\infty p}$ (K lbf/in)	η^*	ω^* (Hz)	B_w (Hz)
47.8	48.5	6.75×10^{-2}	1.59	2.16×10^{-2}

PERCENT VARIATION

PARAMETER		K_{DCp}	$K_{\infty p}$	η^*	ω^*	B_w
K_L	+25%	−0.5	−1.0	−35.1	0.4	−34.8
K_L	−25%	1.2	2.2	74.3	−0.6	73.0
K_S	+25%	25.5	25.9	25.7	0.2	25.9
K_S	−25%	−25.3	−25.5	−25.4	−0.2	−25.5
K_P	+25%	0.2	0.7	40.8	11.8	57.4
K_P	−25%	−0.2	−0.7	−36.7	−11.7	−44.2
k_b	+25%	0.2	0.0	−11.8	13.4	0.0
k_b	−25%	−0.2	0.0	15.4	−13.4	0.0
c	+25%	0.0	0.0	0.0	−20.0	−20.0
c	−25%	0.0	0.0	0.0	33.3	33.3

*The Reference Values are based on an Isotropic, Circular Cylindrical P-Strut with
the following properties:

E =9 Msi (62 GPa), B_f=200 Ksi, t =10 mils (0.25 mm), R_c=0.5 in (1.27 cm),

L =6in (15.2 cm), v =0.3, υ =0.0014 lbf s/in² (9.6 K cp), and L_o=1.25 in (31.8 cm)

Increasing the Bulk Modulus of the fluid, B_f, increases K_f, and stiffens K_p (equation 3.81).

In addition, the parameteric study indicates that decreasing the pressure-elongation stiffness, K_L, would increase the peak loss factor. Physically, this implies an increase in the proportion of the fluid volume change due to axial deformation as opposed to swelling or compressing. However, the model study also suggests increasing the structural stiffness of the cylinder, K_S. K_S and K_L are related by equations 3.79 and 3.82, $K_S = (1-2\nu_{12}{}^L)K_L$. Increasing K_S while decreasing K_L can be achieved by decreasing the Poisson's Ratio $\nu_{12}{}^L$. Reducing $\nu_{12}{}^L$ was beneficial to the static performance as well.

Finally, the parameteric study shows that increasing the peak frequency, ω^*, is inversely proportional to the dashpot coefficient such that increasing c (i.e. a more viscous fluid or smaller orifice dimensions) moves the Bode curves towards DC without effecting the maximum loss factor.

3.5.5   COMPARISON WITH THE D-STRUT

The passive dampers which were mentioned in Chapter 2 have frequency characteristics and equations similar to those developed above. Most notably, the Honeywell D-Strut, as a viscous damper, can be represented by a stiffness model analogous to Figure 3.12. A schematic of the D-Strut is depicted in Figure 3.14. Anderson, et. al. published a thorough explanation and analysis of the D-Strut in reference 2.

Although both the P-Strut and the D-Strut can be identically modeled, the physical interpretations of the stiffness parameters and the geometry of the devices differ significantly. The D-Strut contains an outer and an inner solid tube. For the P-Strut the outer tube is the cylinder wall, while the

inner tube is the fluid-pressure stiffness, K_p. A second and perhaps more significant difference is the orientation of the load path parallel to the cylinder wall. The orifice and the flexible fluid reservoir are arranged inside the outer tube of the D-Strut in line with a diaphragm and the inner tube. Since for the D-Strut both the metal diaphragm and fluid deform together, the overall stiffness of this load connection is difficult to formulate [35]. As a solution, Anderson calculated all of the modeled stiffnesses by fitting experimental data [2]. In contrast, the simplified geometry of the P-Strut permits the direct derivation of the physical stiffness parameters and their coupling to the modeled parameters as accomplished in the Section 3.5.2.
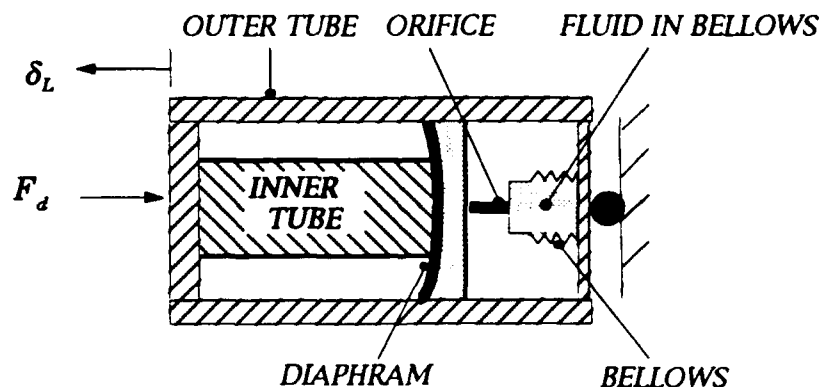
FIGURE 3.14: A Schematic of the D-Strut

3.5.6 COMPARISON WITH PIEZOELECTRIC RESISTIVE-SHUNTED STRUTS

A piezoelectric resistive-shunted device exhibits passive damping qualities analogous to the P-Strut and the D-Strut. The piezo generates a voltage in response to a structurally induced strain. The voltage is then dissipated through a resistive circuit [20].

Piezo dampers can be modeled with the spring-dashpot system of Figure 3.12. The parameters of these models are complex functions of the mechanical and piezoelectric properties of the component materials and the passive circuitry, in contrast to the physical stiffnesses of the P-Strut. The damping loss factor, η, is dependent upon the ratio of the open-circuit to closed-circuit stiffnesses for the piezoelectric material [20] whereas in the viscous dampers η is related to the ratio of K_{DCp} to $K_{\infty p}$. The peak frequency is set by the selected shunting resistor [20]. For viscous dampers, the orifice dimensions and fluid properties fix the ω^*.

Aldrich, et. al. has recently completed work on a piezoelectric passive damper which utilizes a mechanical lever to enhance the damping performance [1]. The lever mechanism could be modified to work as an actuator. The concept is analogous to the P-Strut fluid lever.

3.5.7   REVISED PASSIVE MODEL

In order to seal the P-Strut vessel, endcaps were epoxied to the vessel. The epoxy layer demonstrated, during testing, viscous damping at low frequencies. The discrete stiffness model was revised to include the epoxy dynamics.

The updated model adds three parameters, K_{DCep}, K_{ep}, and C_{ep}. The meanings are analogous to the springs previously defined: K_{DCep} equals the DC stiffness of the epoxy, C_{ep} is the modeled epoxy mechanical dashpot coefficient, and K_{ep} represents the stiffness in series with the epoxy dashpot.

Figure 3.15 depicts the revised discrete stiffness model. The three parameter epoxy model is placed in series with the static stiffness of the cylinder, K_l. Again assuming a sinusoidal displacement, the revised

damping model has performance characteristics similar to the original model with the addition of a second pole and zero set.

Figure 3.16 depicts the magnitude and phase responses of the revised passive damping transfer function, $K_{pass}{}'$ (dashed lines) and the original model, K_{pass} (solid lines). The three epoxy parameters, K_{DCep}, K_{ep}, and C_{ep}, used to calculate $K_{pass}{}'$ are representative of the measured values reported in Chapter 6. The two pole-zero pairs of the revised model (one pair per dashpot) have two frequency regions where stiffening and phase change occurs. However, the location of the first zero and pole, which is inversely dependent on the epoxy dashpot coefficient, C_{ep}, is at approximately the same location as that of the second pole-zero pair which is due to the orifice damping, c. Because of the proximity of the poles and zeroes and because the stiffness change associated with the epoxy is much greater than that associated with the orifice, the analytical epoxy damping overwhelms the orifice damping. In short, the orifice damping is unobserved.

Nevertheless, including the epoxy parameters with the original three modeled stiffnesses and dashpot does not negate the trends established in the parameteric study of Section 3.5.4. Rather, a change in C_{ep}, K_{DCep}, and K_{ep} have the same effect on the first zero-pole pair as changing C_1, K_1 and K_2 in the original model. The first pole-zero pair is controlled by the epoxy parameters and the second by the cylinder and orifice parameters.
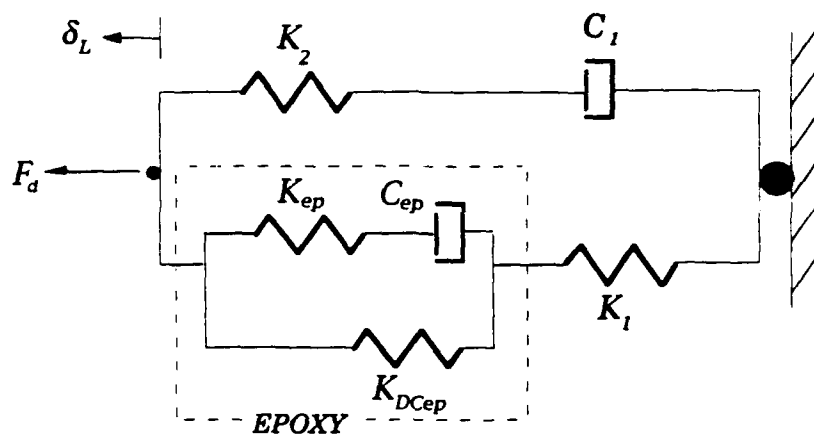
FIGURE 3.15: Revised Passive Discrete Stiffness Model

REVISED PASSIVE PERFORMANCE
Magnitude and Phase vs Frequency
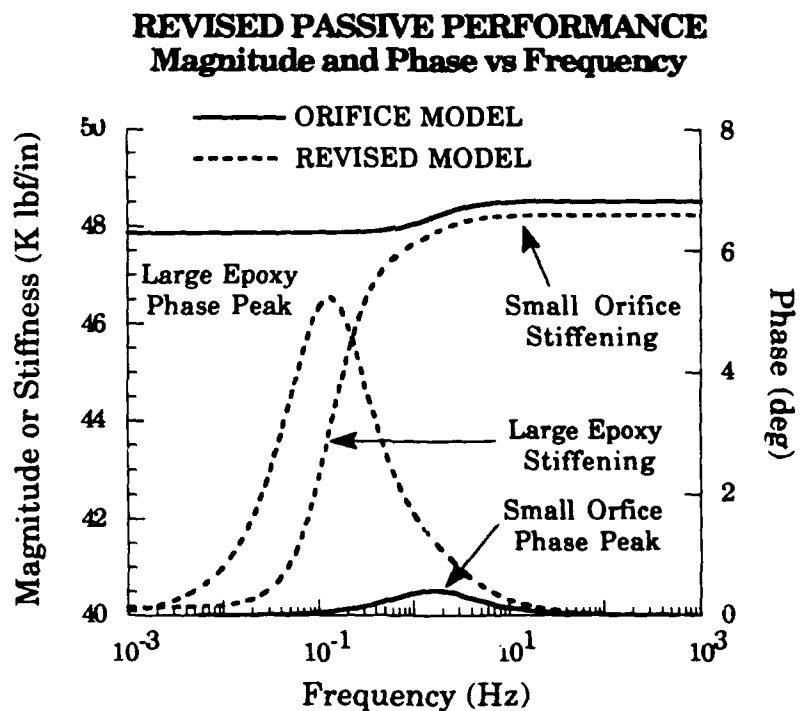
FIGURE 3.16: Revised Passive Performance Bode Plots

81

3.6   DERIVATION OF ACTIVE PERFORMANCE EQUATIONS

The P-Strut is a dynamic fluid elastic actuator. The active mode of operation relates a dynamic input force F_b or input stroke δ_b to a resulting actuation displacement δ_L assuming no disturbance force ($F_d=0$).

3.6.1   MECHANICAL ANALYSIS OF THE ACTIVE PERFORMANCE

Figure 3.17 depicts the P-Strut in its active mode of operation. The dynamic input force, F_b, equals the pressure response in the bellows, P_b, and the spring force of the bellows:

$$F_b = P_b A_b + K_b \delta_b \tag{3.93}$$

The pressure inside the bellows and the pressure loss through the orifice, ΔP, are in equilibrium with the pressure inside the cylinder, P:

$$P_b = P + \Delta P \tag{3.94}$$

where ΔP was defined in equation 3.56.

The velocity in the orifice, V_o, is designated as the speed of the fluid leaving the orifice such that a positive pressure in the bellows, P_b, forces the fluid into the cylinder. This velocity had the opposite sign of the velocity used in the passive modeling (equation 3.74). Therefore, the Laplace definition of V_o as a function of the bellows stroke is $V_o = \Psi_{ob} s \delta_b$. Substituting 3.56 (using this definition of V_o) and 3.93 into 3.94, multiplying by the area of the cylinder, A_c, and solving for P yields:

$$P = \frac{\Psi_b F_b - \delta_b \left[\Psi_o \Psi_{ob} C s + \Psi_b K_b \right]}{A_c} \tag{3.95}$$

The pressure, P, causes an elongation, δ_L, which was defined in equation 3.51.

82
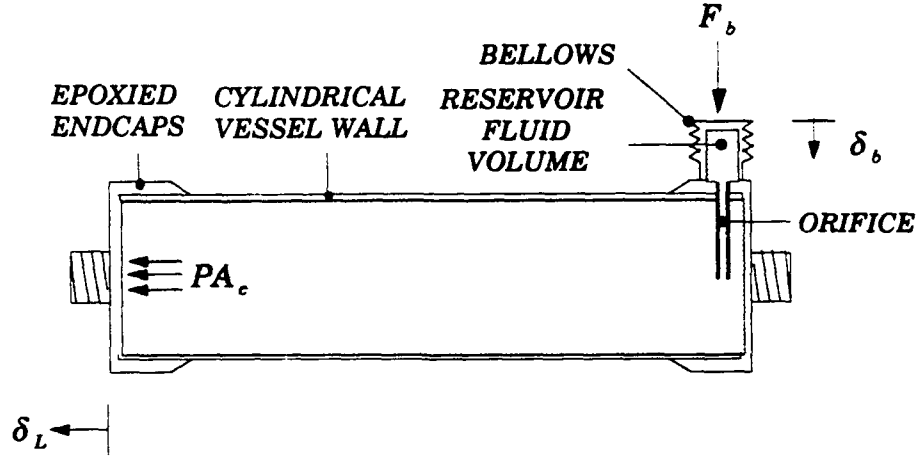
FIGURE 3.17: P-Strut Schematic in Active Mode of Operation

The bellows stroke, δ_b, as a function of pressure was reported previously as equation 3.53. Inserting 3.53 into 3.95 and solving for the pressure as a function of the input force, F_b, yields:

$$P = \frac{\Psi_b F_b}{\left\{ A_c + \left[\Psi_o^2 Cs + \Psi_b^2 K_b \right] \left\{ \dfrac{R_c}{2t} \left[\dfrac{L_{eff}}{E_{11}^L}(1 - 2v_{12}^L) + \dfrac{2L}{E_{22}^L}(2 - v_{21}^L) \right] + \dfrac{L}{B_f} \right\} \right\}} \qquad (3.96)$$

The elongation. δ_L, as a function of the input force, F_b, is determined by substituting 3.96 into equation 3.51 and simplifying. The resulting equation gives the compliance or admittance of the actuator.

$$\delta_L = F_b \left\{ \frac{\Psi_b L_{eff} \dfrac{R_c(1 - 2v_{12}^L)}{2t E_{11}^L A_c}}{1 + \left[\Psi_o^2 Cs + \Psi_b^2 K_b \right] \left\{ \dfrac{R_c}{2t} \left[\dfrac{L_{eff}}{E_{11}^L A_c}(1 - 2v_{12}^L) + \dfrac{2L}{E_{22}^L A_c}(2 - v_{21}^L) \right] + \dfrac{L}{B_f A_c} \right\}} \right\} (3.97)$$

The admittance transfer function (δ_L / F_b) can be written with the physical stiffnesses defined in equations 3.79 through 3.82 as:

$$\frac{\delta_L}{F_b} = A_{act}(s) = \left\{ \frac{\dfrac{\Psi_b}{K_L^e}}{1 + [cs + k_b] \left\{ \dfrac{1}{K_L^e} + \dfrac{1}{K_R} + \dfrac{1}{K_f} \right\}} \right\} \tag{3.98}$$

where:
$$K_L^e = \frac{E_{11}^L A_{ac}}{L_{eff}} = K_L \frac{L}{L_{eff}} \tag{3.99}$$

$c = \Psi_o^2 C$ and $k_b = \Psi_b^2 K_b$.

The effective length, L_{eff}, (see Section 3.3.3) is reintroduced to the axial elongation stiffness since the only axial loading is due to the pressure force inside the cylinder. In contrast to the passive analysis, using the effective length for the axial elongation stiffness and the physical length, L, for the remaining stiffnesses does not complicate the analysis. The terms in equation 3.98 are otherwise the same as those found in the passive analysis, equation 3.78.

The active model evaluated at DC must match the static equations derived in Section 3.3. Setting $s=0$ in equation 3.98 (which is equivalent to ignoring the dashpot loss factor) and rearranging yields:

$$\frac{\delta_L}{F_b}\bigg|_{\substack{ACTIVE \\ DC}} = A_{act}(0) = \left\{ \frac{1}{\dfrac{K_L^e}{\Psi_b} + \Psi_b K_b K_L^e \left[\dfrac{1}{K_L^e} + \dfrac{1}{K_R} + \dfrac{1}{K_f} \right]} \right\} \tag{3.100}$$

Note the strain ratio Γ_c (equation 3.30), can be written as the ratio of the radial dilation stiffness (equation 3.79) to the axial or elongation stiffness (equation 3.80):

$$\Gamma_c = \frac{\varepsilon_{11}}{\varepsilon_{22}} = \frac{K_R}{2K_L} \tag{3.101}$$

84

The static admittance was reported as the inverse of equation 3.55. Substituting the definitions of the physical stiffness (equations 3.79 through 3.82 and 3.99), equation 3.101 into 3.55, and inverting yields for the DC static admittance:

$$
\left. \frac{\delta_L}{F_b} \right|_{STATIC} = \left\{ \frac{1}{\dfrac{K_L^e}{\Psi_b} + \Psi_b K_b \left[1 + \dfrac{K_L^e}{K_R} + \dfrac{K_L^e}{K_f} \right]} \right\}
\qquad (3.102)
$$

Rearranging the denominator in equation 3.102 yields the same equation as the DC admittance of the active analysis.

3.6.2 ACTIVE FREQUENCY CHARACTERISTICS

As illustrated in Figure 3.17, the input force, F_b, is non-collocated with the actuation displacement, δ_L. Due to the absence of the competing stiffnesses which complicated the modeling of the passive stiffness transfer function (equation 3.84), the active admittance transfer function δ_L versus F_b can be pictured with a simple five parameter discrete stiffness model. Figure 3.18 depicts the active spring-dashpot model.

The model parameters are the physical stiffnesses and dashpot, namely K_L, K_R, K_f, K_b and C. To rederive the admittance, A_{act}, from the model, the input force, F_b is related to the input stroke, δ_b, including the proper area ratios for the dashpot, (i.e. $\Psi_o \Psi_{ob}$. from equation 3.95). δ_b is written as a function of δ_L using the series stiffnesses and the ratio of the bellows area to the vessel area, Ψ_b.

The model depicts three parallel load paths. The first is the bellows static stiffness, K_b. The mechanical dashpot represents the second and the

frequency dependent or damping load path. The remaining load path represents the fluid-vessel-pressure stiffness and is formed from K_L, K_R, and K_f.

Reducing the model or simplify equation 3.98 yields the following frequency dependent admittance:

$$\frac{\delta_L}{F_b} = A_{act}(s) = \frac{\Psi_b K_R K_f}{(k_b + cs)(K_L K_R + K_L K_f + K_R K_f) + K_L K_R K_f} \qquad (3.103)$$

A_{act} represents the amount of actuation displacement (i.e. elongation) achieved per input force. The units of A_{act} is length per force or the inverse of the complex actuation stiffness.

The root of the denominator of equation 3.102 represents the pole, ω_c, of the active performance.

$$\omega_c = \frac{k_b(K_L K_R + K_L K_f + K_R K_f) + K_L K_R K_f}{c(K_L K_R + K_L K_f + K_R K_f)} \qquad (3.104)$$

If the input force is assumed sinusoidal, ω_c is the corner frequency on a Bode Diagram. A sinusoidal input force causes a sinusoidal response at the same frequency but with a different magnitude and a shifted phase. The magnitude and phase of A_{act} versus frequency is depicted in the Bode plots of Figure 3.19. The DC admittance and the roll-off associated with the pole are apparent.

Physically the actuation force commands a "static" displacement at low frequencies with magnitude, A_{DCact}. As the frequency increases the fluid traveling from the bellows through the orifice is impeded by the viscous shearing action. The phase of the actuation displacement begins to lag the input force as the dashpot starts to "lock-up". At high frequencies

the dashpot is effectively rigid with an infinite stiffness, $cs = \infty$. Thus, as the frequency increases the actuation displacement rolls-off to zero.

The bandwidth is defined by the frequency where the admittance equals $0.707A_{DCact}$ (i.e. a –3 dB reduction in the DC magnitude). For single pole systems, the corner frequency equals the bandwidth [37]. As stated in Chapter 2, to actively damp a mode or to alter the performance of a structure at a particular frequency, the P-Strut must be capable of commanding a displacement or force at that frequency. Therefore, the bandwidth limits the effective frequency range of the fluid elastic actuator.

In the time domain the bandwidth dictates the speed of the response. A high bandwidth ($\omega_c >> 0$) indicates a quick response to an input force. If a step input force is initiated and held, the actuation displacement will respond by elongating the amount predicted in the static analysis. In the complex frequency or Laplace domain, equation 3.103 subjected to a step input can be written as:

$$\delta_L(s) = \frac{N}{D_1 + D_2 s} F_b(s) \bigg|_{\text{unit step}} = \frac{N}{D_1 + D_2 s}\left(\frac{1}{s}\right) \tag{3.105}$$

where N, D_1, and D_2 are apparent from the numerator and denominator of 3.103. The time to rise to within 5% of the steady state or static value, t_r, can be determined with an Inverse Laplace Transform. The Inverse Laplace Transform of 3.105 equals:

$$\delta_L(t) = \frac{N}{D_1}(1 - e^{-D_1/D_2 t}) = A_{DCact}(1 - e^{-\omega_c t}) \tag{3.106}$$
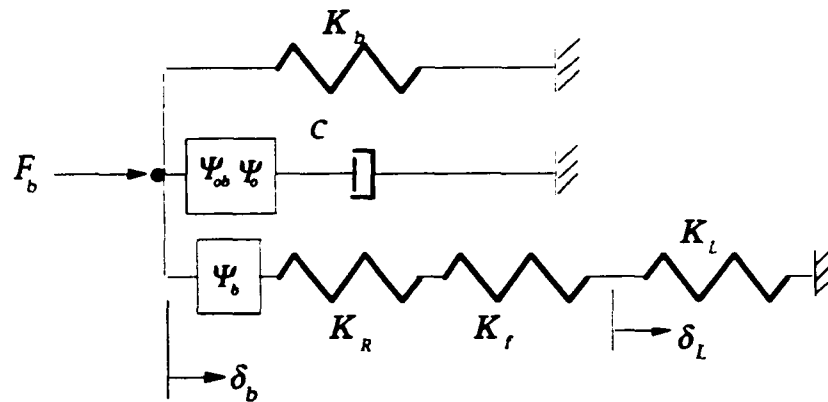
FIGURE 3.18: Discrete Active Performance (Admittance) Model
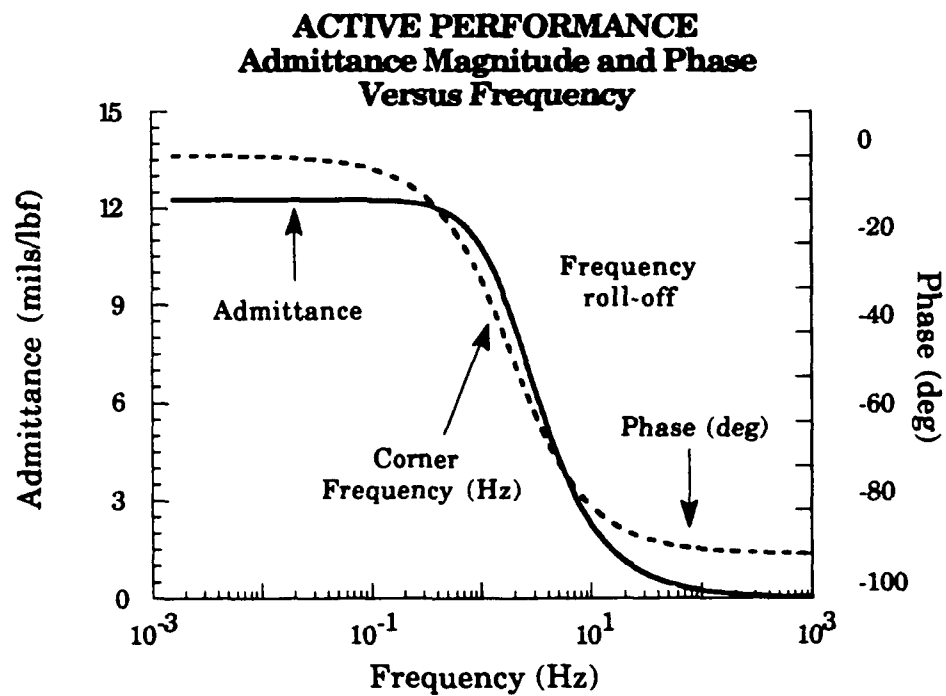
FIGURE 3.19: Active Performance Admittance (A_{act}) Bode Diagrams: Magnitude and Phase Versus Frequency

At $t=0$, the force is initiated and the response is zero. As time increases, the static elongation A_{DCact} is approached. By definition of t_r:

$$0.95 = (1 - e^{-\omega_c t}) \quad \text{or} \quad t_r \approx \frac{3}{\omega_c} \tag{3.107}$$

Therefore, increasing the bandwidth or increasing the corner frequency decreases the time to rise, t_r.

Nevertheless, increasing the bandwidth is not necessarily ideal. The benefit of the P-Strut's inherent roll-off is that the actuator cannot feedback noise or add energy to higher (and possibly unmodeled) structural modes. This prevents the controller from commanding inputs through the P-Strut which could destabilize the higher dynamics of the structure.

3.6.3 PARAMETERIC STUDY OF THE ACTIVE PERFORMANCE

The findings of a parameteric study on the active performance model are reported in Table 3.3. For the active model, the four springs, K_L, K_R, K_f, and K_b, and the dashpot coefficient, c, were varied by ±25% and the resulting impact on the DC admittance and the corner frequency, ω_c, or bandwidth, B_w, is listed. The percent difference was defined in equation 3.90. The reference values were calculated from the same physical dimensions and properties used in the passive parameteric study.

Table 3.3 indicates that decreasing the longitudinal stiffness, K_L, and increasing the radial dilation stiffness, K_R, and the fluid stiffness, K_f, increases the DC admittance while only minimally effecting the pole and zero. In the passive parameteric study of Section 3.43, stiffening K_R and K_f also increased the passive performance.

TABLE 3.3: A Parameteric Study of the Active Performance Model

REFERENCE VALUES

K_L (K lbf/in)	K_R (K lbf/in)	K_b (lbf/in)	K_f (K lbf/in)	C (lbf s / in)
117.8	13.8	10.0	26.2	0.044

Ψ_b' (K in²/in²)	Ψ_o' (K in²/in²)	A_{DCact} (in/lbf)	ω_c or BW_{act} (Hz)
31.42	204.1	1.23×10^{-4}	1.59

PERCENT VARIATION

PARAMETER		A_{DCact}	ω_c or B_{uact}
K_L	+25%	−19.4	0.7
K_L	−25%	31.6	−1.1
K_R	+25%	7.0	6.4
K_R	−25%	−9.8	−7.7
K_f	+25%	3.6	3.2
K_f	−25%	−5.5	−4.5
k_b	+25%	−11.9	13.5
k_b	−25%	15.6	−13.5
c	+25%	0.0	−20.0
c	−25%	0.0	33.3

The bellows stiffness, K_b, represents a direct path from the input force, F_b, to ground, therefore decreasing k_b intuitively increases A_{DCact}. In addition, k_b strongly influences the bandwidth.

The orifice dashpot coefficient, c, influenced the location of the pole, ω_c, such that increasing c moves the pole towards DC thereby reducing the bandwidth of the actuator. The same observation was true for the passive performance.

3.7   CLOSING COMMENTS ON THE PERFORMANCE EQUATIONS

The model developed in Section 3.6 correlated well with the measured data. Therefore, the additional epoxy damping, which was discovered during testing and discussed in Section 3.5.7, was not modeled in the active analysis.

The three separate models can be combined. The resulting model would include the elongation of the actuator, δ_L, and the bellows stroke, δ_b, as a dynamic function of the input force, F_b, and the disturbance force, F_d. The analysis and experimental work presented in this thesis does not require the combination model. Nevertheless, the author is planning to present the combined model in a future publication as part of a control experiment involving the P-Strut.

CHAPTER 4:

Optimizing the P-Strut Design

4.1   CHAPTER OUTLINE

In Chapter 4 the fluid elastic actuator's dimensions and physical properties are optimized with respect to the static, passive, and active performances. Three P-Strut designs are considered: an isotropic aluminum, a hybrid aluminum-composite, and a balanced composite. The hardware selected and the final actuator configurations are detailed.

4.2   OPTIMIZING THE PHYSICAL DIMENSIONS

The P-Strut is primarily constructed from a circular cylinder. For a cylinder, the three physical dimensions to optimize are the radius, R_c, the length, L, and the thickness, t. Section 3.3.5 reported the isotropic, static equations for a circular cylindrical P-Strut. Considering an isotropic actuator, Figures 4.1 and 4.2 depict the trends for R_c and L versus the input force required to achieve a specified

**INPUT FORCE VERSUS CYLINDER RADIUS
(Isotropic P-Strut Static Performance)**

*Force Required to Achieve
0.33 mil Actuation Elongation*

—o— w t=0.005in
—△— w/ t=0.010in
—□— w/ t=0.015in
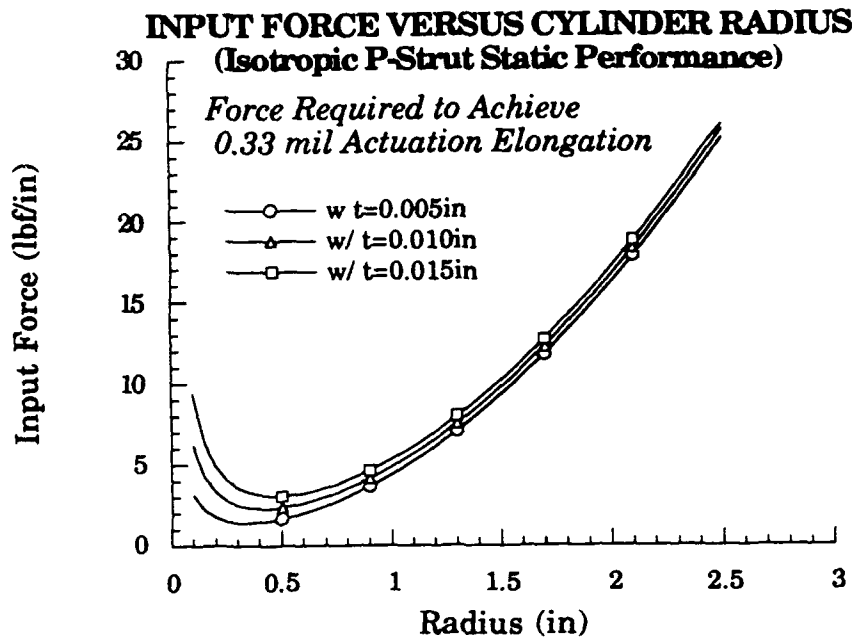
FIGURE 4.1: P-Strut Vessel Radius Versus Input Force

**INPUT FORCE VERSUS CYLINDER LENGTH
(Isotropic P-Strut Static Performance)**

*Force Required to Achieve
0.33 mil Actuation Elongation*

—o— w/ t=0.005in
—△— w/ t=0.010in
—□— w/ t=0.015in
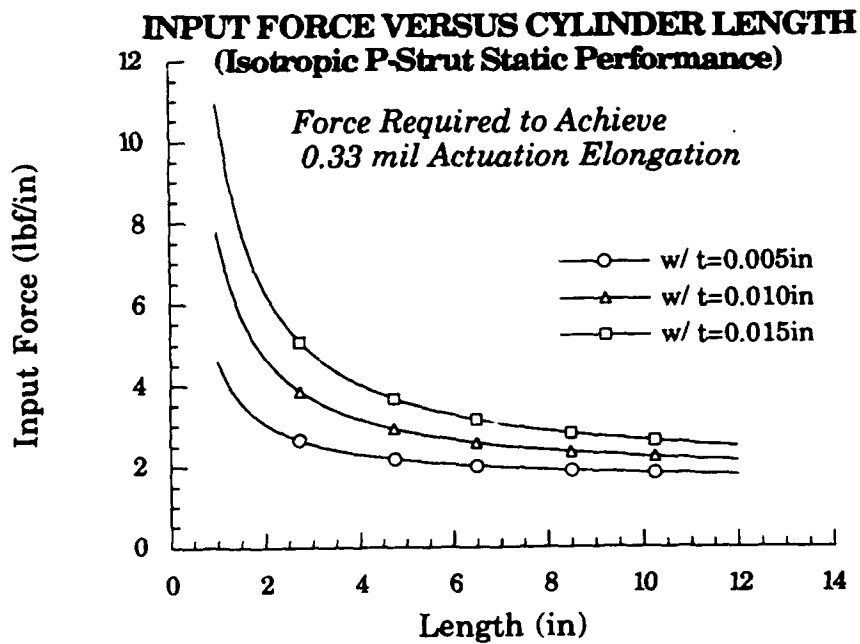
FIGURE 4.2: P-Strut Vessel Length Versus Input Force

93

elongation of 0.33 mil. These curves were calculated with the reference constants listed in Table 4.1 while varying only the parameter of interest and the cylinder thickness. Figure 4.1 indicates that a radius of approximately 0.5 in (1.27 cm) is optimal. The input force versus elongation cost, F_b / δ_L, as represented in Figure 4.2, levels off as the length of the P-Strut increases.

Additional constraints on L and t include the required static stiffness (approximately K_S from equation 3.87) and the physical limits of the optical interferometer testbed, on which the P-Strut actuator is to be applied [5,36]. The length of the longerons on the interferometer are approximately 7 in (17.8 cm). Existing component hardware (i.e. passive dampers and actuators) have DC stiffnesses ranging from 22.9K lbf/in (4 N/μm) [3] to approximately 85K lbf/in (15 N/μm) [5]. Combining these considerations with the definition of K_S (equation 3.82), the proposed P-Strut designs have an L of no more than 7 in and a t of 4 to 15 mil (0.10-0.38 mm).

4.3 OPTIMIZING THE MATERIAL PROPERTIES WITH COMPOSITES

Tailoring the material properties has the potential to enhance the static performance by increasing the hoop stiffness and therefore decreasing the radial dilation as shown in Section 3.3.6. Similarly, the passive and active performances may be improved by decreasing $v_{12}{}^L$.

Table 4.1 lists the results of adding successive graphite-epoxy AS4/3501-6 plies to an aluminum cylinder. The wraps have the graphite fibers running in the radial direction (i.e. $\varphi = 90°$). The table lists the calculated laminate properties, the axial stiffness of the cylinder, the

TABLE 4.1: A Comparison of the Number of Composite Wraps
Versus the Static Performance of a Hybrid
Aluminum-Composite

REFERENCE CONSTANTS

E_{11} = 20.6 Msi (142 GPa) E_{22} = 1.42 Msi (9.82 GPa)

G_{12} = 0.87 Msi (6 GPa) v_{comp} = 0.3

t_{comp} = 5.28 mil (0.134 mm)/ply t_{al} = 8 mil (0.203 mm)

E_{al} = 9 Msi (62 GPa) v_{al} = 0.3

L = 6.0 in (15.24 cm) R_c=0.60 in (1.52 cm)

K_b = 10 lbf/in (1.75 KN/m) B_f = 588 Ksi (4.1 GPa)

A_b = 0.025 in^2 (16.1 mm^2)

RESULTS

Parameters	Number of 90° Wraps					
	None	1	2	3	4	
E_{11}^{L}	9.00	6.25	4.94	4.18	3.69	Msi
E_{22}^{L}	9.00	13.61	15.60	16.70	17.41	Msi
v_{12}^{L}	0.30	0.14	0.10	0.08	0.06	
K_S	45.5	52.8	58.4	63.8	69.0	K lbf/in
Γ_c	0.24	0.97	1.51	2.00	2.42	
F_b / δ_L	7240	3297	2885	2794	2800	lbf/in
δ_b / δ_L	476	172	134	120	113	in/in

strain ratio, Γ_c, and the actuation costs, F_b / δ_L and δ_b / δ_L. The fibers increase E_{22}^{L} and reduce v_{12}^{L}. Due to the increasing thickness of the cylinder wall, K_S is increased. After just one ply, the strain ratio, Γ_c, is considerably increased and the performance costs are drastically decreased. Subsequent wraps improve the performance at a significantly decreasing rate of return due to the additional thickness. After the third ply, the actuation cost, F_b / δ_L, increases as a result of the increasing thickness. The "optimal" hybrid P-Strut selected was an aluminum cylinder with a single 90° composite wrap.

Table 4.2 considers the performance of several all-composite P-Struts. To avoid normal stress-shear coupling only balanced laminates were examined. To maintain a reasonable thickness, the number of plies was limited to four—therefore, layup symmetry was not possible with most combinations. The results indicate that having all fibers run in the hoop direction have the least actuation costs, F_b / δ_L and δ_b / δ_L. However, if all the fibers run in the hoop direction, the static stiffness is below the desired range. The [90/∓60/90] layup offers a compromise with an acceptable vessel axial stiffness, K_S, as well as low F_b / δ_L and δ_b / δ_L cost ratios.

An interesting phenomenon is observed when attempting to maximize the strain ratio Γ_c (equation 3.30). This parameter includes both stiffnesses and a factor of laminate Poisson's Ratios. As shown in Figure 4.2, the optimal layup with respect to Γ_c has fibers slightly offset from the hoop direction. This is due to a complex Poisson's effect called "scissoring".

TABLE 4.2: A Comparison of P-Strut Composite Layups
Versus the Static Performance

RESULTS

Parameters	Balanced Composite Layups					
	[90/0/90]	[90₄]	[90/∓75/90]	[90/∓60/90]	[90/∓45/90]	
$E_{11}{}^L$	7.85	1.42	1.47	1.91	3.51	Msi
$E_{22}{}^L$	14.27	20.60	18.88	14.61	11.92	Msi
$v_{12}{}^L$	0.03	0.02	0.05	0.13	0.19	
K_S	79.1	19.2	19.9	25.8	47.4	K lbf/in
Γ_c	0.88	8.15	8.53	5.53	1.55	
F_b / δ_L	3630	1070	1118	1487	2997	lbf/in
δ_b / δ_L	182	64.2	64.6	75.2	134	in/in

STATIC PERFORMANCE COMPARISON
Gr/Ep Composite Layup

Peak at [90/-75/+75/90] ——————➤

Γ_c (Long Strain/Hoop Strain)

Composite Layups   [90/$-\varphi$/$+\varphi$/90]
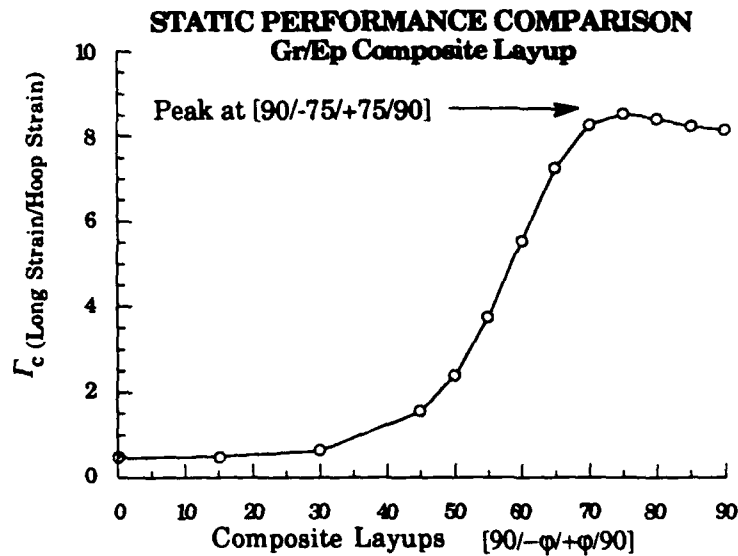
FIGURE 4.3: Poisson's "Scissoring" Effect:
Γ_c Versus Composite Four Ply Layups

4.4   VISCOUS FLUID AND ORIFICE

The passive and active analyses indicated the frequency dependence of the P-Strut's performance on the fluid and the orifice. The ideal fluid would have an infinite bulk modulus (i.e. incompressible) with a high viscosity. The DOW Corning 200 Series silicon fluids have a high B_f and a viscosity which can be tailored to a desired specification [15]. A less expensive alternative is glycerol which has a higher B_f and a viscosity in the range of the selected silicon fluids. Table 4.3 lists the properties of the two silicon fluids and the glycerol fluid which was utilized in the P-Strut tests. These parameters span the range of practical viscous fluid properties and include the range where most viscous oils are present. The thermal expansion and variation of the fluid properties with temperature were not

modeled, although the silicon and glycerol fluids exhibit decreasing viscosity with temperature [6,15,31].

The orifices used in the P-Strut design ranged in diameter from 30 to 84 mil (0.76-2.13 mm) and in length from 0.8 to 1.5 in (1.93-3.81 cm). An additional fixed fluid passageway, inside the bellows-orifice connector, has an approximate diameter of 0.16 mil (0.41 cm) and length of 0.3 in (0.76 cm). This connector orifice was included in the calculation of the orifice dashpot coefficient, C.

TABLE 4.3: Properties of the P-Strut's Viscous Fluids

Parameters	10K cs Silicon*	30K cs Silicon*	Glycerol**	Units
Bulk Modulus, B_f	2.14×10^5	2.14×10^5	5.88×10^5	psi/ΔVol/Vol
Absolute Viscosity, μ	1.41×10^{-3}	4.22×10^{-3}	1.67×10^{-3}	lbf s/in @ R.T.
Density, ρ	0.0352	0.0352	0.0452	lbm/in^3

* Reference 15.   ** Reference 31.

4.5   HARDWARE SELECTION

The flexible reservoir contains the fluid which flows through the orifice during actuation. The flexible fluid reservoir selected was a metal bellows. The bellows offered the advantages over a piston-type mechanism of being simple, "leak-proof", and essentially frictionless. However, with the bellows difficulties arise in calculating the effective cross-sectional area, A_b, since during actuation the metal convolutions of the bellows open and close. A Parker Metal Bellows was selected which had an inner

diameter of 0.125 in (3.2 mm), an outer diameter of 0.375 in (9.5 mm), and an expanded length of approximately 0.46 in (11.7 mm) [38].

In order to achieve the input force, F_b, over the stroke required, δ_b, a DC solenoid was chosen. The solenoid is an "off-the-shelf" force generator which is capable of commanding reasonable forces over large displacements. Other actuators such as piezoactuators had limited stroke capabilities and/or were not feasible due to size considerations. Unfortunately, resistive heating in the coiled wire limits the on-time as well as influences the size, mass, and force characteristic of the solenoid [19,42]. The time delay associated with the magnetic flux in the air-gap limits the frequency.

The solenoid selected was a G.W. Lisk DC push-armature conical pole face solenoid capable of a force of 4 lbf over 0.2 in stroke. (18 N over 0.5 cm) with a maximum on time of 4.5 minutes [19]. The time delay is approximately 5 ms, indicating the dynamic behavior of the solenoid is not important in the bandwidth of the P-Strut's active performance.

4.6   FINAL P-STRUT DESIGN

Figures 4.4 through 4.6 depict a three view drawing of the P-Strut. Figure 4.7 details the solenoid-bellows-orifice connections. The length, radius, and thickness of the three P-Strut designs are reported in Table 4.4.

SCALE: *0.6 in (figure) to 1 in (P-Strut)*
All Dimensions in Inches

AXIAL VIEW POINT
Figure 4.5

TOP VIEW POINT
Figure 4.6

Endcap

*Additional Length Required
For Instrumentation
(see Chapter 5)*

Adjustable Depending Instrumentation

*Solenoid Bolted
(12-32 Bolt)
to Endcap*

See Figure 4.7 for Detail
*and Dimensions of
Solenoid-Bellows-Orifice
Connections*

Solenoid

7.9

Bellows

Bleed / Fill Port
10-32 Threaded Screw

Epoxied
Endcaps

*(Threaded 3/8-24
Connector)*

0.30

Bellows-Orifice
Connector   Cylinder

1.75

Orifice

0.38

Fluid

R_c

t

0.15   0.6   0.4

0.35

0.20

0.15   0.10

0.25 0.20

L

FIGURE 4.4: P-Strut Side View

100

Far Endcap

SCALE: 0.6 in (figure) to 1 in (P-Strut)
All Dimensions in Inches

6.15

Solenoid

Solenoid-Bellows
Connector

Bellows

Bellows-Orifice
Connector
Orifice

Vessel
Threaded Connector

1.75

0.375

Bleed / Fill Ports

Near Endcap

Bleed / Fill Ports

t $2R_i$ 0.25
                   0.10

1.75
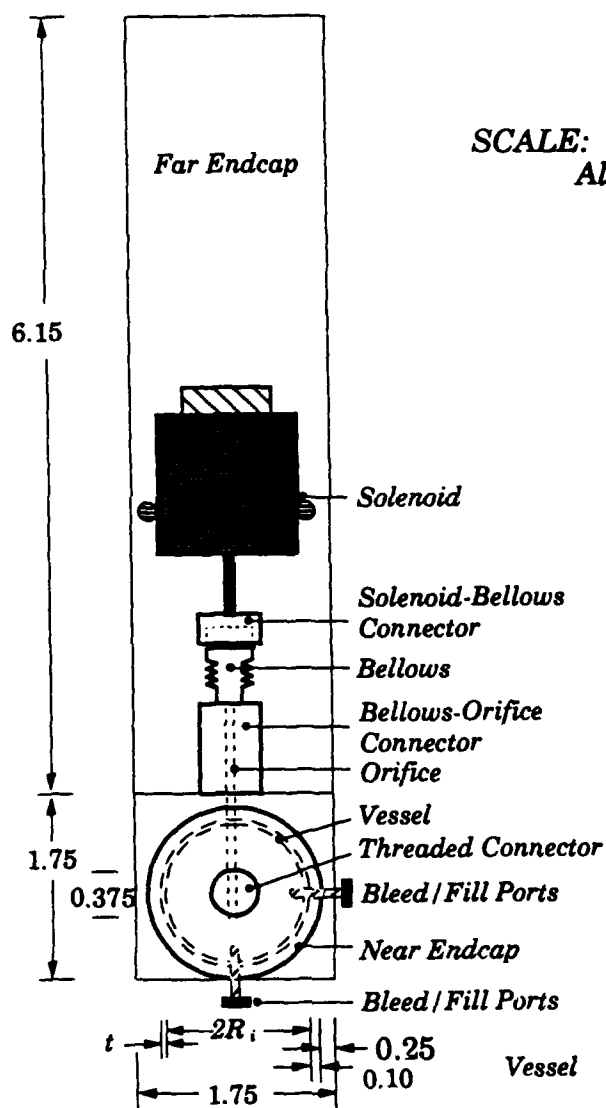
FIGURE 4.5: P-Strut Axial View

0.35
0.30
0.20
0.15

L

Vessel

Solenoid

Endcap

Solenoid
Bolted to
Endcap

Solenoid
Attachment

0.20

1.20

0.28
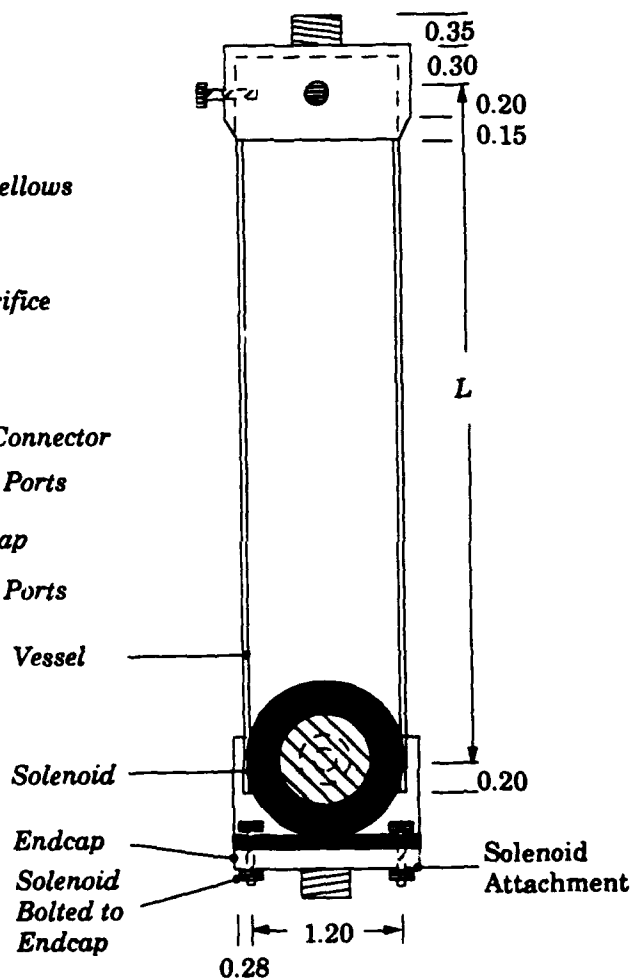
FIGURE 4.6: P-Strut Top View

101

FIGURE 4.7: Solenoid—Bellows—Orifice Connections

TABLE 4.4: The Dimensions of the Three P-Strut Designs

CIRCULAR CYLINDER DIMENSIONS

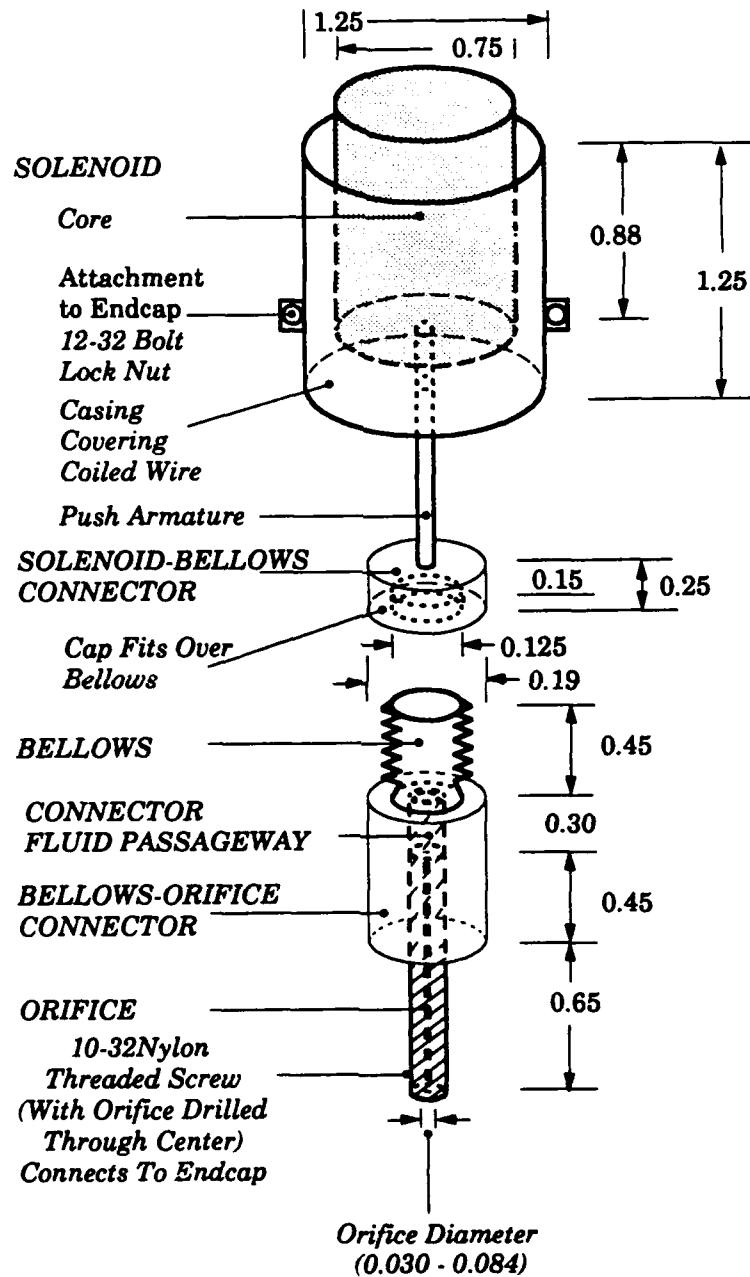| Parameters	Isotropic Aluminum	Hybrid Composite-Al	All-Composite [90/∓60/90]	Units
t_{al}	5.9	7.9	—	mil
t_{comp}	—	10.2	37.6	mil
L	6.90	6.65	5.50	in
R_i (Interior Radius)	0.60	0.60	0.60	in
R_c (Mean Radius)	0.61	0.61	0.62	in

4.7 "SUB-OPTIMAL" ASPECTS OF THE P-STRUT DESIGN

Certainly, the fluid elastic actuator described and pictured above is not optimal with respect to mass. The endcaps and the attachments are not optimized with regards to size or shape. The DC solenoid selected has a greater force/stroke characteristic and consequently, more coiled wire and metal core than required. In addition, moving the fluid into an annulus configuration (i.e. inserting a stiff foam or secondary composite cylinder), instead of the fully filled cylinder, would reduce the fluid mass while only nominally effecting the overall performance. This concept is depicted in Figure 4.8. Although a performance versus mass tradeoff for an annulus configured P-Strut could lead to a more "optimal" design, the basic equations and the optimization studies conducted in this chapter would remain relevant to the new design.
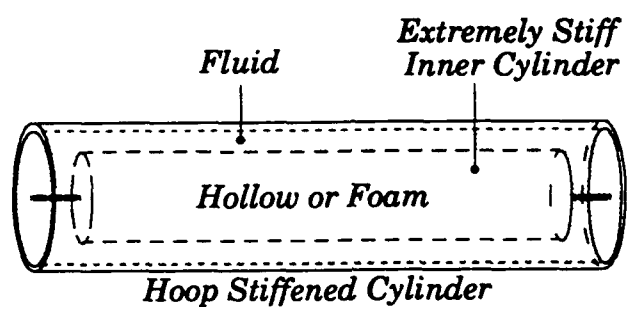
Fluid

Extremely Stiff
Inner Cylinder

Hollow or Foam

Hoop Stiffened Cylinder

FIGURE 4.8: An "Optimal" Vessel for the
P-Strut Design

CHAPTER 5:
Manufacturing and Experimental Procedures

5.1   CHAPTER OUTLINE

Chapter 5 describes the processes used to manufacture the isotropic, hybrid, and composite P-Strut pressure vessels. In addition, the experimen'al objectives, instrumentation, and procedures are discussed.

5.2   MANUFACTURING PROCESS

The key component of a P-Strut is the pressure vessel containing the viscous fluid.

5.2.1   CHEMICAL MILLING PROCESS FOR THIN ALUMINUM CYLINDERS

Available "off-the-shelf" 6061-T4 Aluminum tubing had an outer diameter of 1.25 in (3.18 cm) with a 20 mil (0.51 mm) wall thickness, t_{al}. In order to reduce t_{al}, a chemical milling process was utilized.

A simple alkaline reaction capable of etching aluminum was published by Cotton in reference 8 as:

$$2Al + 2NaOH + 2H_2O \rightarrow 2NaAlO_2 + 3H_2 \uparrow$$
$$2NaAlO_2 + 4H_2O \rightarrow 2NaOH + Al_2O_3 \bullet 3H_2O \downarrow$$

$$(5.1)$$
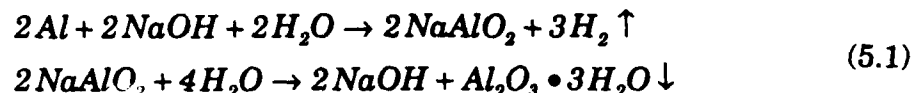
The base, sodiur hydroxide, dissolves the aluminum, releasing hydrogen gas, and producing an alumina precipitate. For safety, the reaction was performed inside of an air ducted hood. In addition, protective hand and eye wear was worn since sodium hydroxide is caustic.

Due to the exothermic nature of the reaction, the rate is highly dependent on the amount of milling material and solution. To determine the proper concentration (i.e. defined as mass of sodium hydroxide per mass of fluid) and the approximate time required to thin the cylinders a series of tests involving 3 in (7.6 cm) cylinder lengths was conducted. The results are graphed in Figure 5.1. The curves are exponentially fit to the data which are the expected reaction rate behaviors.

The actual P-Strut aluminum cylinders, which are approximately 6 in (15.2 cm) in length (see Table 4.4), were milled in the fluid baths at concentrations of approximately 15% sodium hydroxide. The milling time was approximately 30 minutes, which was less than anticipated based on the earlier tests. The cylinders were removed from the basic solution and measured with a caliper frequently. To insure uniform thinning the sodium hydroxide bath was kept agitated by hand.

The aluminum cylinder for the isotropic P-Strut was milled to an average thickness of 5.9 mil (0.15 mm) with a standard deviation of 0.4 mil (0.01 mm). The aluminum cylinder for the hybrid P-Strut was reduced to 7.9 mil (0.20 mm) with a deviation of 0.4 mil. The thickness was measured at the ends of the cylinders. Since attempting to measure the radius would

distort the thin tube, the inner and outer radii were estimated from their pre-etched values and the post-milled measured thickness.
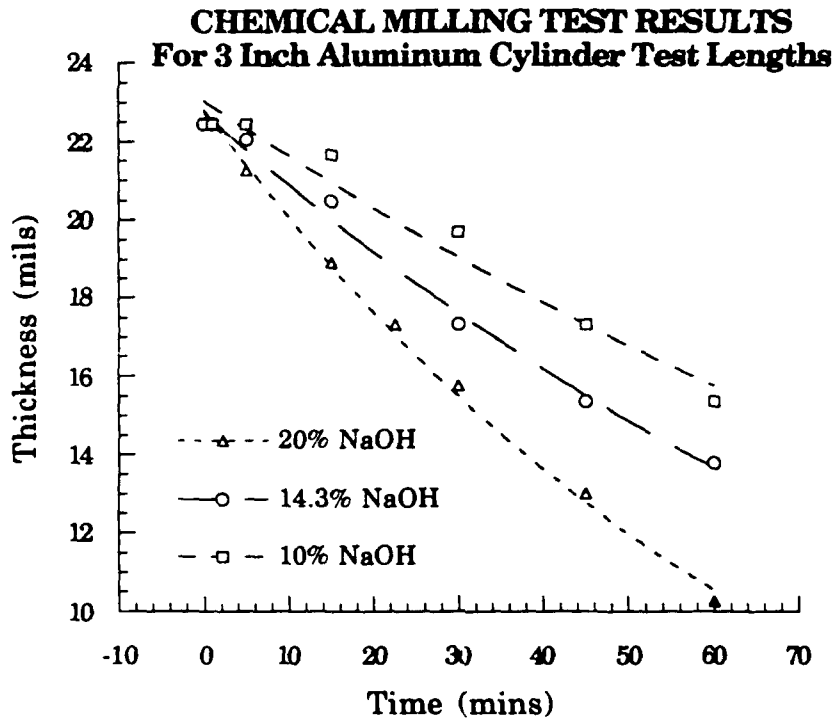
FIGURE 5.1: Chemical Milling Sample Test Results

5.2.2 COMPOSITE CYLINDERS FOR THE HYBRID AND ALL-COMPOSITE P-STRUTS

The composite manufacturing process was completed in the Technology Laboratory for Advanced Composites (TELAC) at MIT. Reference 28 details the materials, preparation, and cure cycle followed.

For the hybrid vessel, the milled aluminum cylinder was hand wrapped in one ply of AS4/3501-6 35% resin graphite-epoxy composite prepreg with fibers in the hoop (90°) direction. For the all composite vessel

the laminates [90/∓60/90] were cut and laid-up around a non-porous Teflon coated aluminum mandrill. For both P-Struts each composite ply was overlapped at its joints to allow some thermal expansion during curing. the overlaps are potential locations of voids see Figure 5.2. Conforming the plies to the cylindrical shape increased the difficulty of the layup process.

The cylinder was covered with several materials in preparation for curing. Figure 5.3 depicts these material layers. The hybrid cylinders were cured without a bleeder pad. The all-composite cylinder included one layer of bleeder paper. A shrink fit material, which was the outer layer, was secured to the mandrill with flash tape. This layer contracted during the cure, applying pressure to the composite cylinders.

The cure cycle followed was 1 hour at 240°F (116°C) and 2 hours at 350° (177°C) with an 8 hour post-cure at 350°F (177°C). No external pressure was used. The oven temperature was set via a dial and the temperature was measured by a thermocouple inside the oven and reported by a digital readout. The ramp time is approximately 5°F (2.7°C) per minute. The cooling time was not specified.

The cured tubes were removed from the oven and the mandrill after cooling to near room temperature. The composite cylinder thickness was measured at the ends with a caliper. The dimension were reported in Table 4.4. Since a single composite laminate is approximately 5.3 mil (0.134 mm) thick, the measured composite thicknesses, t_{comp} (listed in Table 4.5) were significantly higher than anticipated. The additional thickness was assumed to be epoxy or possibly voids. This explanation is based on the issue of composite conformability and not having used a vacuum during the
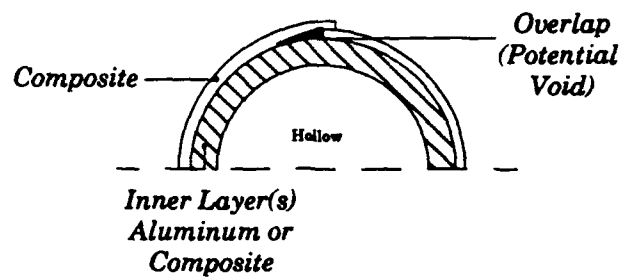
FIGURE 5.2: Overlap of Composite Plies During Layup Cross-Sectional View
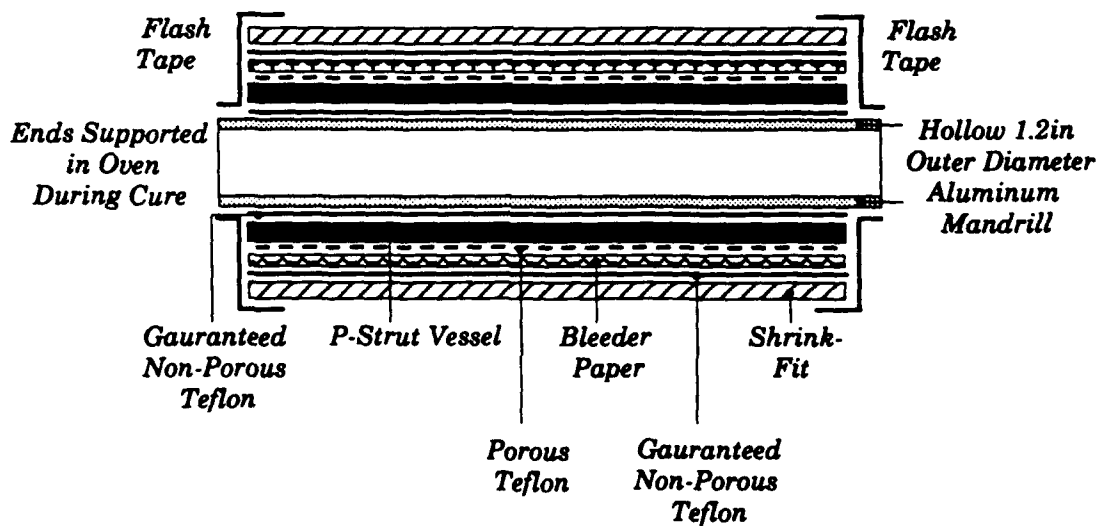

FIGURE 5.3: Axial Cross-Section: P-Strut Cure Preparation

cures. To avoid exaggerating the laminate stiffnesses, the data analysis assumed the composites were formed from plies of graphite fibers 5.3 mil thick surrounded in epoxy t_{comp} thick.

Viewing the cured hybrid cylinder from one end indicated that the cylinder had deformed slightly into an elliptical shape. This was caused by the shrink-fit forcing the aluminum-composite vessel to fit the slightly smaller mandrill on which the cylinder was cured. Small wrinkles on the inner and outer surfaces of the all-composite P-Strut cylinder were noted.

5.2.3 ATTACHING ENDCAPS

The endcaps pictured in Figures 4.4 through 4.6 were attached to the cured cylinders with 3M Scotch Weld 2216 B/A Gray Epoxy Adhesive. This epoxy has high axial and shear stiffnesses [43]. The epoxy cures at room temperature in 8-12 hours with a full cure in 7 days [43]. No testing was conducted before waiting at least 24 hours.

5.2.4 FILLING THE CYLINDER WITH VISCOUS FLUID

Having sealed the P-Strut vessel, the viscous fluid (reference Table 4.4) was forced into the cylinder under pressure. The setup used in pictured in Figure 5.4. A port on one endcap was utilized to fill while a second bled off the air in the cylinder. In order to remove the air trapped in the bellows/orifice, the bellows was filled such that air would rise out of the bellows (see Figure 5.4). In addition, the bellows were pumped repeatedly during the filling/bleeding procedure in attempt to force the air inside the bellows out into the cylinder where it could be bled off.

After filling the cylinder as completely as possible with this procedure, two screws were inserted into the bleed/fill holes. The two

screws, coated in Teflon tape, were screwed into the cylinder, slightly pressurizing the fluid. This was done to reduce the size of any residual air bubbles.

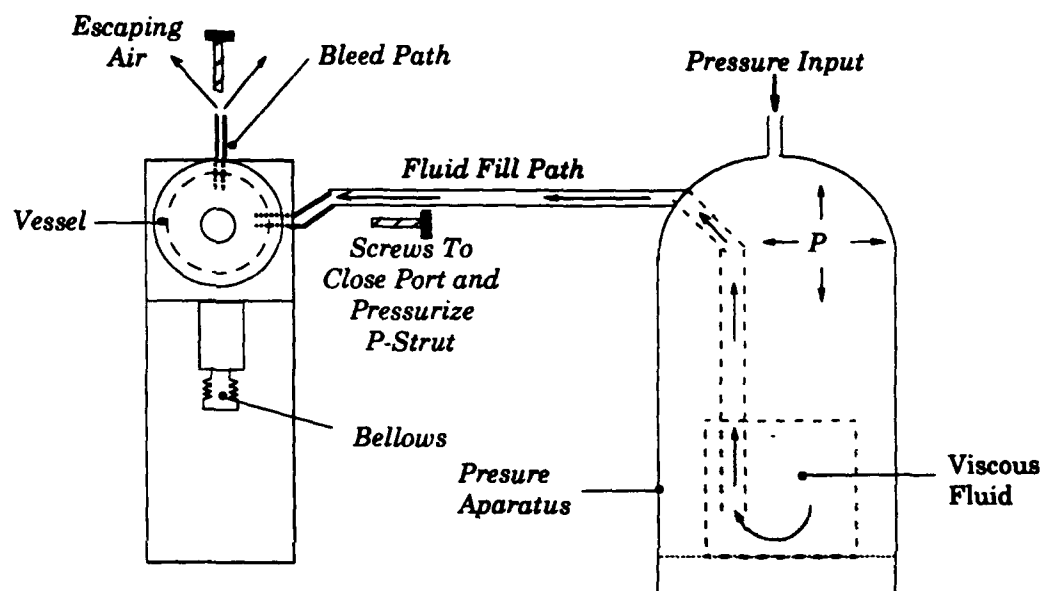

FIGURE 5.4: Bleed/Fill Diagram

5.3   INSTRUMENTATION AND EXPERIMENTAL PROCEDURE

The objective of the experiments was to demonstrate the feasibility of the P-Strut as a fluid elastic actuator and to verify the models developed in Chapter 3.

5.3.1 INSTRUMENTATION

Figure 5.5 illustrates a side view of the P-Strut with the experimental instrumentation labeled. For static testing six types of data were gathered: input stroke, input force, longitudinal strain, hoop strain, internal pressure, and elongation. These measurements provided enough information to confirm the static analysis of Section 3.3. During passive and active testing only the end displacement and the input force (i.e. disturbance force for passive testing, and input force into bellows for active testing) were recorded.

Table 5.1 lists the instrumentation used in the experiments. The data was digitally acquired and processed via a 2630 Tektronics Box connected to a Gateway 2000 (IBM compatible) computer system.

The elongation was measured with a Zygote Laser Interferometer which is part of a component tester. The component tester is depicted in Figure 5.6. The interferometer operates by sensing the difference in distance between a beam reflected from the end of the P-Strut and a reference beam.

In the passive experiments, a Piezo Instruments 244.30 Piezotranslator with a load cell was used to produce and measure a disturbance force. In the static and active tests, the piezotranslator (i.e. disturbance source) was disconnected, releasing the end of the P-Strut to elongate freely. The Tektronics Box outputted a signal to command the solenoid in the active tests or the piezotranslator in the passive tests. These signals were amplified by a Crown D-150A-II Amplifier for the solenoid and a Kepco BOP-500M Amplifier for the piezo actuator.
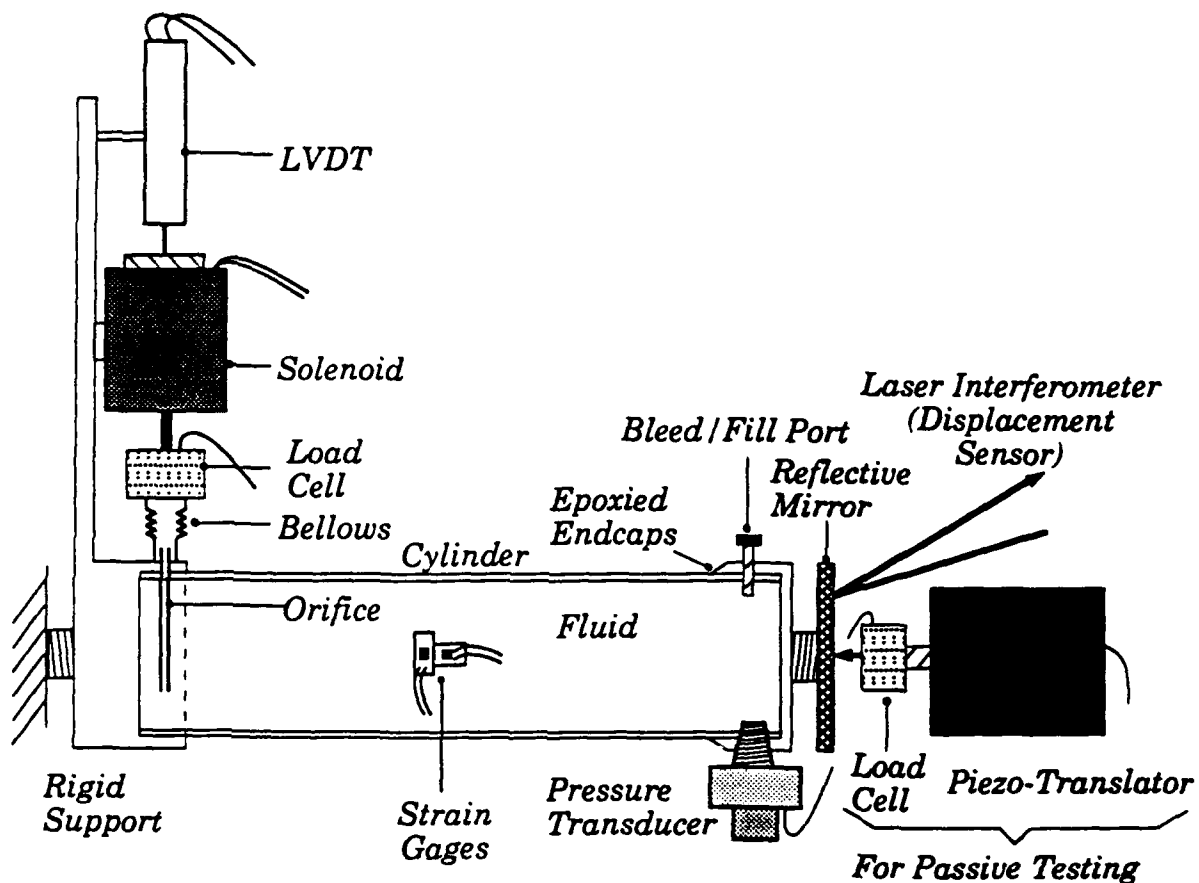
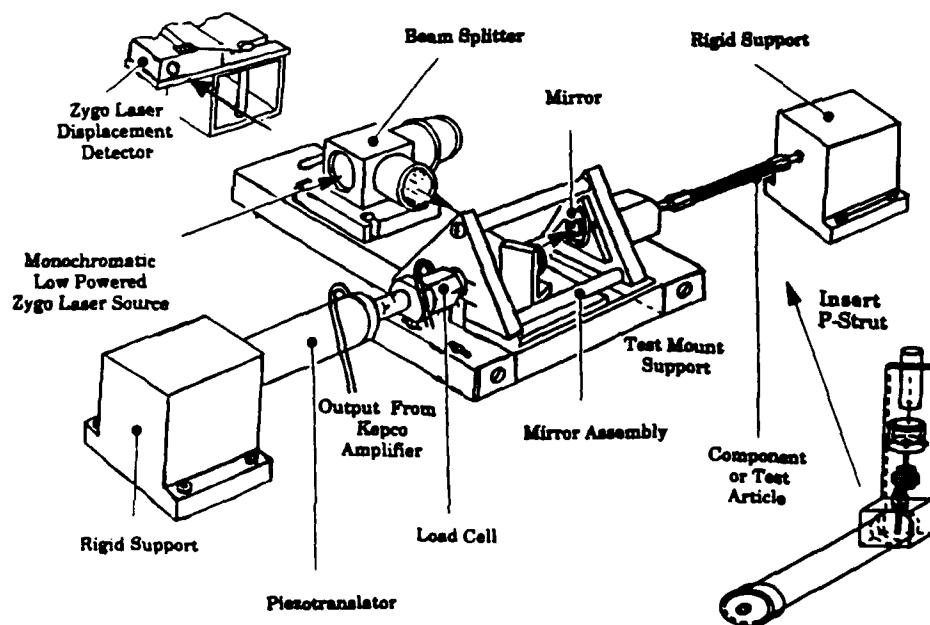FIGURE 5.5: P-Strut Instrumentation (Reference Table 5.1)

FIGURE 5.6: View of Component Tester

113

TABLE 5.1: Instrumentation List and Characteristics

Measurement Variable	Instrumentation (Type/Manufacturer)	Input Voltage	Sensitivity	Range	Noise or Resolution
Input Stroke (δ_b)	Trans-Tek DC LVDT	24 V	20.26V/in	±1in	N A
Input Force (F_b)	PCB Piezotronics 208A02 Loadcells with Conditioner	20V	50.5mV/lb	±500lb	±0.002lb
Dist. Force (F_d)	PCB Piezotronics 208A02 Loadcells with Conditioner	20V	50.5mV/lb	±500lb	±0.002lb
Long. Strain (ε_{11})	Measurement Group Strain Gages 350Ω[1], 120Ω[2], and 120Ω[3]	≈3V	2.5V/mε	±0.5mε	±5-20$\mu\varepsilon$
Hoop Strain (ε_{22})	Measurement Group Strain Gages 350Ω[1], 120Ω[2], and 120Ω[3]	≈3V	2.5V/mε	±1mε	±5-10$\mu\varepsilon$
Pressure (P)	Omega PX236 Piezoresistive Pressure Transducer	10V	1mV/psi	100psi	±0.25psi
Elongation (δ_L)	SERC Component Tester w/ Zygote Laser Interferometer	N A	±0.08mil/V	±0.8mil	±1%/sec drift

[1] Strain Gage Rosette on Isotropic P-Strut: CEA-06-125UR-350

[2] Two Separate Gages (Longitudinal/Hoop) on Hybrid P-Strut: EA-06-031DE-120

[3] Strain Gage Rosette on Composite P-Strut: CE-06-125UT-120

(Note: Different strain gages were used due to availability constraints. The strain gages were set to the desired sensitivity by the gains on the Vishay 2120A Instrument and re-balanced frequently. The ranges were set by input voltage limits for the Tektronics Box.)

5.3.2 STATIC EXPERIMENTAL PROCEDURE

The static tests were conducted by inputting a voltage step into the solenoid and observing the steady-state responses of the instruments. The data was acquired approximately one second past the time to rise as defined in Section 3.6.2. Timing started at the instant the force was applied.

Each test collected data for a single load level. At least 30 tests were conducted at a variety of load levels to characterize the static response. The input voltage levels varied from 5 VDC to 20 VDC which correspond approximately to 0.2 lbf (0.9 N) to 2.5 lbf (11.1 N). Data was acquired in both directions (i.e. increasing force levels and decreasing force levels).

The solenoid loadcell had an inherent AC coupling in the sensor which meant the steady state value decayed to zero. Therefore, the input force, F_b, (which was measured with the loadcell) was read at the first reasonable point after the step input. Initially the loadcell would read a spike in the force due to the impact nature of a step input. However, the spike would return to a plateau before beginning to decay. This value was considered the correct measurement of the input force. The laser interferometer system had a minor (approximately 1% per second) drift which could have been temperature dependent. Since data was collected within a few seconds, the effect was considered negligible.

5.3.3 PASSIVE EXPERIMENTAL PROCEDURE

The Tektronics system generated a dynamic signal that was random in frequency within a specified bandwidth. This signal was amplified through the Kepco Amplifier. The output drove a piezo actuator (see Figure 5.5 and 5.6) which provided the disturbance force. The disturbance force, F_d, was measured via a loadcell; the resulting elongation of the P-Strut, δ_L, was measured by the laser interferometric system. Both measurements were recorded by the Tektronics box.

The Tektronics box automatically acquired 800 points of data over the bandwidth during each measurement cycle. The length of time required for each cycle was defined by the bandwidth and the number of data points. The digital acquisition system calculated, for each cycle, the Bode plot of the stiffness transfer function, F_d/δ_L (see Chapter 2 for definition of Bode plot and reference). The recorded transfer function represents at least ten cycles of data averaged automatically by the digital acquisition system.

5.3.4 ACTIVE EXPERIMENTAL PROCEDURE

In the active experiments, a random frequency voltage signal was generated by the output of the Tektronics Box, amplified by the Crown amplifier, and applied to the solenoid creating a dynamic input force, F_b. The input force was sensed by a load cell attached to the solenoid (see Figure 5.5). The resulting dynamic elongation of the P-Strut was measured via the laser interferometer.

The Tektronics box automatically acquired at least 400 points of data over the bandwidth during each measurement cycle. The length of time required for each cycle was defined by the bandwidth and the number of data points. The digital acquisition system calculated, for each cycle the Bode plot of the admittance transfer function, δ_L/F_b. The recorded transfer function represents at least ten cycles of data averaged automatically by the digital acquisition system. The input was constrained by the hardware to a two decade frequency range. The range was selected, based on preliminary tests, to include the roll-off of the active response in the Bode Diagram.

CHAPTER 6:

Experimental Results and Correlation

6.1 CHAPTER OUTLINE

In this chapter, experimental results for the P-Strut are presented and correlated. Three P-Struts were tested in the static, passive, and active modes of operation.

The static measurements appear linear although there is significant scatter in some of the data. The static equations of Section 3.3 show good agreement with the data. The values of two unknown parameters were ascertained from the data.

The passive data acquired indicated damping which was not directly traceable to the orifice. The damping source was modeled in Section 3.5 as the epoxy used in attaching the endcaps. The epoxy model parameters are fit to the measured data and the revised model is discussed.

The active model correlates with the active measurements verifying the modeling procedure and the analysis presented in Chapter 3. The

117

modeled roll-off of the actuator authority agrees with the experimental results from the isotropic and composite P-Struts.

6.2   STATIC PERFORMANCE EVALUATION

6.2.1   STATIC EXPERIMENTAL RESULTS

The static results are depicted in Figure 6.1 through 6.14. The first six figures illustrate the six types of data acquired for the isotropic aluminum P-Strut which contained 10K cs silicon fluid. Figures 6.7 through 6.12 illustrate the performance measures of the hybrid P-Strut filled with three different fluids. The last pair of plots (Figure 6.13 and 6.14) represent the static performance of the composite P-Strut filled with glycerol fluid. Each plot includes a line corresponding to the static model predictions.

Figure 6.1 depicts the measured longitudinal strain versus hoop strain in the isotropic cylinder. The scatter is probably the result of noise in the longitudinal strain gage noted in Table 5.1. Figures 6.2 to 6.4 show the hoop strain, pressure, and input stroke graphed against the input force. Figure 6.5 illustrates the static performance of the isotropic P-Strut as measured by actuation displacement versus the input force. The actuation displacement versus the input stroke is depicted in Figure 6.6. A moderate input force (2 lbf or 9N) over a moderate input stroke (0.15 in or 0.38 cm) produces a small but precisely controlled elongation of approximately 0.5 mil (0.13 mm). Due to limitations in the number of data collection channels available in the acquisitional hardware not every data type was collected

during every test. This accounts for the differing maximum elongation values plotted in Figure 6.5 and 6.6.

Figure 6.7 and 6.8 show the static performance of the hybrid P-Strut filled with 10K cs silicon fluid. Due to the more massive cylinder wall, the maximum elongation is slightly less than for the isotropic P-Strut. Figure 6.9 and 6.10 depict the performance of the same P-Strut filled with 30K cs silicon fluid. No significant change in performance is noted. Figure 6.11 and 6.12 depict the performance of the hybrid P-Strut filled with glycerol. A modest increase in performance is noted.

Figures 6.13 and 6.14 shows a dramatic increase in static performance for the composite P-Strut over the aluminum and hybrid P-Struts.

6.2.2 CORRELATION OF THE STATIC RESULTS

Table 6.1 lists the performance metrics, elongation per unit force (δ_L/F_b) and elongation per unit input stroke (δ_L/δ_b). The data values were computed by determining the slope of the least squares fit of the data plotted in the figures. The model values were calculated as follows.

The unknown effective cross-sectional area of the bellows, A_b, was determined such that the absolute error between the static model predictions and the least squared linear fits to selected data was minimized. The selected data consisted of the six comparisons of the types shown in Figure 6.1 through 6.6. An effective A_b was determined for each P-Strut independently.

Due to the accidental out of specification distortion of the bellows during testing of the aluminum P-Strut, the effective cross-sectional area was higher than either value determined for the hybrid or composite

119

P-Struts. A new bellows was used in the composite P-Strut which had a calculated effective area only slightly less that than that of the hybrid P-Strut. Due to the uncertainty in the properties of the chemically milled aluminum tubes, the assumed Young's Modulus for the aluminum tube (and the aluminum in the hybrid tube) was adjusted to be 8.5 Msi (59 GPa) and a P isson's Ratio was assumed to be 0.32. All other material properties and dimensions are found in Tables 4.1, 4.3, and 4.4. These values were used to compute the model parameters (from equations 3.79 through 3.82) reported in Table 6.2.
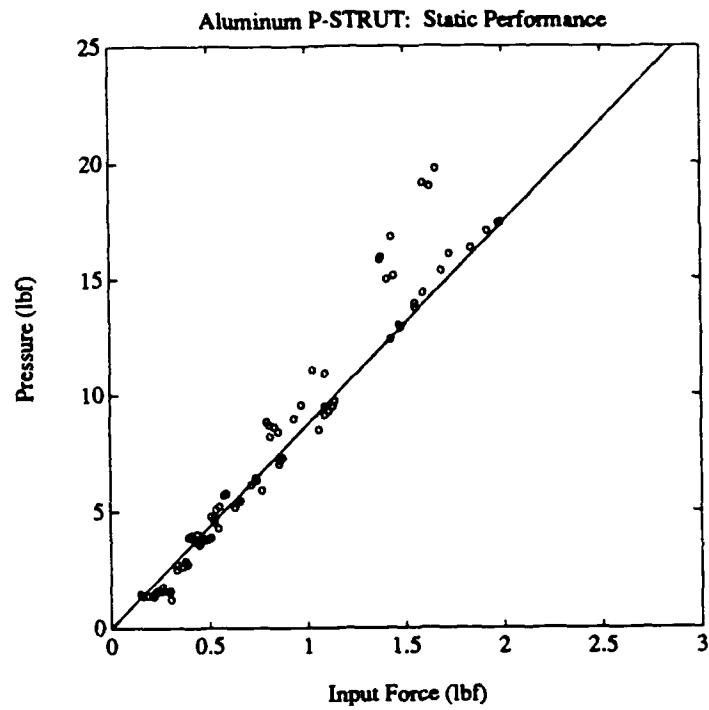
The agreement between the model and data is good. In most cases, the model under predicts the performance of the aluminum P-Strut and over predicts the performance of the hybrid P-Struts. The model correctly predicts the greatly improved performance of the composite P-Strut.
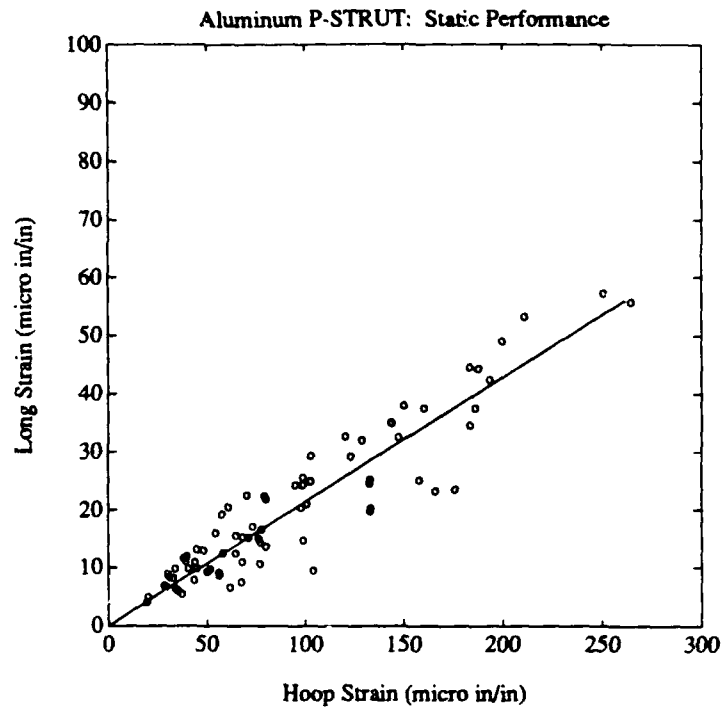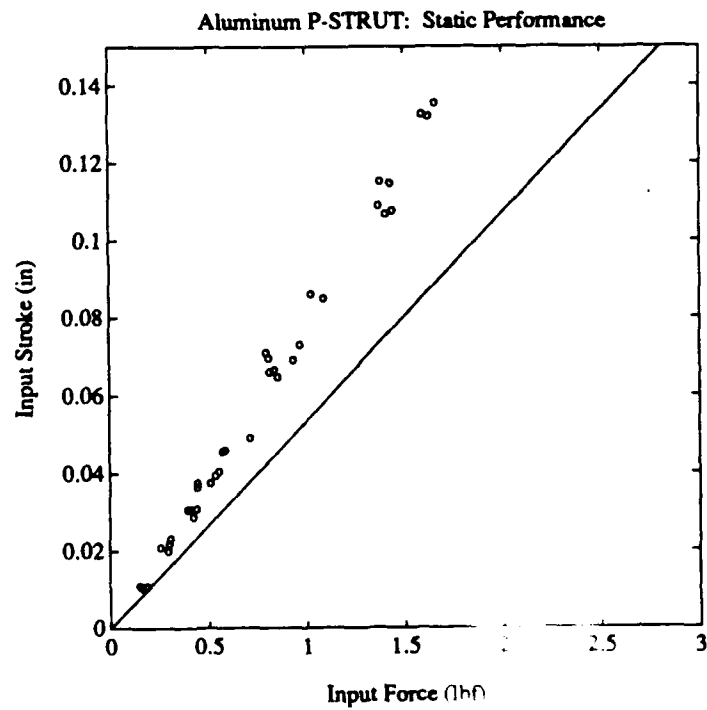
FIGURE 6.1: Longitudinal Strain vs. Hoop Strain
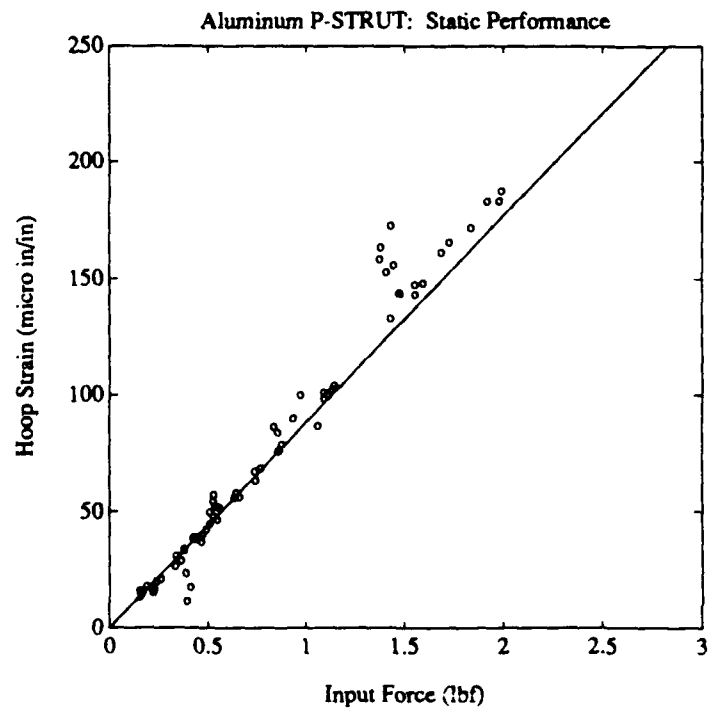
FIGURE 6.2: Hoop Strain vs. Input Force

121

FIGURE 6.3: Pressure vs. Input Force

FIGURE 6.4: Input Stroke vs. Input Force

122
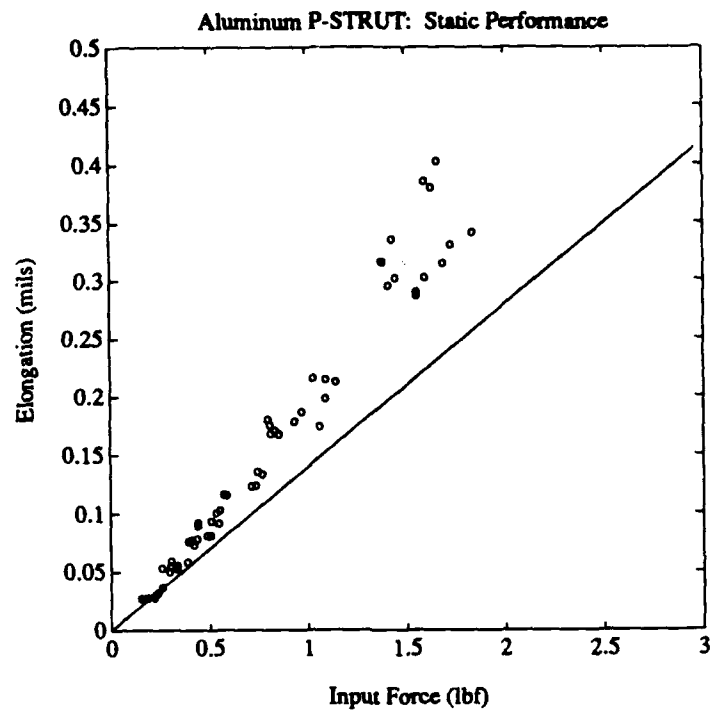
FIGURE 6.5: Isotropic Performance: Elongation vs. Input Force
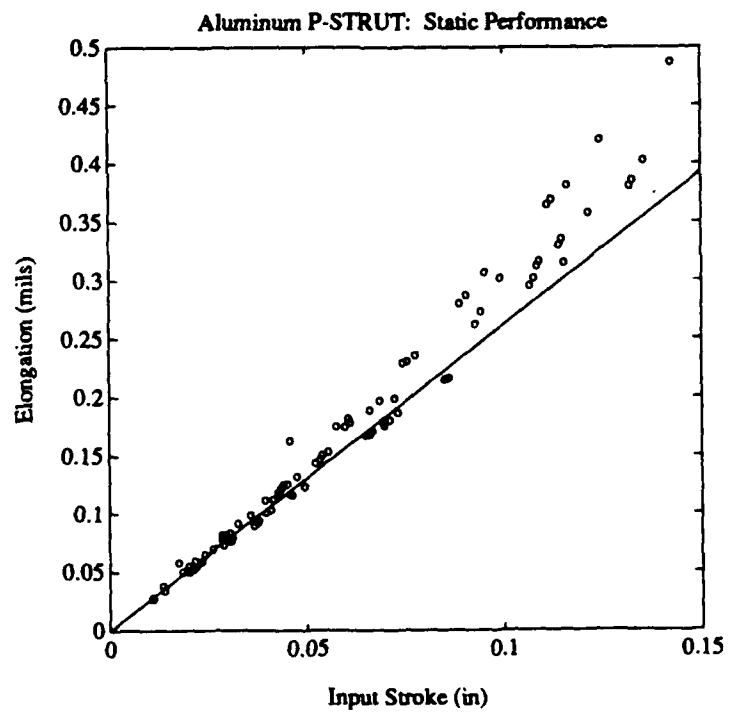
FIGURE 6.6: Isotropic Performance: Elongation vs. Input Stroke

Hybrid Al-Comp P-STRUT: Static Performance
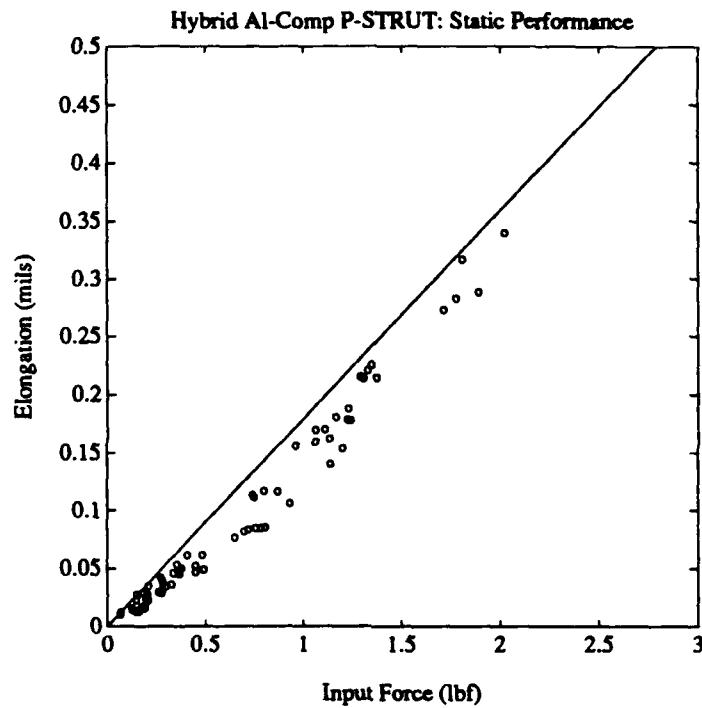
FIGURE 6.7: Hybrid Performance with 10K cs Silicon Fluid:
Elongation vs. Input Force

Hybrid Al-Comp P-STRUT: Static Performance
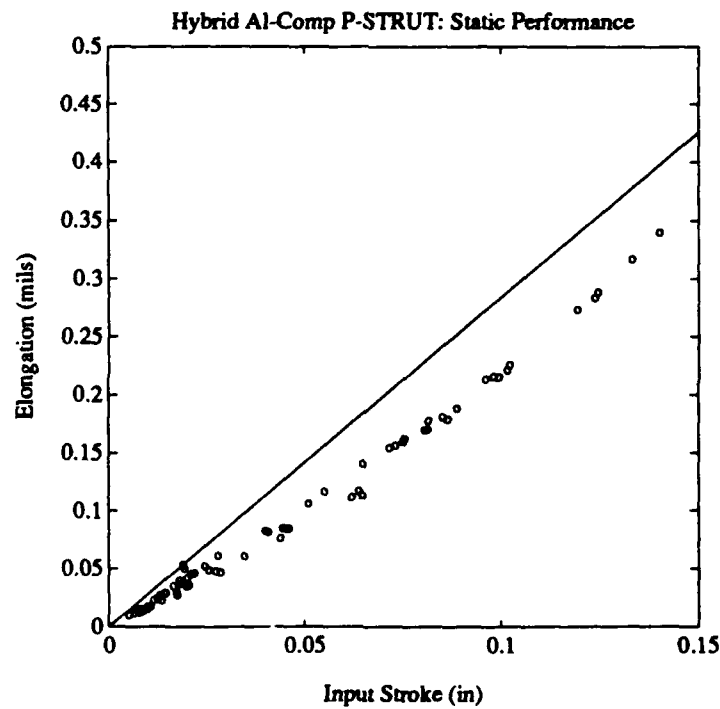
FIGURE 6.8: Hybrid Performance with 10K cs Silicon Fluid:
Elongation vs. Input Stroke

124
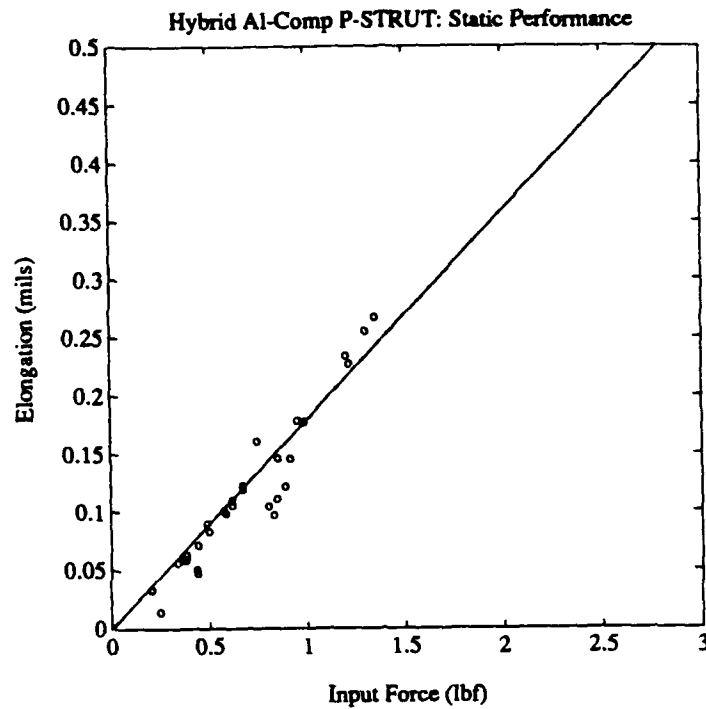
FIGURE 6.9: Hybrid Performance with 30K cs Silicon Fluid: Elongation vs. Input Force

FIGURE 6.10: Hybrid Performance with 30K cs Silicon Fluid: Elongation vs. Input Stroke

125

FIGURE 6.11: Hybrid Performance with Glycerol Fluid: Elongation vs. Input Force

FIGURE 6.12: Hybrid Performance with Glycerol Fluid: Elongation vs. Input Stroke
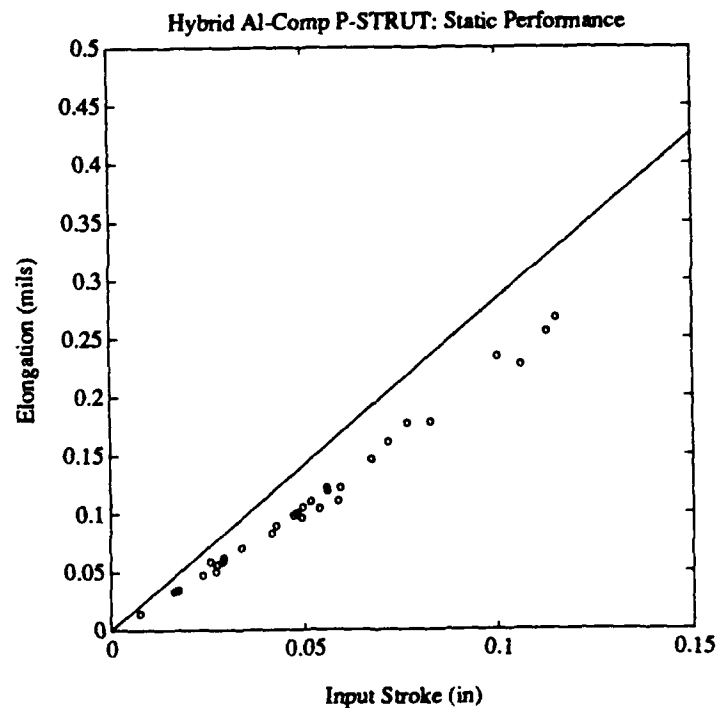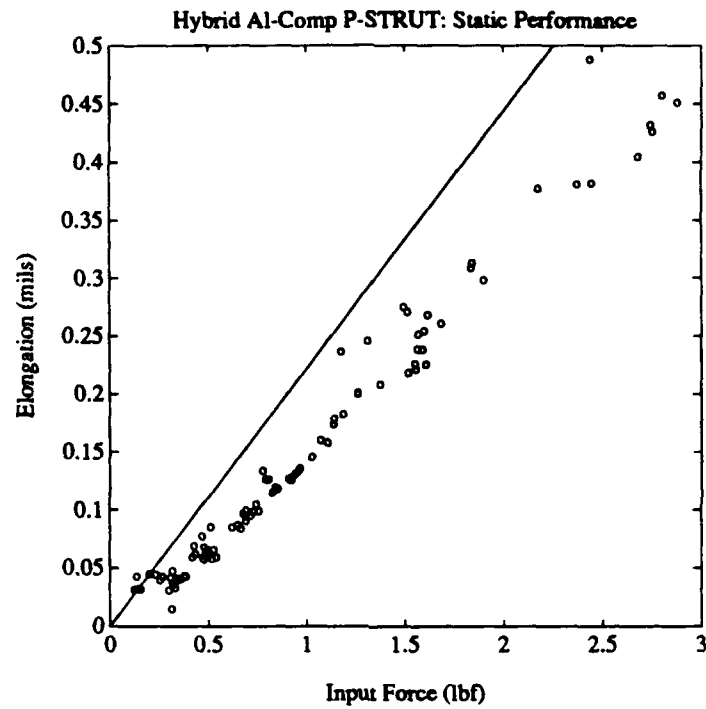
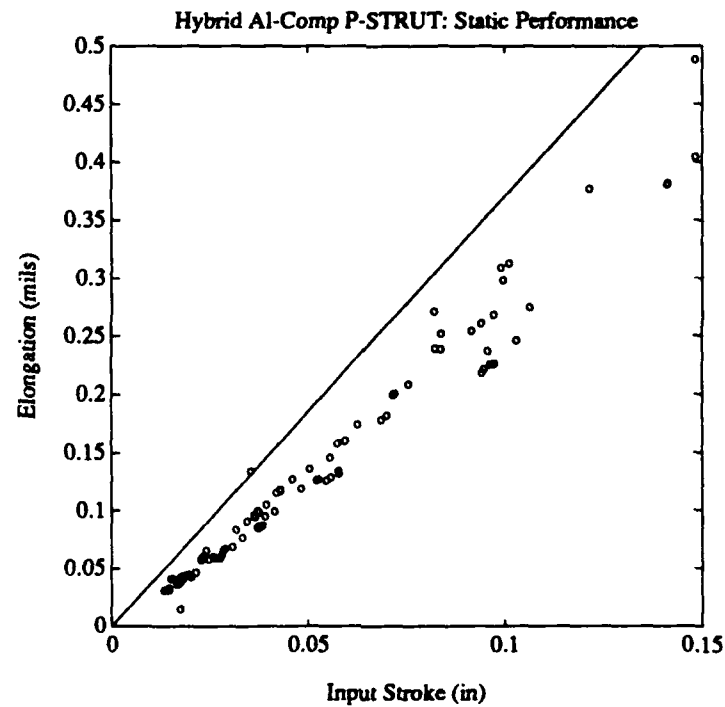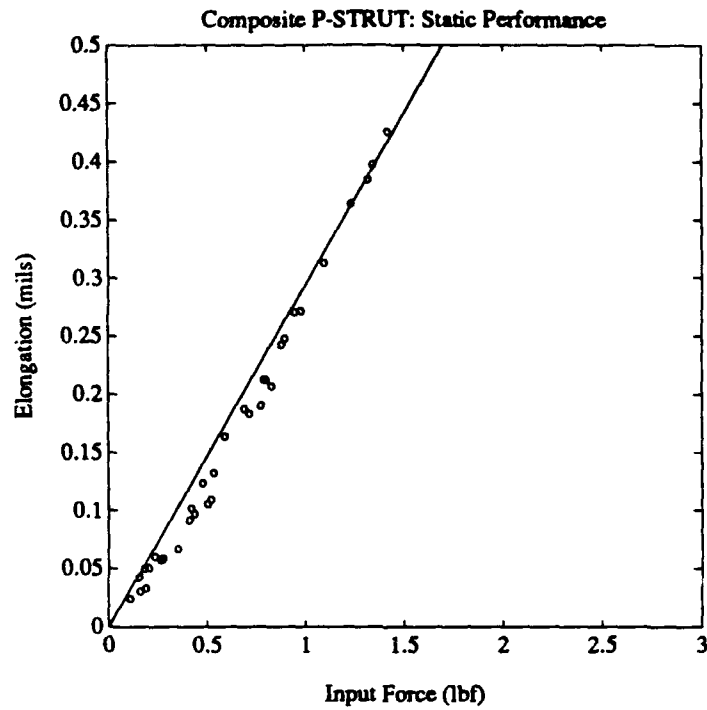FIGURE 6.13: Composite Performance: Elongation vs. Input Force
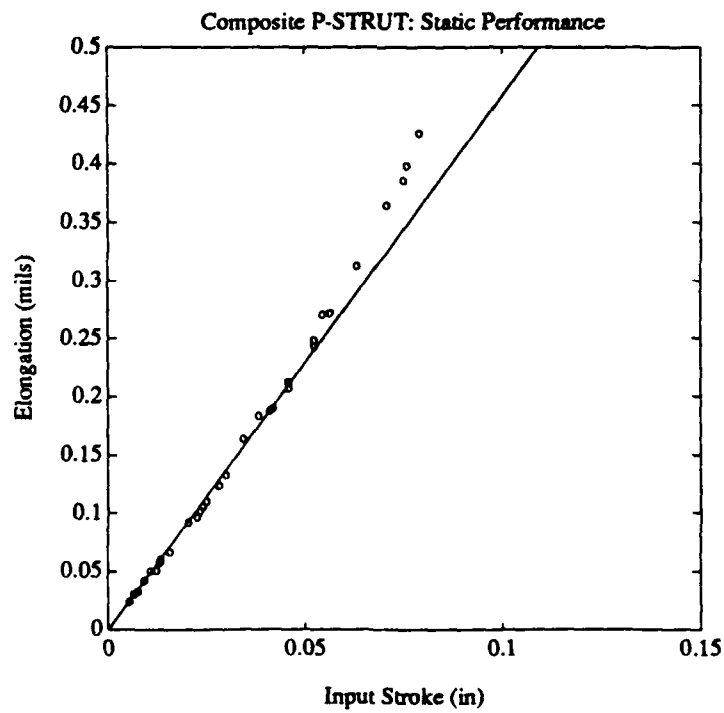
FIGURE 6.14: Composite Performance: Elongation vs. Input Stroke

127

TABLE 6.1: Static Performance Results

P-STRUT CYLINDERS/FLUIDS

Performance Metric		Aluminum 10K cs Silicon	Hybrid 10K cs Silicon	Hybrid 30K cs Silicon	Hybrid Glycerol	Composite Glycerol	
δ_L/F_b	Data	0.20	0.15	0.17	0.16	0.28	mil/lbf
δ_L/F_b	Model	0.14	0.18	0.18	0.22	0.29	mil/lbf
δ_L/δ_b	Data	2.95	2.18	2.18	2.70	4.99	mil/in
δ_L/δ_b	Model	2.53	2.81	2.81	3.67	6.99	mil/in

TABLE 6.2: Constants Used in Correlation of Static Performance Results

P-STRUT CYLINDERS/FLUIDS

Parameter	Aluminum 10K cs Silicon	Hybrid 10K cs Silicon	Hybrid 30K cs Silicon	Hybrid Glycerol	Composite Glycerol	
A_b	0.35	0.17	0.17	0.17	0.11	in^2
L_{eff}/L	1.03	1.01	1.01	1.01	1.01	% of L
K_b	13	13	13	13	13	lbf/in
K_L	73.7	67.4	67.4	67.4	58.3	K lbf/in
K_R	8.2	28.8	28.8	28.8	87.2	K lbf/in
K_F	33.5	34.7	34.7	95.3	120.9	K lbf/in
K_S	27.7	46.5	46.5	46.5	50.4	K lbf/in

6.3 PASSIVE PERFORMANCE EVALUATION

6.3.1 PASSIVE EXPERIMENTAL RESULTS

Figure 6.15 through 6.18 shows the results of the passive tests on the three P-Struts. The Bode magnitude and phase of the disturbance force per unit axial elongation are shown, along with model correlations to be discussed below. Figure 6.15 shows the passive performance of the aluminum P-Strut filled with 10K cs silicon fluid and fitted with an 84 mil diameter 1.1 in length orifice. The hybrid P-Strut containing 10K cs silicon fluid with an 82 mil diameter 0.9 in length orifice is pictured in Figure 6.16. Figure 6.17 depicts the hybrid P-Strut without fluid. The composite cylinder with an 82 mil diameter 0.9 in length orifice and filled with glycerol is depicted in Figure 6.18.

The behavior of the classic zero-pole system as discussed in Section 3.4 is observed in all cases. Stiffness at zero and infinite frequencies, K_{DCp} and K_{∞_p}, the peak frequency, ω^*, and the maximum loss factor, η^*, are listed in Table 6.3. Alarmingly damping is noted in the hybrid cylinder shown in Figure 6.17 which contains no fluid.

### 6.3.2 CORRELATION OF THE PASSIVE RESULTS

To correlate the passive performance with the measure data, the effective stiffness of the component tester had to be added to the model discussed in Section 3.5. The connection of the piezotranslator to the P-Strut (see Figures 5.5. and 5.6) introduces a stiff in-series spring into the load path which decreases the measured passive performance. The spring

is considered to have a fixed stiffness of 225K lbf/in (40 N/μm) which was determined from experimental calibrations.

Figures 6.15, 6.16, and 6.18 picture the predicted passive damping due to the orifice. In the isotropic and hybrid cases the predicted damping due to the orifice is extremely small and barely noticeably running along the frequency axis. In addition, the stiffness is virtually unchanged throughout the frequency range (i.e. the flat dotted line). In the composite case modest orifice damping is predicted with a peak near 10 Hz. The data does not agree with any of the predictions.

A revised model was d ·lopeu in Section 3.5.7 assuming the epoxy used to attach the endcaps to the cylinder provided additional viscous damping. The damping action of the ˆpoxy was assumed to be sensitive to uncontrolled parameters such as bond thickness; therefore, no attempt was made to calculate the parameters of the epoxy model from material properties and geometry of the bond. Instead the values of the additional model epoxy parameters were determined by fitting the data. These are listed in Table 6.4. For all cases except the composite P-Strut, the revised model fit the data very well. The composite results are not well matched even by the revised model due to the lack of the predicted orifice damping.

The passive results indicate that the P-Strut in its current configuration is not an effective passive damper. Unintentional effects, possibly the epoxy by which the endcaps are attached, demonstrate damping which overwhelms any orifice contribution.

Aluminum P-STRUT: Passive Performance
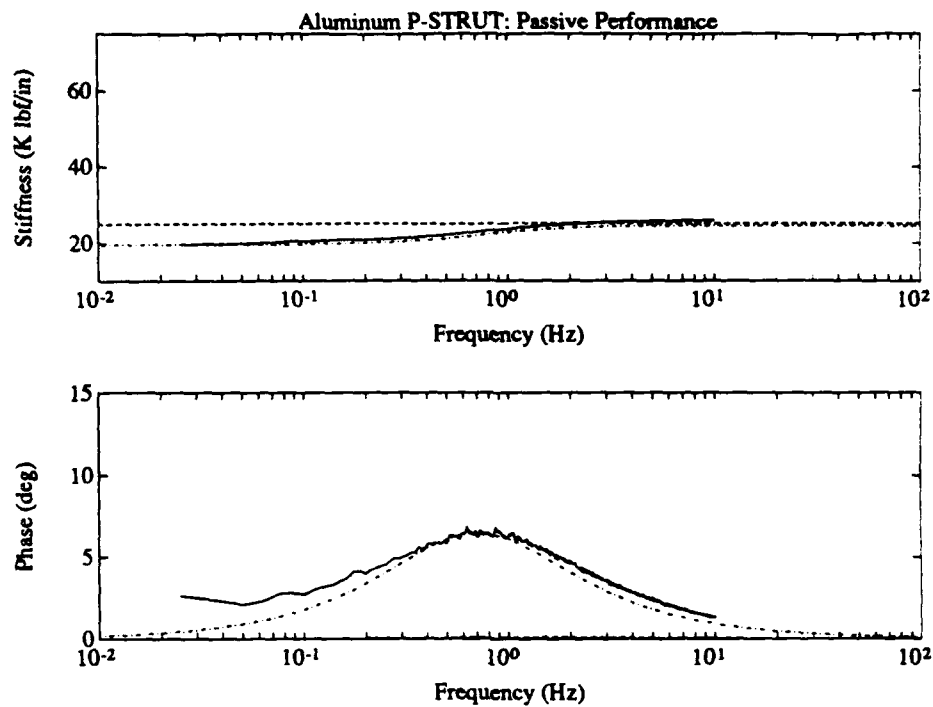
FIGURE 6.15: Isotropic Passive Performance

Hybrid Al-Comp P-STRUT: Passive Performance
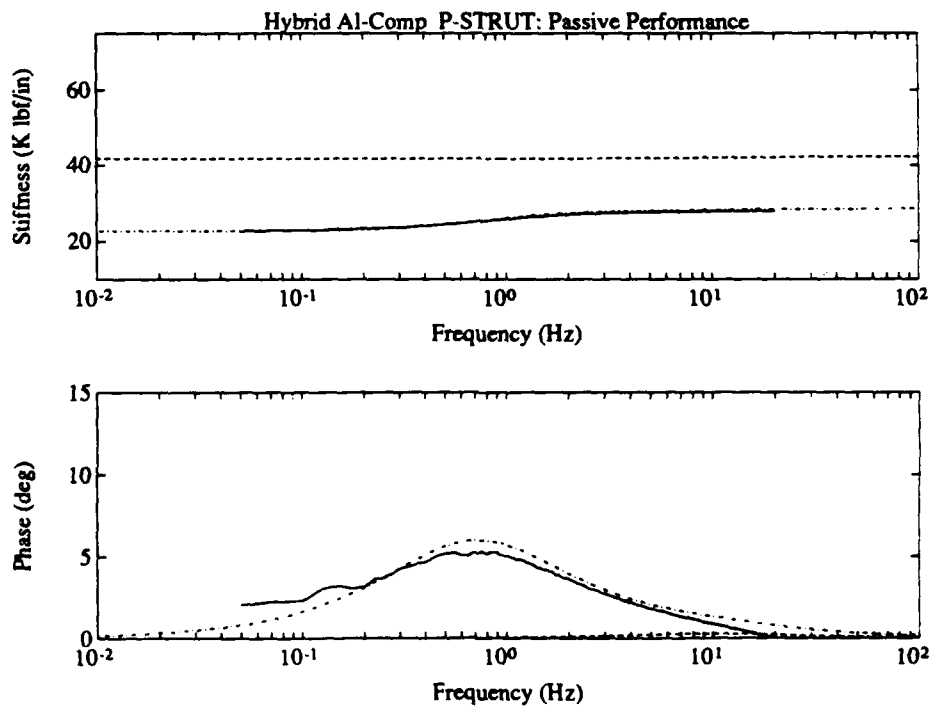
FIGURE 6.16 Hybrid Passive Performance

131
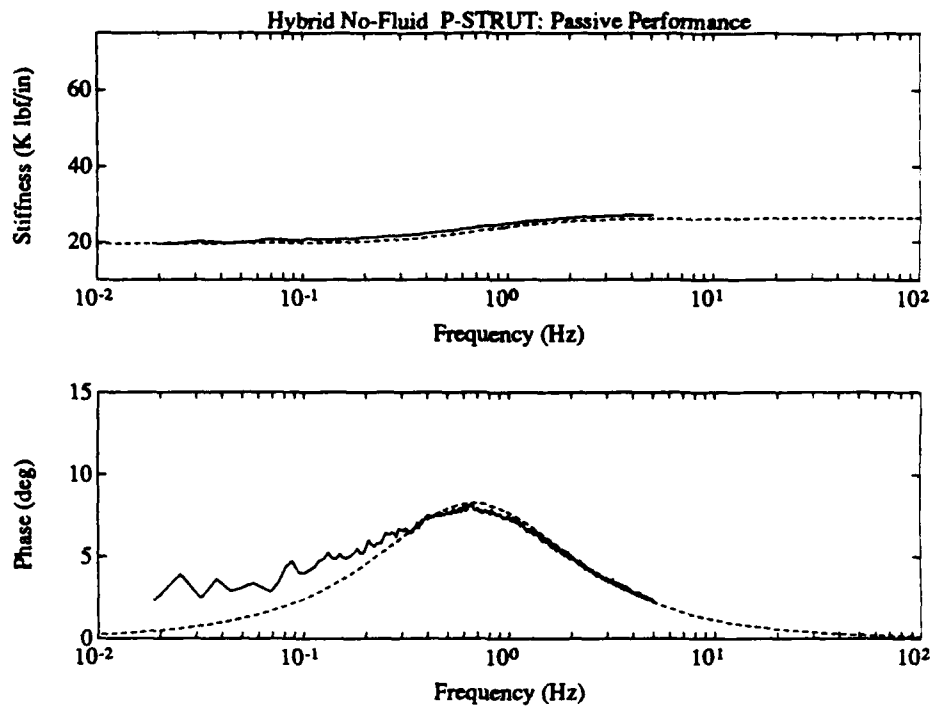
FIGURE 6.17: Hybrid Passive Performance with No Fluid
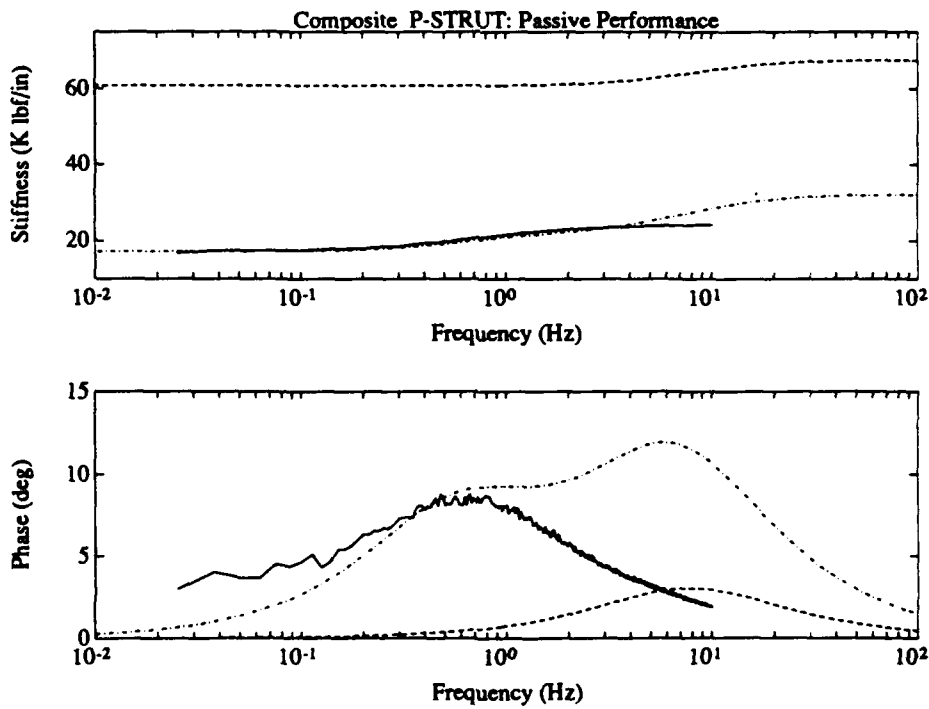
FIGURE 6.18: Composite Passive Performance

132

TABLE 6.3: Measured Passive Performance

P-STRUT CYLINDERS / FLUIDS

Parameter	Aluminum 10K cs Silicon	Hybrid No Fluid	Hybrid 10K cs Silicon	Composite Glycerol	
K_{DCp}	19.91	19.95	22.47	17.35	K lbf/in
$K_{\infty p}$	26.14	27.6	27.96	24.67	K lbf/in
ω^*	0.76	0.68	0.74	0.65	Hz
η^*	0.11	0.15	0.09	0.15	

TABLE 6.4: Epoxy Parameters Fit to Passive Data

P-STRUT CYLINDERS / FLUIDS

Parameter	Aluminum 10K cs Silicon	Hybrid No Fluid	Hybrid 10K cs Silicon	Composite Glycerol	
K_{DCep}	90	40	50	24	K lbf/in
K_{ep}	1000	42	35	10	K lbf/in
C_{ep}	21	5.6	5.1	2.2	K lbf sec/in

6.4 ACTIVE PERFORMANCE EVALUATION

6.4.1 ACTIVE EXPERIMENTAL RESULTS

The results of testing the P-Struts in the active mode are shown in Figure 6.19 through 6.21. The Bode magnitude and phase of the admittance, actuation displacement or axial elongation per unit applied force (δ_L/F_b), are depicted. Figure 6.20 plots the Bode data and model for the aluminum P-Strut with 10K cs silicon fluid and an orifice with a diameter of 84 mil and a length of 1.1 in. Figure 6.21 depicts the data for two hybrid P-Struts both with 82 mil 0.9 in length orifices. The left most data corresponds to the cylinder filled with 30K cs silicon fluid while the second data set corresponds to the same P-Strut containing lower viscosity glycerol fluid. Figure 6.21 depicts the effect of increasing the orifice diameter (or decreasing the orifice damping) for the composite P-Strut filled with glycerol fluid. The orifice diameters correspond with the order of the roll-off data curves such that the highest diameter orifice has the greatest corner frequency. Figure 6.21 depicts the composite P-Strut data for five orifices: 30 mil 1.5 in, 40 mil 1.1 in, 55 mil 1.1 in, 70 mil 1.1 in, and 82 mil 0.9 in orifices.

One-pole roll-off behavior is observed in each case, except the hybrid magnitude data which for unknown reasons appears anomalous. The observed DC admittance, A_{DCact}, and the corner frequency (ω_c) are shown in Table 6.5. The corner frequency of the data was measured as the frequency at which the phase was 45°.

The DC admittance (which corresponds to the static performance of the P-Strut) is much greater for the composite P-Strut than for the aluminum. The effect of the orifice size on the roll-off frequency is clearly seen in Figure 6.21.

6.4.2   CORRELATION OF THE ACTIVE RESULTS

The predictions based on the active performance equations developed in Section 3.6.1 are shown on Figures 6.19 and 6.22 for the aluminum and composite P-Struts respectively. Figure 6.22 shows active performance data of the composite P-Strut with different orifices and the corresponding analytical predictions. Figure 6.22 depicts the composite P-Strut data for three orifices: 30 mil 1.5 in, 40 mil 1.1 in, and 82 mil 0.9 in orifice. The parameters found on Table 6.2, which includes the effective bellows area calculated based on the static results, were used to compute the model performance. No fitting of the model parameters were done to achieve the correlations. The agreement is excellent in all cases. This correlation serves to verify the validity of the active P-Strut model.
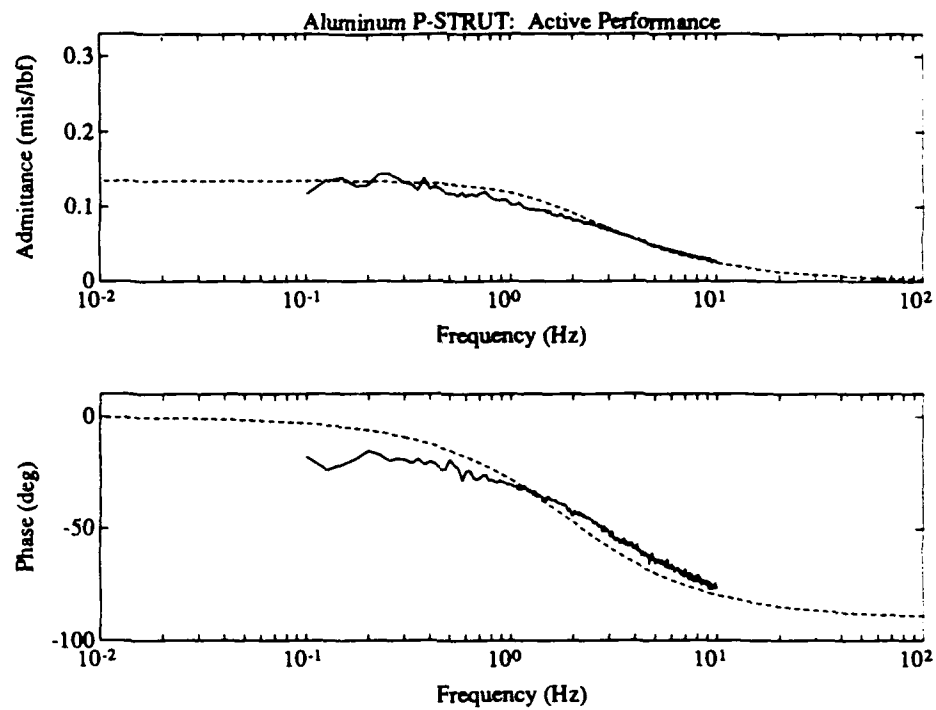
FIGURE 6.19: Isotropic Active Performance
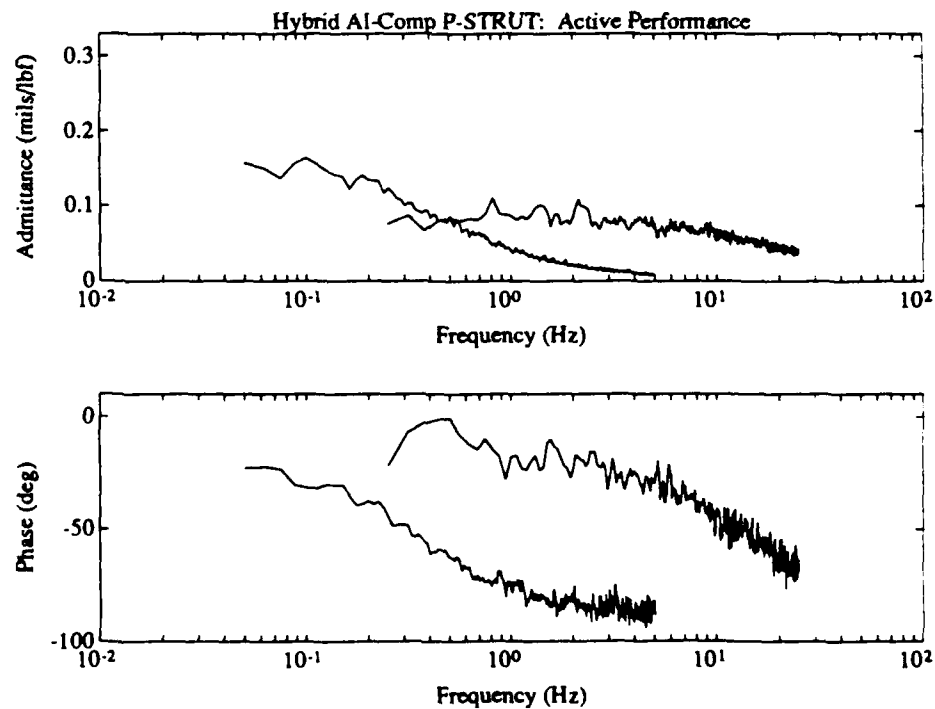
FIGURE 6.20: Hybrid Active Performance with 30K cs Silicon and Glycerol Fluids

136
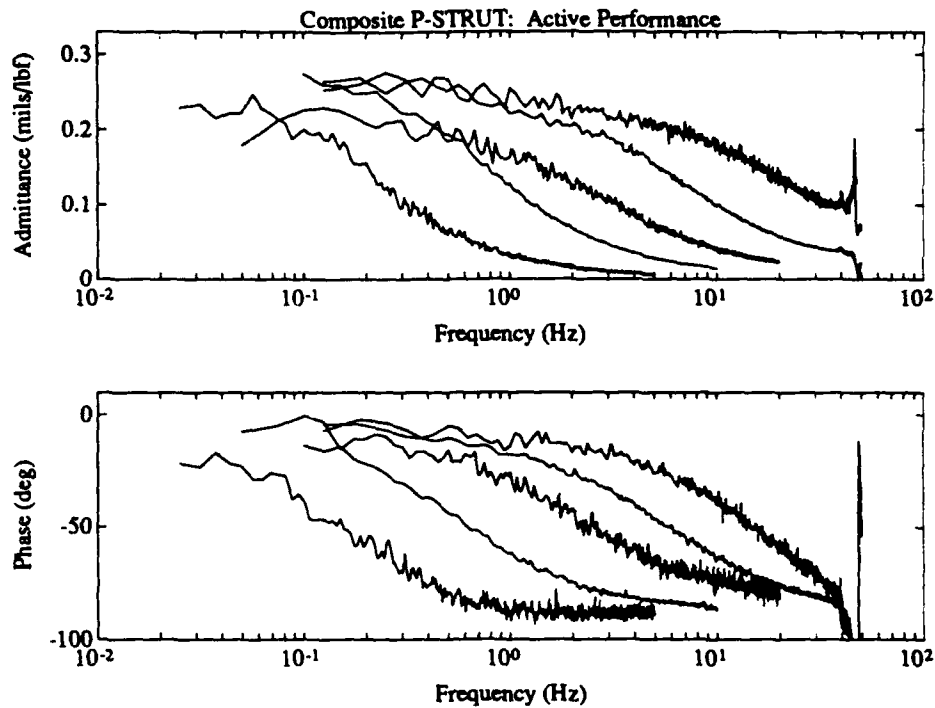
FIGURE 6.21: Composite Active Performance with Increasing
Orifice Sizes (30, 40, 55. 70, 82 mil)
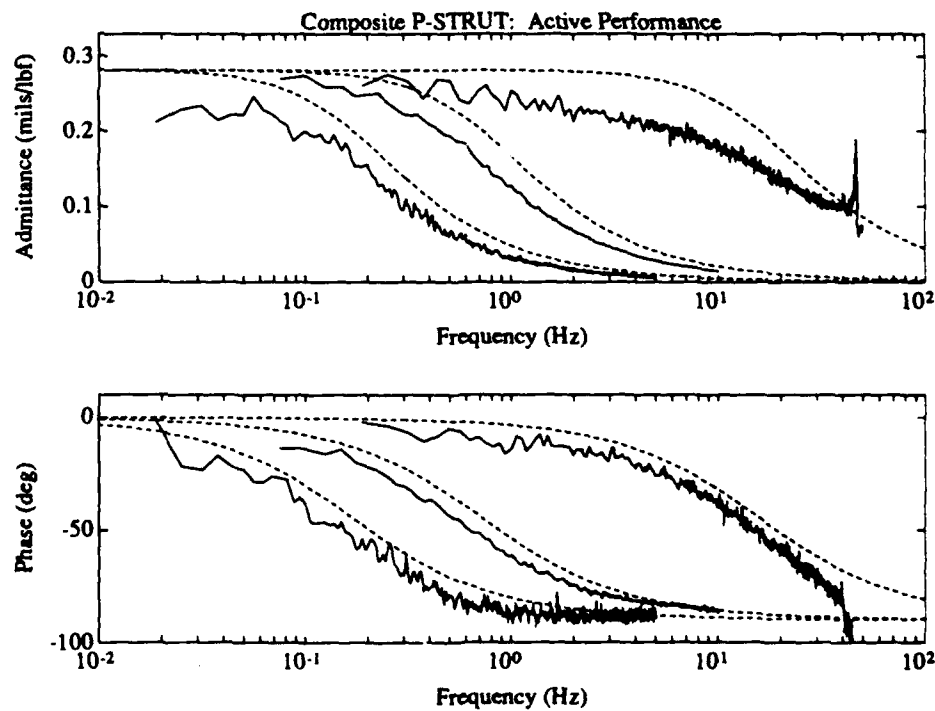
FIGURE 6.22: Composite Active Performance

137

TABLE 6.5: Corner Frequency and Active Performance Admittance

P-Strut Cylinder	Fluid	Orifice Length L_o in	Orifice Diameter D_o mil	Corner Frequency ω_c Hz		DC Admittance A_{DCact} mil/lbf	
				DATA	MODEL	DATA	MODEL
Aluminum	10K cs Silicon	1.1	84	1.85	2.27	0.13	0.14
Hybrid	30K cs Silicon	0.8	63	0.25	1.05	0.15	0.18
Hybrid	Glycerol	0.8	63	13.5	2.77	0.09	0.22
Composite	Glycerol	1.5	30	0.10	0.17	0.23	0.29
Composite	Glycerol	1.1	40	0.55	0.76	0.27	0.29
Composite	Glycerol	1.1	55	2.50	2.69	0.24	0.29
Composite	Glycerol	1.1	70	4.81	7.03	0.27	0.29
Composite	Glycerol	0.9	82	13.7	15.9	0.27	0.29

6.5   DISCUSSION OF RESULTS

The P-Strut concept explained in Chapter 1 has been demonstrated. P-Struts have been tested in static, passive, and active modes.

The orifice damping is not effective in the passive mode. With the current P-Strut the expected effect is small and it is apparently masked by other damping effects—probably the epoxy by which the endcaps are attached. It has been speculated that air trapped in the cylinder or bellows could also be responsible for lack of the passive performance. More fundamental is the non-optimal geometry of the current P-Strut for the passive damping function.

The static results confirm the linear nature of the relationships between input force and stroke, internal pressure, cylinder hoop and longitudinal strains, and axial elongation. The scatter observed in the static data is probably associated with data collecting methods. The data acquisition hardware is designed for dynamic experimentation. The AC loadcell and the laser interferometeric component tester discussed in Section 5.3.2 cannot measure DC data for more than a short time before the signal decays.

Supporting this conclusion, the active test results were very good. The active results verified the P-Strut model developed in Chapter 3. This model allows the geometry and material properties of the P-Strut to be used directly to calculate the responses. This capability aids in understanding the physical principles behind the modes of operations of the P-Strut. This knowledge can be used improve the design or customize the performance.

The importance and usefulness of tailoring the material properties and the geometry have been demonstrated. The optimal composite cylinder greatly improved the performance by constraining the undesirable radial deformations. The choice of fluids effects both the magnitude of the performance via the fluid bulk modulus and the corner frequency in the active performance via the fluid viscosity. The orifice diameter has a demonstrated strong effect on the roll-off frequency.

The P-Strut presented here, can be used as an actuator in a controlled structures application. Its static stiffness and actuation authority are similar to that of other actuators such as a piezotranslator. Advantages of the P-Strut include the linear response to an input command and use of "off the shelf" hardware. Conceptually, the P-Strut could be improved by the addition of passive damping, however the geometry of the fluid elastic actuator would need to be optimized for this purpose. For example, the Honeywell D-Strut as described in Section 3.5.5 is a fluid elastic mechanism optimized for passive damping. The usefulness of the P-Strut in its current configuration is to provide axial actuation within a specified bandwidth.

Although the bandwidth limits the modes which can be targeted for damping, it beneficially prevents the amplification of noise. Physically, the P-Strut cannot command displacement or force above a set frequency. Therefore, even if an active control compensator is unstable at high frequencies or the feedback noise is severe, the actuator cannot add energy into the higher modes. Simply, a control system using this fluid elastic actuator cannot destabilize the structure at high frequencies.

CHAPTER 7:

Overview and Conclusions

7.1 OVERVIEW

A pressurized elastic vessel undergoes elastic deformations. If the pressure is controlled, the elongation is predictable. This fluid elastic actuation concept was used to develop the P-Strut. Fluid pressure, controlled by a commanded input force, produced axial elongation. The static operation was observed to be linear and precise. Dynamic input force caused a dynamic elongation which was limited in bandwidth due to an orifice through which the viscous fluid flowed.

Models of the static, passive, and active performance were developed from mechanical principles. The models allowed the optimization of the material and geometric properties. In addition, the models can be extended to the design of other similar fluid elastic actuator concepts.

Three P-Struts were manufactured and tested. The experimental results verified the static and active models. In addition, the tailored composite properties of the third P-Strut resulted in dramatically better

141

performance. Other experimental results indicated that the frequency performance of the fluid elastic actuator can be tailored either by the fluid viscosity or more effectively by the diameter of the orifice. The passive performance was masked by other damping effects of uncertain origin. The analytical modeling and experimental results showed that the P-Strut geometry is not optimal for this function. As an actuator, the P-Strut's results are excellent.

7.2   CONCLUSIONS

The P-Strut is a functional fluid elastic actuator with properties comparable to other actuators over a specified bandwidth. In addition, the P-Strut is manufactured from "off-the-shelf" components. The physical principles by which the P-Strut operates has been mathematically modeled. These models allow optimization of P-Strut designs.

The P-Strut can be effectively used in the control of a structure. The bandwidth inhibits actuation above the frequency of the roll-off regardless of the stability of the compensator. The linear nature of the actuator simplifies control and allows the damping of low frequency modes. The P-Strut can also be used to command and hold static displacements.

7.3   FUTURE WORK

A final demonstration of the usefulnes3 of the current P-Strut for active control is in progress at SERC at MIT. A P-Strut will be inserted into the optical interferometry testbed [5,36], and used to damp low frequency disturbances. The P-Strut concept is also being considered for use in the Stellar Interferometry Testbed Experiment (SITE) at SERC. For this application, the design will be modified to optimize both the passive and active performances. In addition, industry has demonstrated interest in the fluid elastic actuation concept.

The contribution of this work to future fluid elastic actuator is mostly in the modeling of Chapter 3 and the verification of the models by the results of Chapter 6. The demonstration that the performance of the actuator can be tailored by properly selecting its components' material and geometric properties is relevant to any fluid elastic actuator design.

References

1. Aldrich, J.L., "Design of Passive Piezoelectric Damping for Space Structures." First Annual North American Conference on Smart Structures. Paper in Print. Alberque, N.M. February 1-4 1993.

2. Anderson, E.H., Trubert M., Fanson, J.L., and Davis, P., "Testing And Application of a Viscous Passive Damper for Use in Precision Truss Structures." *Proceedings of the 33rd Structures, Structural Dynamics, and Materials Conference.* AIAA Paper No. 91-0996, Baltimore Maryland, MD. April 8-10, 1991. pp 2796-2808.

3. Anderson, E.H., Blackwood, G.H., and How, J.P., "The Role of Passive Damping in the MIT SERC Controlled Structures Testbed," International Symposium on Active Materials and Adaptive Structures, Alexandria, VA. November 1991.

4. Anderson, E.H., Moore, D.M., and Fanson, J.L., "Development of An Active Truss Element for Control of Precision Structures." *Optical Engineering.* Vol 29 (11). November 1990, pp 1333-1341.

5. Blackwood, G. H., Jacques, R.N., and Miller, D., "The MIT Multipoint Alignment Testbed: Technology Development For the Optical Interferometry." SPIE Conference on Active and Adaptive Optical Systems. Paper No. 1542-34. July 1991.

6. Bolz, R.E. and Tuve, G.L., *CRC Handbook of Tables for Applied Engineering Science.* 2nd Ed. Cleavland, Ohio: CRC Press.

7. Butsuen, Tetsuro. *The Design of Semi-Active Suspensions for Automotive Vehicles.* S.M. Thesis in Department of Mechanical Engineering at the Massachusetts Institute of Technology. June 1989.

8. Cotton, William L., "Acid and Alkaline Chemical Milling Processes for Aluminum Alloys." *The Finishing of Aluminum.* Chap 3. G.H. Kissin, ed. New York: New York. Reinhold Publishing Corp., 1963.

9. Cunningham, D.C., "Development of the PACOSS D-Strut." Proceedings of Damping 1991, San Diego, California, February 1991. *Proceedings of Damping '91.* Vol. III. Paper No. IAA. Wright Laboratory, Wright-Patterson AFB, Ohio.

10. Craig, R.R., Jr., "Recent Literature on Structural Modeling, Identification, and Analysis." Chapter 1. *Structural Modeling, Identification, and Analysis*. AIAA 1990.

11. Crawley, E. F., Sarver, G.L., and Mohr, D.G. "Experimental Measurements of Passive Material and Structural Damping for Flexible Space Structures." *Acta Astronautica*. Vol 10. May-June 1983. pp 381-393.

12. Crawley, E. F. and Hall S.R., *The Dynamics of Controlled Structures: Course 16.093 Notes 1991*. SERC Report #10-91-I. Massachusetts Institute of Technology, Cambridge, MA.

13. DamJanovic, D. and Newnham, R.E., "Electrostrictive and Piezoelectric Materials for Actuator Applications." *Journal of Intelligent Materials, Systems and Structures*. Vol. 3. April 1992.

14. Davis, L.P. and Ginter, S.D. "An Advanced D-Strut." Proceedings of Damping 1991, San Diego, California, February 1991. *Proceedings of Damping '91*, Vol. III. Paper No. IAC. Wright Laboratory, Wright-Patterson AFB, Ohio.

15. Dow Corning Silicone Fluids 200 Fluid Series. Product Information. Dow Corning Corp. Midland, Michigan. January, 1970.

16.. Gibson, J. E. *Thin Shells: Computing and Theory*. New York: New York. Pergamon Press, 1980.

17. Graves, M.J. *16.292 Advanced Laminar Composites: Course Notes*. Massachusetts Institute Technology, Cambridge, Massachusetts, Spring 1992.

18. Graves, M.J. *The Catastrophic Failure of Pressurized Graphite/Epoxy Cylinders*. PhD Thesis in Department of Aeronautics and Astronautics, MIT, September 1982.

19. G. W. Lisk Company, Inc. Standard High Performance Solenoids, Catalog 9A Tubular Solenoids. Product Information. Clifton Springs, New York. 1992.

20. Hagood, N.W. and von Flotow, A.H., "Damping of Structural Vibrations with Piezoelectric Materials and Passive Electrical Networks." *Journal of Sound and Vibration* 1991. pp. 243-268.

21. Hagood, N.W. and Crawley, E.F. "Experimental Investigation into Passive Damping Enhancement for Space Structures." AIAA Paper No. 89-3436. *AIAA Journal of Guidance, Control, and Dynamics*. Vol. 14. No. 6, pp 1100-1109, Nov.-Dec. 1991.

22. Hallauer, W. L. and J. C. Smith. "Air Jet Thrusters for Active Vibration Control: Design and Calibration." Work Conducted at the United States Air Force Academy, Colorado Springs, Co. 1991- 1992. Published in *Experimental Techniques*. Date unknown.

23. Hallauer, W. L. and S. Lamberson. "Experimental Active Vibration Damping of a Plane Truss Using Hybrid Actuation." 30th AIAA/ ASME/ASCE/AHS/ASC Structures, Structural Dynamics, and Materials Conference. Mobile, Alabama. April 3-5, 1989.

24. Harvey, John F. *Theory and Design of Pressure Vessels*. New York, New York: Van Nostrand Reinold Company, 1985.

25. Jones, Robert M. *Mechanics of Composite Materials*. New York, New York: Hemisphere Publishing Corporation, 1975.

26. Karnopp, D. C. "Active and Passive Isolation of Random Vibration." *Isolation of Mechanical Vibration, Impact, and Noise*. ASME Design Engineering Technical Conference, Cincinnati Ohio September 1973.

27. Kelkar, Vasant S. and Robert T. Sewell. *Fundamentals of the Analysis and Design of Shell Structures*. Englewood Cliffs, New Jersey: Prentice-Hall, Inc., 1987.

28. Laglace, P.A., Beaumont, M., Brewer, J.C., and Vernerin, C.F. *TELAC Manufacturing Course 16.291 Class Notes*. Technology Laboratory for Advanced Composites at Massachusetts Institute of Technology, Cambridge, MA. September 1991.

29. Lee, David R. and Steven G. Webb. "Passive Control of a Flexible Planar Truss Using a Reaction Mass Actuator." Work Conducted at the United States Air Force Academy, Colorado Springs, Co. 1990- 1991. Unknown Publication Source.

30. Lim, K. B., Maghamni, P.G., and Joshi, S.M., "A Comparison of Controller Designs for an Experimental Flexible Structure." 1991 American Control Conference. Boston, MA. June 1991.

31. Malinckrodt Material Safety Data. Product Information. Paris, Kentucky. March, 1990.

32. Mattiat, O. E. *Ultrasonic Transducer Materials*. New York, New York: Plenum Press, 1971. Chapter 2.

33. McDonald, Alan T. and Robert W. Fox. *Introduction to Fluid Mechanics*. New York, New York: John Wiley and Sons, 1985.

34. Mikulas, M. M. Jr, *SDM Lecture: Space Structures Technology*. 33rd Structures, Dynamics, and Materials Conference. LaHolla, CA. April 21, 1993.

35. Morgenthaler, D.R. "Design, Analysis, and Testing of the PACOSS D-Strut." Proceedings of Damping 1991, San Diego, California, February 1991. *Proceedings of Damping '91*, Vol III. Paper No. IAB. Wright Laboratory, Wright-Patterson AFB, OH.

36. Nisbet, A.M. *Design of an Optical Interferometer Spacecraft*. S.M. Thesis in Department of Aeronautics and Astronautics. May 1992. SERC #10-92.

37. Ogata, Katsuhiko. *Modern Control Engineering*. Englewood Cliffs, New Jersey: Prentice-Hall, Inc., 1970.

38. Parker Metal Bellows. Product Information. Parker Metal Bellows Sharon Division, Sharon, Massachusetts. 1992.

39. Plunkett, R. and C. T. Lee. "Length Optimization for Constrained Viscoelastic Layer Damping." *Journal of the Acousitcal Society of America*. Vol. 48. No. 1 (2). July 1970, pp. 150-161.

40. Rafati, Hamid. *Experimental Evaluation of a Non-Linear Controller for a Pneumatic Active Suspension*. S.M. Thesis in Department of Mechanical Engineering, February 1985.

41. R.G. Ni and Adams,R.D., "The Damping and Dynamic Modulii or Symmetric Laminated Composite Beams—Theoretical and Experimental Results." *Journal of Composite Materials*, Vol. 18, March 1984. pp. 104-121.

42. Royers, Herbert C. *Electromagnetic Devices*. New York, New York: John Wiley & Sons, Inc. 1941.

43. Scotch-Weld Technical Data Sheet: 2216 B/A Gray or Translucent Epoxy Adhesives. 3M Industrial Specialties Division, St. Paul, MN. July 1991.

44. Scribner, K.B., Sievers, L.A., and von Flotow, A.H., "Active Narrow Band Vibration Isolation of Machinery from Resonant Substructures." *Active Noise and Vibration Control 1990*. ASME Winter Annual Meeting of the American Society of Mechanical Engineers. Nov. 25-30 1990.

45. Singer, N.C. and Seering, W.P., "Preshaping Commands Inputs to Reduce System Vibration." ASME Vol. 112. March 1990.

46. Sivers, L.A., and von Flotow, A.H., "Linear Control Design for Design for Active Vibration Isolation of Narrow Band Disturbances." Proceeding as of the 27th Conference of Decision and Control. Austin, TX. IEEE 1988. pp 1032-1036.

47. Stevens, K.K., *Statics and Strengths of Materials*. 2nd Ed. Englewood Cliffs, New Jersey: Prentice-Hall, Inc., 1987.

48. Ting, J. and Crawley, E.F., "Characterization of Damping of Materials and Structures from Nanostrain Levels to One Thousand Microstrain." AIAA Paper No. 91-1125, AIAA Journal, Vol. 30. No. 7, pp 1856-1863.

49. Torvik, P. J. "The Analysis and Design of Constrained Layer Damping Treatments." *Damping Applications for Vibrational Control*, AMD-Vol. 38 ASME, 1980.

50. Unchino, Kenji. "Electrostrictive Actuators: Materials and Applications." *Ceramic Bulletin*. Vol. 65 No. 4 1986.

51. Van de Vegte, John. *Feedback Control Systems*. 2nd Ed. Englewood Cliffs, New Jersey: Prentice-Hall, Inc., 1990.

52. Wada, B. K., Fanson J.L., and Crawley, E.F. "Adaptive Structures." *Journal of Intelligent Material Systems and Structures*, Vol. 1. No. 2. April 1990, pp 157-174.

53. White, Frank M. *Viscous Fluid Flow*. New York, New York: McGraw-Hill Publishing Company, 1974.

APPENDIX A: END EFFECTS AND SHELL BENDING THEORY

The well-known longitudinal and hoop stress equations 3.23 and 3.24 reported in Section 3.3.2 for a pressurized circular cylinder assume a plane-stress state. This assumption is incompatible with the boundary conditions. For the P-Strut, the end conditions are clamped-clamped.

Bending theory is capable of determining the end effects and incorporates the elementary stress equations. However, the Bending Theory solution requires several additional relationships including the displacements, strains, and forces in order to acquire enough equations to solve for the strains at the boundaries.

A.1 The Boundary Effects For Isotropic Circular Cylinders

A pressurized, isotropic, thin, closed, circular cylinder with rigid endcaps is depicted in Figure A.1. The end conditions are assumed to be clamped-clamped. Symmetry and isotropy reduce the number of unknown stress-resultants [16]. After some manipulation [16], the key equilibrium condition is given by:

$$\frac{d^2 M_{11}}{dx^2} + \frac{t\,\sigma_{22}}{R_c} - P = 0 \qquad (A.1)$$

The constitutive laws are::

$$\sigma_{11} = \frac{PR_c}{2t} = \frac{E}{(1-v^2)}[\varepsilon_{11} + v\,\varepsilon_{22}] \qquad (A.2)$$

$$\sigma_{22} = \frac{E}{(1-v^2)}[\varepsilon_{22} + v\,\varepsilon_{11}] \qquad (A.3)$$

Substituting A.2 into A.3 yields:

$$\sigma_{22} = E\,\varepsilon_{22} + v\frac{PR_c}{2t} \qquad (A.4)$$

The bending moment stress resultant, M_{11}, is defined as a constant multiplied by the curvature of the deformed shell [16]. The curvature of

interest [16] is defined as the second derivative of the radial displacement, w, which is equal to negative the radial dilation, $(w=-\delta_R)$. Therefore,

$$M_{11} = -\frac{Et^3}{12(1-v^2)}\frac{d^2w}{dx^2} = -\Omega\frac{d^2(-\varepsilon_{22}R_c)}{dx^2} \qquad (A.5)$$

where $\Omega = \dfrac{Et^3}{12(1-v^2)}$ and by geometry $\varepsilon_{22} = -\dfrac{w}{R_c}$

Substituting A.4 and A.5 into A.1, the fourth order differential equation in w is:

$$-\Omega\frac{d^4w}{dx^4} - \frac{Et}{R_c^2}w + (\frac{v}{2}-1)P = 0 \qquad (A.6)$$

The particular solution is:

$$w = -\frac{PR_c^2(1-\frac{v}{2})}{Et} \quad \text{or} \quad \varepsilon_{22} = \frac{PR_c(1-\frac{v}{2})}{Et} \qquad (A.7)$$

This particular solution matches (as expected) the hoop strain (equation 3.26) determined from the elementary stress equations. In general, the homogenous solution to a fourth differential equation is a series of sines and hyperbolic sines which could also be represented by a complex exponential. The homogenous solution, by definition, decays to zero. Adding the particular and homogenous solutions together yields,

$$w = A_1 \sin \lambda x \sinh \lambda x + A_2 \cos \lambda x \cosh \lambda x - \frac{PR_c^2(1-\frac{v}{2})}{Et} \qquad (A.8)$$

where

$$A_1 = \frac{2PR_c^2(1-\frac{v}{2})}{Et}\left[\frac{\sin\chi\cosh\chi - \cos\chi\sinh\alpha}{\sin 2\chi + \sinh 2\chi}\right] \qquad (A.9)$$

$$A_2 = \frac{2PR_c^2(1-\frac{v}{2})}{Et}\left[\frac{\cos\chi\sinh\chi + \sin\chi\cosh\chi}{\sin 2\chi + \sinh 2\chi}\right] \qquad (A.10)$$

and

$$\chi = \frac{\lambda L}{2} \text{ and } \lambda^4 = \frac{3(1-v^2)}{R_c^2 t^2} \tag{A.11}$$

From solving A.2 for the longitudinal strain,

$$\varepsilon_{11} = \frac{PR(1-v^2)}{2Et} - v\,\varepsilon_{22} \tag{A.12}$$

Figure A.2 plots these equations for a cylinder with E = 9 Msi (62 GPa), t = 10 mils (0.25 mm), v = 0.3, R_c = 0.605 in (15.4 mm), and L = 6 in (15.2 cm). The dramatic increase in the longitudinal strain is due to the exponential terms or the homogenous part of A.7. At the ends, the hoop strain drops to zero as the rigid endcaps restrain the cylinder from swelling. As ε_{22} decreases, the Poisson's effect on the longitudinal strain (equation A.12) decreases and therefore, ε_{11} increases.

The total area under the curve is the actuation elongation, δ_L, which was defined in equation 3.31 as the effective length multiplied by the longitudinal strain. To account for the peak in ε_{11} near the boundaries, the length, L, is increased by an amount ϖ where ϖ is a percentage of L. The resulting effective length, L_{eff}, was defined in equation in 3.32 and used in the analysis of Chapter 3.
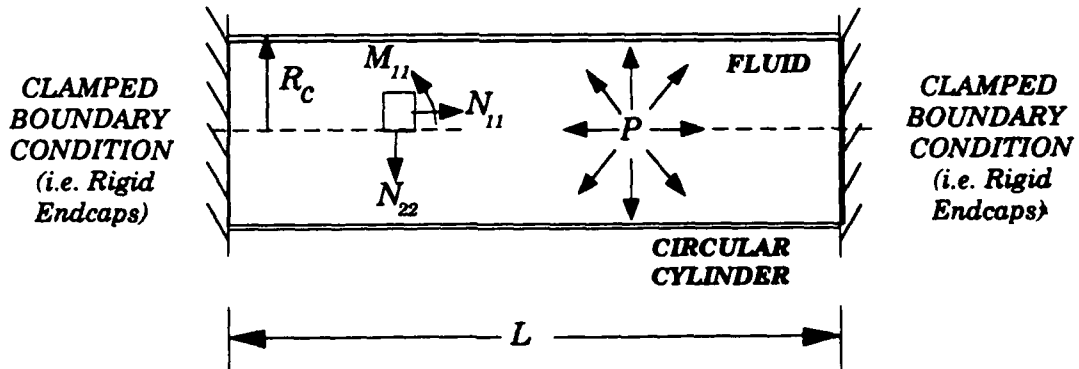

FIGURE A.1: Pressurized Isotropic Circular Cylinder

A.2 The Boundary Effects For Composite Circular Cylinders

If the cylinder is anisotropic the displacements, the strains, and the stress-resultants are coupled. Graves solved the Bending Theory problem for a pressurized, thin, clamped-clamped ended, balanced-symmetric-composite, circular cylinder [7*3]. His analysis is based on an eighth order potential function which efficiently incorporates the displacements, strains, and stress-resultants. His work included a FORTRAN computer program which was reformatted by the author of this thesis into MATLAB and verified against the isotropic analysis of Section A.1.

The "optimal" hybrid, Graphite/Epoxy-Aluminum, P-Strut and the "optimal" composite—see Chapters 4 and 5—are balanced circular cylinders but not symmetric. Nevertheless, if the composite **B** matrix—which couples bending and stretching in the material and is zero for a symmetric laminate—is negligible, Graves analysis and the program remain accurate and consistent with the physics. The entries in the **B** matrices for the hybrid and composite P-Struts are in fact relatively small.

For the [90/∓60/90] composite cylinder proposed in Section 4.3, Figure A.3 depicts the end effects. ϖ for the composite is less than the isotropic cylinder. Since the hoop stiffness is increased over the isotropic P-Strut, ε_{22} is reduced. Therefore, the peaks in ε_{11}, which result from the drop in ε_{22} through the Poisson's effect, are smaller in comparison to the isotropic cylinder. Table 6.2 lists the ratio of effective length to the physical length (L_{eff}/L) for the three P-Struts.
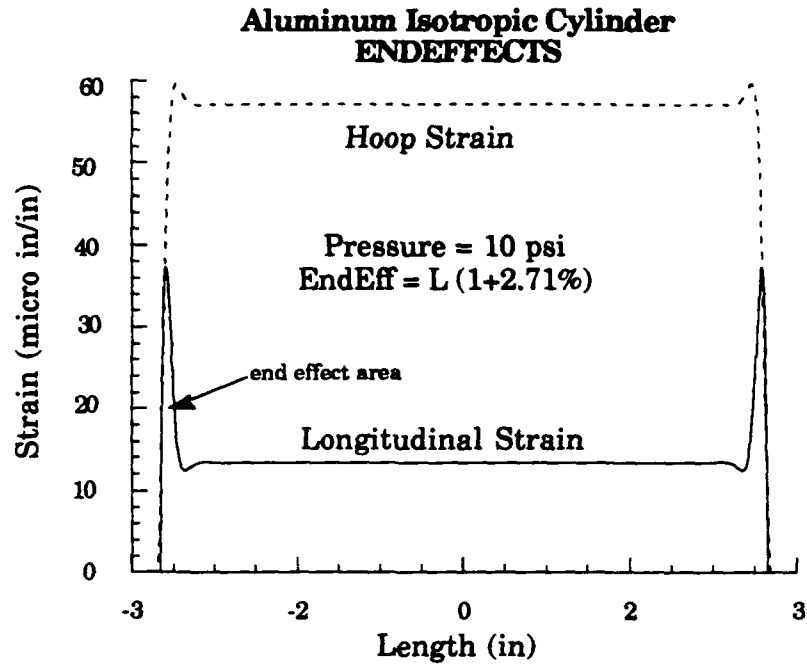
Aluminum Isotropic Cylinder
ENDEFFECTS

Hoop Strain

Pressure = 10 psi
EndEff = L (1+2.71%)

end effect area

Longitudinal Strain

FIGURE A.2: Hoop and Longitudinal Strain in an Isotropic Cylinder

Gr/Ep Composite [90+60/-60/90] Cylinder
ENDEFFECTS

Longitudinal Strain

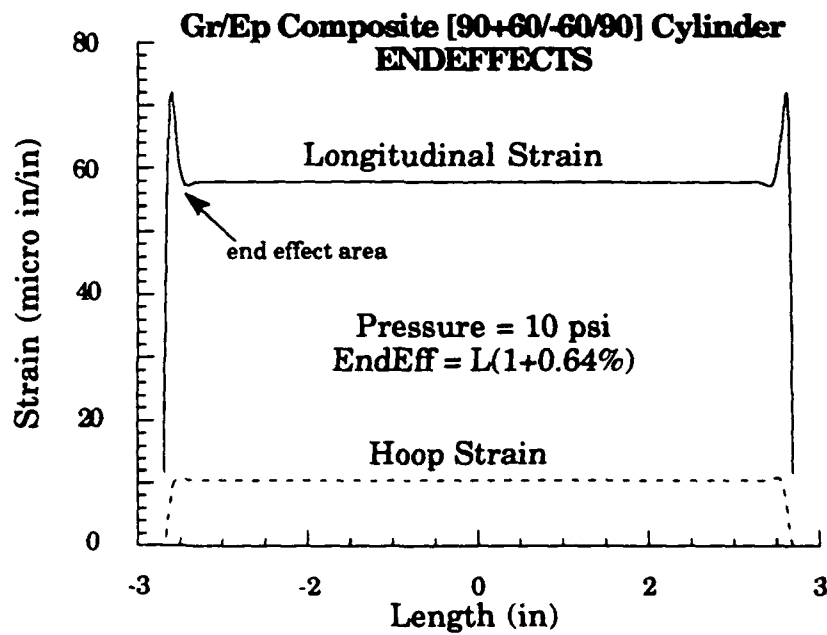end effect area

Pressure = 10 psi
EndEff = L(1+0.64%)

Hoop Strain

FIGURE A.3: Hoop and Longitudinal Strain in a Composite Cylinder